UNIVERSITY OF
BIRMINGHAM

A Methodology Towards the Design and Control of a Microfluidic Device for Single Sperm Capture and Isolation

By

ARRAN J. R. HUGHES

A thesis submitted to the University of Birmingham for the degree of
DOCTOR OF PHILOSOPHY

Department of Mechanical Engineering
School of Engineering
College of Engineering and Physical Sciences
University of Birmingham

April 2023

Abstract

Intracytoplasmic Sperm Injection (ICSI) is an Assisted Reproductive Technology (ART) where a singular sperm is injected directly into an egg for fertilisation to assist couples experience trouble conceiving. Sperm selection is a necessary procedure prior to ICSI for the choosing of the cell to be injected into the egg. In this technique, an embryologist manually selects a sperm based on observation, leading to inconsistencies in the operation between clinicians due to varying experience levels. Therefore, there is a need to assist and automate this procedure to deliver consistent sperm selection prior to injection for more consistent success rates. Microfluidics is a promising technique for the manipulation of cells and other objects of sizes ranging between one to several hundreds of micrometers. This thesis focuses on the develop of a novel microfluidic technique for automated capture, isolation and retrieval of single objects/cells from a larger population with application to ICSI. Initially, a novel manufacturing technique was developed utilising an ablation method with a red femtosecond laser to develop rapid prototypes for the device structure which had replication of 300 µm channels and 200 µm gates gate sizes were 40 µm smaller compared to the original design. Next, a simulation model with particle tracing was developed to determine the key requirements of a countercurrent design in order to facilitate successful capture and release of objects. From this, fundamental pressure requirements were determined to achieve the device function where the pressure difference across the gate dictates flow direction. Geometric restrictions were also determined based on proximity to inlets and outlets where 300 µm from the fluid inlets is required for successful object capture/release. Finally, a theoretical model was developed utilising electrical circuit analogies for fluids to give an analytical solution to the fluid flow in the device as well as to determine controller pressure requirements and the errors determined based on experimental validation. The proposed technique offers a novel method for isolation of objects/cells from a larger population, with the key function of being able to deliver any captured objects/cells individually.

Table of Contents

List of Tables

List of Figures

Acknowledgement

I would like to express my thanks to my supervisor, Dr. Mozafar Saadat, for his continued support throughout the entirety of my Ph.D study. His advice and recommendations have been invaluable in completion of this research.

I would like to thank my family for their unrelenting love and support throughout this long journey, without them I may have given up long ago.

List of Abbreviations

ICSI – Intracytoplasmic Sperm injection

IVF – In Vitro Fertilisation

PDMS – Polydimethylsiloxane

PMMA - Polymethyl Methacrylate

ART – Assisted Reproductive Technology

DNA - Deoxyribonucleic Acid

CASA – Computer Aided Sperm Analysis

DFI – DNA Fragmentation Index

HDS – High DNA Stainability

VAP – Average Path Velocity

VSL – Straight Line Velocity

VCL – Curvilinear Velocity

LIN – Linearity

ALH – Amplitude of Lateral Head Displacement

WOB – Wobble

LED – Light-Emitting Diode

CMOS – Complementary Metal-Oxide-Semiconductor

SLC – Single-Layer Colloidal Centrifugation

SU – Swim-Up Method

SLA – Low Force Stereolithography

UV – Ultra-Violet

RMS – Root Mean Square

WHO – World Health Organisation

List of Symbols

Re – Reynold's Number

ρ - Fluid Density

u – Average Fluid Velocity

d – Characteristic Diameter

μ - Dynamic Viscosity

p – Pressure

$\vec{\boldsymbol{u}}$ – Velocity Vector

$\hat{\boldsymbol{n}}$ – Unit Normal Vector

u_n – Normal Velocity

$\vec{\boldsymbol{u}}_t$ – Tangential Velocity Vector

$\vec{\boldsymbol{F}}$ – Fluid Drag Force

a - Sphere Radius

P_B – Bulk Pressure

P_c – Controller Pressure

Q – Flow Rate

R_H - Hydraulic Resistance

L – Channel Length

R – Channel Radius

w – Channel Width

h – Channel Height

Q_b – Inlet Bulk Flow Rate

Q_c – Inlet Control Flow Rate

Q_n – Flow Rate at Junction n

R_n – Channel Resistance in Channel n

P_n – Pressure Difference at Each Node

$P_{b,cont}$ – Bulk Flow Controller Pressure

$P_{c,cont}$ – Control Flow Controller Pressure

$Q_{n,crit}$ – Critical Gate Flow Rate

1. Introduction

1.1 Background

Infertility is defined as the inability of a couple to conceive after one year of regular unprotected intercourse [1]. Male infertility is the sole contributor to infertility issues for about 20% of cases and is a contributing factor for 30-50% of other infertility cases [2]. Globally, this means that around 24 million men have some level of male infertility [3], or approximately 7.5% of couples worldwide struggling to conceive is due to male infertility issues. From these men, 70% exhibit untreatable infertility conditions: oligozoospermia, defined as having fewer than 15 million sperm per millilitre of semen (low sperm count); asthenozoospermia, defined as sperm having less than 40% motility or less than 32% progressive motility (low motile sperm); teratozoospermia, defined as having sperm with less than 15% normal morphology (poor morphology sperm); or normospermia with functional defects, defined as normally analysed sperm with underlying issues (such as zona pellucida binding defects or high levels of reactive oxygen species) [4, 5].

ICSI (Intracytoplasmic Sperm Injection) was first introduced in 1992 as an Assisted Reproductive Technology (ART) to help alleviate the impacts of male infertility [6]. The process involves manually selecting a sperm by an embryologist, immobilising it and then injecting it directly into an oocyte using an injection micropipette. An image of sperm aspiration into the micropipette [7] is shown in Figure 1.1 below.

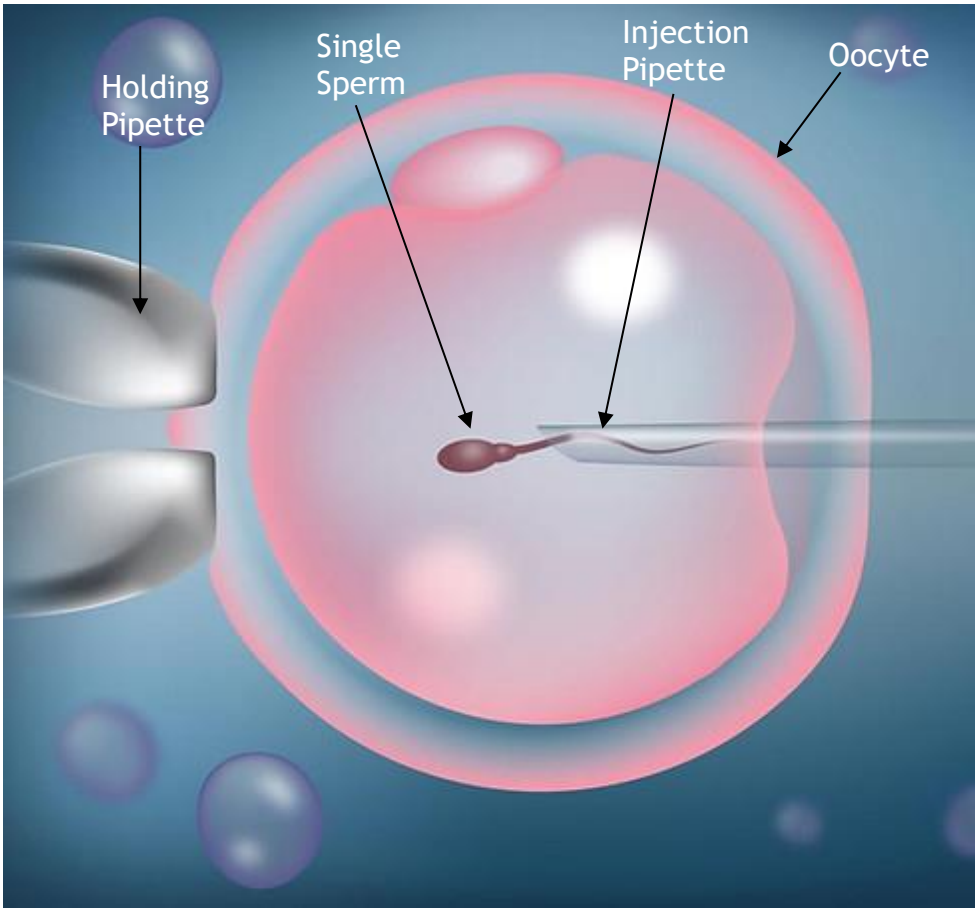

Figure 1.1: A diagrammatic representation of a spermatozoon being injected into an oocyte during a typical ICSI procedure [7].

Sperm selection is a key process prior to ICSI where an embryologist identifies a suitable sperm to be used and manually aspirates it into a micropipette. The selection procedure is based on the parameters laid out by the World Health Organistion (WHO), according to which the sperm should have category 'A' progressive motility (fast progressively motile, with forward velocity over 25 µm/s) and normal velocity [8–10]. If category 'A' sperm are not available, the embryologist will move down the categories for sperm selection from slow progressively motile with forward velocity under 25 µm/s, non-progressively motile and finally immotile, corresponding respectively grades 'B', 'C' and 'D'. Morphology is examined for specific abnormalities in the head, tail and neckpiece such as irregular shapes, asymmetry, multiple heads/tails or any combinations of these defects.

This means that during the current manual selection procedure, the selection of the appropriate sperm is left to the subjective view of the embryologst. This leads to lower chances of a successful ICSI procedure with 1,600 couples having 1 or more ICSI cycles without any success in the years 2017-18 [11]. Further reflecting these inconsistencies,

there are also widely reported different success rates for an already relatively low chance of successful pregnancy of around 40% [12–16].

There are other clinical factors that impact the fertilisation rate of OCSI, such as both patients' age, testicular histology, embryo quality and number of embryos all can affect the outcome [17, 18]. Even though these clinical factors have consistent impacts on the success rates, the main reason for inconsistencies during the ICSI operation remains due to human involvement during the procedure. For this reason, microfluidics has been identified as a potential research breakthrough for the assistance of sperm selection prior to ICSI, particularly due to high DNA damage to cells during the current initial centrifugation step for sperm sorting [19]. Applying microfluidic techniques to ICSI presents a significant engineering challenge, particularly concerning manufacturing devices capable of handling 100s to 1s of microns in dimensions and isolating an individual sperm from a population automatically through fluid control and geometric design. Particularly relevant to the procedure is the retrieval of one single sperm that can be presented for ICSI, which is a technology that has yet to be developed. There is also motivation to develop a fully mechanical system to prevent unknown interactions affecting the sperm prior to injection, as well as utilising an active flow system to assist sperms during ICSI as generally, the sperm sample is weaker than normal sperms. Due to the laminar flow in microfluidic systems, these operations can be performed automatically and consistently since there is very little flow variation between operations as an almost robotic sorting method [20].

The procedure of sorting, isolation and release of individual sperms utilising microfluidics refers to taking a sperm population at the inlet, isolating individual sperms from the population, and releasing them individually to the embryologist, ready for injection. An active microfluidic device can improve selection speed, improve the consistency of the operation performed by the operator, mitigate sperm damage during the procedure, as well as reduce complexity of training required to perform the operation saving costs. These benefits offer significant opportunities for improvements of the present ICSI process to offer better success rates of ART.

Many current microfluidic sorting methods only offer a passive sorting method, where sperms are sorted as a result of their own motility [21, 22]. It is hypothesised that an active flow sorting device is a strong candidate for improving current technologies due to faster

sorting, sorting of the entire sperm sample, and assistance for weaker sperms to overcome present challenges in ICSI.

The main aim of the present research thesis is developing a novel microfluidic technique to be utilised with a fully automated microinjection system, to enhance current drawbacks in manual and microfluidic sperm selection process within ICSI, and ultimately to help embryologists eliminate variability during the sperm selection procedure [23].

1.2 Motivation

The conventional sperm selection method is not efficient since it involves a human operator selecting a sperm based on their own best judgement and using a joystick for motion control, and microscope for monitoring during the procedure. There are several reasons to advance this procedure by automating the selection process, particularly with the use of microfluidics. Firstly, there will be a variation between embryologists based on their experience for sperm selection due to all selection being based on manual observation. The consequence of this is a non-standardised selection procedure which is rather left to best judgement and inevitable human error. This creates situations where a selected sperm chosen may not be the most appropriate for the ICSI procedure from an entire population. As a result, couples may experience a higher failure rate of ARTs leading to increased costs to both the consumers and clinicians for repeated procedures.

Microfluidics is an emerging technology in clinics for sperm selection but has so far been relying on passive sorting techniques. This means that the current technologies can only offer an enhanced motility-based-sorting population of sperm to the embryologist, and the selection and isolation must still be performed manually as an additional procedure. Moreover, the sorting procedure is relatively slow and can only take a smaller segment of the entire sperm sample to be sorted. Therefore, utilising active flow in the microfluidic system provides great advantages by speeding up the process significantly and assisting lower motility sperm populations that may not be viable for these techniques, as reportedly 1 million progressively motile sperm per millilitre are required [24]. The expertise can also be further improved by developing a technology specifically for ICSI which has the ability to isolate and present an individual sperm to the embryologist for the rest of the procedure.

Microfluidics is characterised by micron-sized length scales for channel geometry with fluid reagant flow rates moving in the magnitude of µl/minute. This characteristic means that low reagant volume is required for each procedure, therefore saving costs on consumables. More importantly, this means that a laminar flow condition is maintained throughout the device, which has the property of consistent, and repeatable flow conditions due to there being zero turbulence through the device with proper design and limited inertial fluid effects at lower flow rates. Therefore, microfluidics can offer repeatable fluid control for the manipulation of cells and other micron-sized objects that, when applied to ICSI, can deliver a replicable, reliable, and consistent operation between each procedure.

Clearly then, devices developed for microfluidics provides a useful method of manipulating micron-sized objects. This fact motivates the present study to recognise and evaluate the potential of the application of active-flow microfluidics for automated sperm selection, isolation, and retrieval within ICSI. This thesis further sets out to fulfil the requirement of developing a suitable microfluidic technique for isolation of individual objects from a larger population through active-fluid control.

1.3 Research aim, objectives and methodology

The aim of the present research project is the development of a novel microfluidic automated technique for micro-scale objects/cells to isolate and retrieve individual objects/cells from a larger population, with further application to ICSI.

The objectives of this thesis are as follow:

- To develop microfluidic manufacturing techniques capable of developing 3D channel geometries. The technique should be made for rapid prototyping to allow for consistent design iterations as it is a new technology. The technique is aimed to have a balance of minimum feature size and to enhance manufacturing speed for quick but accurate manufacture of microfluidic devices with small critical gate dimensions.

- To develop simulation analysis of the microfluidic design in order to determine key parameters in the microfluidic device. The simulation should be validated by demonstrating the capture/release mechanism of the new microfluidic technique.

The simulation is expected to be able to be applicable for continuous redesign and development of the device.

- To determine the control mechanism and parameters for fluid control to effectively execute the microfluidic technique. The parameters should be defined based on controllable inputs with a pressure-driven flow. The fluid control should demonstrate control over each individual channel required for object/cell isolation and retrieval.

In this research, a novel microfluidic technique was developed for automation of individual object selection and release, with potential further application to ICSI. To achieve this, manufacturing methods were first explored for rapid prototyping of microfluidic test structures to be utilised for analysing the device operation. An overview of the device design is illustrated in Figure 1.2 below.

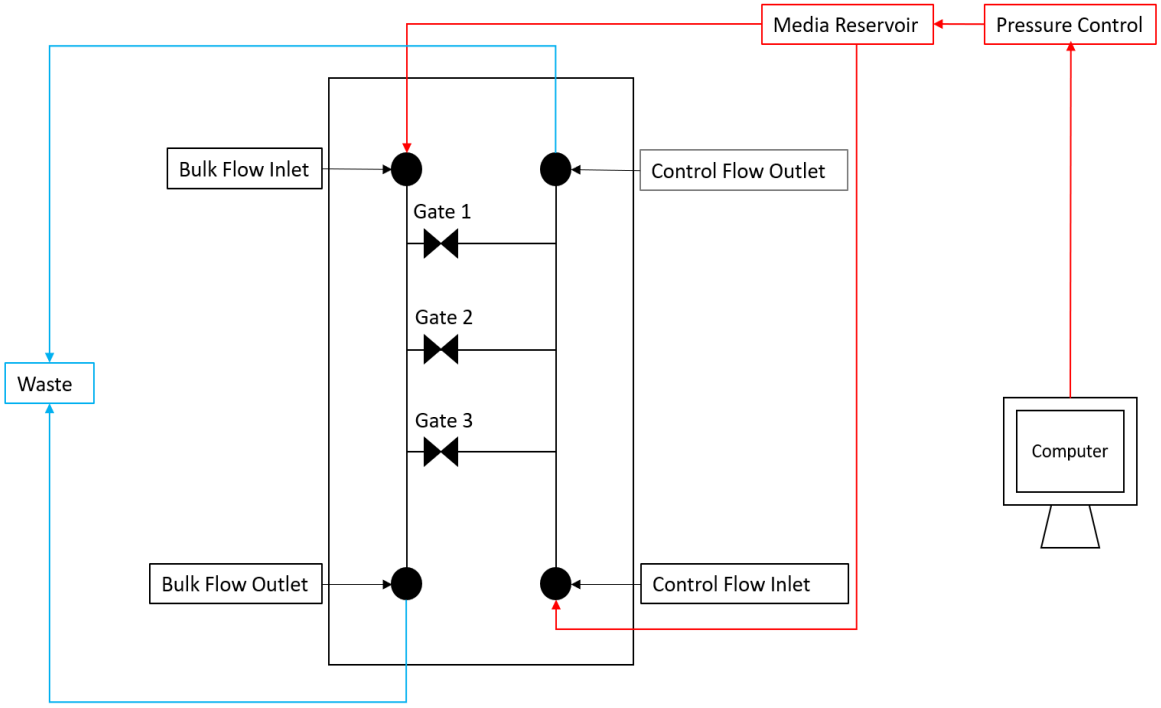

Figure 1.2: Schematic overview of the design for the microfluidic technique.

Figure 1.2 then highlights the general working principles of the microfluidic technique. Two inlets are set up countercurrent to each other, with two other inlets sending any liquid to waste. Gates are placed between each of the channels comprising a geometric restriction to prevent any objects larger than the restriction passing through. The number of gates is

abritrary as long as they can fit between the inlets but 3 is shown for simplicty in the figure. The left channel is denoted as the 'bulk flow channel' which is where any active objects/cells move through and the right channel is referred to as the 'control flow channel' whose only purpose is for fluid control. Pressure driven flow was chosen as this fluid control mechanism because it allows for greater flow stability which is advantageous when considering the precise pressures required due to the sizes of the devices.

1.4 Thesis Structure

This thesis is divided into 6 chapters, and its overall structure is outlined.

Chapter 2 details a literature review of currently published research. This provides a comprehensive background for the research demonstrated in each of the chapters.

Chapter 3 proposes two methods of rapid prototyping for microfluidic devices for proof-of-concept testing. In this study, a novel femtosecond laser technique was developed for the ablation of steel moulds, along with the analysis of the applications of low force stereolithography 3D printing to this specific device design.

Chapter 4 offers a simulation analysis of the microfluidic technique to determine the operating principles to achieve target object capture and isolation. The simulation is first tested with a simple 3-gate design, then updated to determine operating principles and limitations of adding in more gates, as well as the positional requirements to achieve full flow control. The simulation demonstrates further the link between the counter flows, and the effects the magnitude has on the operation of the device to successfully execute the technique and is ultimately validated experimentally. This chapter then demonstrates the main working principles of the device when considering the manipulation of objects.

Chapter 5 establishes the fluid control operational parameters of the microfluidic technique within the device. In this chapter, a theoretical analysis is developed to determine flow rate directions and magnitudes depending on the pressures supplied by the controller. Velocimetric techniques are used to determine parameters relating to the device, and the theoretical description is validated through experimental analysis of fluid flow. Full control over the flow rates within the device is demonstrated and used to validate the effectiveness of the theoretical model.

Finally, Chapter 6 concludes the thesis by providing a detailed account and analysis of Chapters 3, 4 and 5 and correlations between them. This concluding chapter also suggests future research avenues towards the development of microfluidic devices in the field of object/cell sorting and its applications.

2. Literature Review

2.1 Introduction

The current sperm selection process is performed manually by an embryologist with any selection criteria determined by their own subjective experience. This operation is performed utilising a microinjection needle, where a sperm is selected, immobilised and then aspirated into the needle ready for injection. Due to the subjective nature of sperm selection, there are many chances for inconsistencies between clinics, embryologists and even through inevitable human error. As such, there is a need to standardise this procedure and assist the embryologist in developing a consistent sperm selection technique prior to ICSI. The following section is divided into 4 main areas which hold relevance over practical considerations when developing microfluidic devices.

2.2 Microfluidic Device Manufacture

This review of the existing manufacturing literature is largely based on the assessment developed in [25]. Manufacturing of microfluidic devices dates to the invention of photolithography soft lithography techniques in 1998. Photolithography allows for patterning of features with a high resolution (1 μm resolution under standard conditions). However, this technique requires a clean room for mould development, high skilled training, and handling of hazardous substances. Elastomeric stamps or moulds are used within soft lithography for manufacturing of microfluidic features onto a substrate [26]. This method allows for higher resolution feature replication but requires an initial manufacturing step of utilising photolithography or micromachining to make the elastomeric stamps to be used during the manufacturing process. Generally, the elastomeric stamps are made from polydimethylsiloxane (PDMS) or polymethylmethacrylate (PMMA).

PDMS in particular has gained significant interest in the scientific field, not only for exploration of manufacturing methods via soft lithography, but also as the main material to be used in microfluidic devices containing all the channel structures. PDMS has many desirable properties for use in microfluidics such as inertness, biocompatibility (non-toxicity), porous to allow oxygen to diffuse through for live cells, optical transparency (at 230-700 nm), flexibility, and stability at a wide range of temperatures [27–29]. The material

is relatively cheap, and there are several manufacturing methods that can be utilised for rapid prototyping with PDMS as all that is required is a mould where the PDMS is poured, and the structure replicated from the mould. This makes it very suitable for disposable, single-use, low-cost devices to be developed for microfluidic research. There are potential disadvantages, however, particularly for biomedical applications such as liquid evaporation in the channel creating bubble propagation, which can then lead to cell death, or the PDMS could absorb hydrophobic compounds. These problems could nevertheless be mitigated by utilising surface coatings such as parylene for absorption, prevention, or environmental controls [30].

A low cost, easily performed and well-established technique for microfluidic device manufacture is replica moulding, which requires almost no specialist equipment [31–33]. The process involves mixing unpolymerized PDMS and a curing agent, pouring it over a mould and then either thermally curing the mixture in an oven or letting it cure at room temperature over a longer period. The PDMS can then be peeled from the mould after revealing the microfluidic geometry assuming the mould is a positive print of the microfluidic device. Clean room facilities are not required, and the equipment utilised is only a temperature-controlled oven, and potentially a desiccator/vacuum chamber for removal of air bubbles prior to curing. The mould used for microfluidic device fabrication is typically made from Su-8 or PDMS, which is in turn produced using conventional photolithographic techniques.

There has additionally been progress made in recent years in the development of metallic moulds for replica moulding techniques. This is the case not only because of their capacity to withstand high temperatures during curing with low thermal expansion, which in turn is due to their small thermal coefficients of expansion, but also because they can be re-used many times [34]. Peeling of PDMS has also been performed on these devices without the need for surface coatings, which can be a problem with other manufacturing methods [35–37]

Additionally, using lasers as an ablation method of the metallic moulds is a current area of research to develop the positive mould. Laser ablation is a non-contact process and can achieve high resolution geometries, limited by the beam spot diameter of the laser optics system. Presently, three main types of lasers are in use: continuous wave, pulsed

(nanosecond) or ultra-fast pulsed (femtosecond) [38]. Optimisation of laser optical parameters has been widely researched, and has an application to manufacture good quality channels with dimensions close to the intended design [39, 40]. The lower pulse duration of the ultra-fast methods gives the best quality of mould manufacturing where material is removed through the sublimination process instead of melting and vaporisation [41].

A comparison of current microfluidic manufacturing techniques [25, 42–54] is shown in Table 2.1:

Table 2.1: A brief overview of current microfluidic manufacturing techniques [18, 34–46].

Microfabrication Technology	Geometry Choice	Min. Feature Size	Max. Height	Time/Speed	Cost	Commercial Availability
Wet Etch	2D only.	3 µm	500 µm	1-3 µm/min	Expensive due to clean-room facilities	Most common mould manufacturing technique with high throughput.
Dry Etch	All geometry including 3D (some undercutting)	100 nm	10 µm	100 µm/min	More expensive than wet etch due to plasma generation.	Widely used but not as often as wet etching.
Deep Reactive Ion Etching	All geometry including 3D (no under cuts)	40-100 nm	500 µm	3.2 µm/min	Very expensive due to initial capital.	Not often used.
E-beam Lithography	2D only	1-100 nm	5 µm	1-500 nm/min	Most expensive due to capital and operating costs.	Ideal for low volume applications only due to no mask requirement.
Powder Blasting	2D only	<50 µm	>1 mm	1 mm/min	Relatively cheap due to not requiring clean room.	Not widely used due to being a serial process.

Micromachining	All geometry including 3D (no undercuts)	0.1-25 µm	40 µm	6mm/min	Expensive due to control and tooling prices.	Not widely used due to being a serial process and specialist equipment needed.
X-ray Lithography (LIGA)	2D only	0.1-3 µm	0.1-1 mm	0.24 µm/min	Very expensive due to initial capital and operating costs.	Not used often due to specialist equipment/facilities being required.
Wax 3D Printing	All geometry including 3D	75 µm	50 µm	Varies as function of channel size.	Very cheap due to low initial capital and operating costs.	Technology is currently being developed to be used in wider research.
Laser Ablation of Steel Mould	All geometry including 3D (no undercuts)	1 µm	1 mm	1 mm/min	Expensive initial capital costs but cheaper operating costs due to no clean-room facilities required	Suitable for 3D prototyping but not commercially due to it being a serial process.
Low Force Stereolithography 3D Printing	All geometry including 3D	50 µm	Several millimetres	1-3 cm/hour	Relatively cheap initial capital and operating costs.	Suitable for 3D prototyping, commercial viability requires higher capital investment in number of printers.

In addition to Table 2.1, optimisations of these techniques have been further researched, such as micro milled channels with gas blowing assisted PDMS coating which allows for 3D planar surfaces to be manufactured, and then optimised by coating the surface with PDMS. However, this has only been researched for 100-800 µm feature sizes [55]. Full 3D manufacturing techniques have likewise been explored, such as the development of 3D micromixers or other 3D microstructures by femtosecond laser direct writing which are suspended inside fused glass silica. Nevertheless, this technique does not seem to be very suitable for mould manufacture, but can generate a prototype for long-term usage [56–59]. Laser ablation of moulds has also been previously discussed by Isiksacan et al.; however, manufacturing a 3D planar surface would require several steps as the ablation is a through-cut of sacrificial PDMS and acetate [60].

Table 2.2 below highlights the specific niches that each of the manufacturing methods fulfil:

Table 2.2: A comparative summary of each of the manufacturing methods highlighted in Table 2.1.

Microfabrication Technology	Geometry Choice	Min. Feature Size	Max. Height	Time/ Speed	Capital Costs	Operational Costs	Commercial Availability
Wet Etch	-	-	-	- -	+	-	+ + +
Dry Etch	++	++	- -	-	+	- -	+ +
Deep Reactive Ion Etching	+	++	-	- -	- -	- -	- - -
E-beam Lithography	-	+++	- - -	- - -	- - -	- - -	- - -
Powder Blasting	-	- -	++	++	+ +	+ +	-
Micromachining	+	+/- (Depending on tooling)	- -		-	+ +	- -
X-ray Lithography (LIGA)	-	+	+		- - -	- - -	- -
Wax 3D Printing	++	- -	- -		+ + +	+ + +	-
Laser Ablation of Steel Mould	+	+	++	++	- -	+	- - -
Low Force Stereolithography 3D Printing	++	- -	+++	+	++	+++	+

Table 2.2 highlights that the most ideal rapid prototyping methods should be laser ablation for those researchers with access to laser facilities as an alternative to outsourcing their manufacturing processes; however, this method is not suitable for commercial manufacturing due to the reasons mentioned in Table 2.1. Low force stereolithography 3D printing is a good choice for prototyping moulds at a larger scale due to the relatively high minimum feature size for proof-of-concept testing in research, especially at the design stage due to the fairly quick speed and low capital costs of obtaining the equipment for use. Both techniques are particularly suitable for biomedical applications where the chip is required to be disposed of between each experiment or test. Each method allows for a mould to be formed, so multiple chips can easily be developed by replica moulding with PDMS as prototype testing for developing microfluidic research designs.

Finally, micromachining can be considered as a useful manufacturing technique since it is a method that works well with devices that are required not to be made from PDMS due to the previously highlighted absorption and hydrophobicity issues [60] as this method can be used with other plastics such as PMMA.

2.3 Sperm Sorting/Devices

There have equally been many recent advances in the field of sperm sorting utilising microfluidic devices. One of those first developments is one that utilises parallel laminar flow lines along with a passive pump to sort motile from immotile sperms. Due to the flow lines being laminar, only cells with their own movement can move between the lines and out of the original path to where they can be collected and examined. This has the added benefit of removing any debris or unwanted cells from a sample inserted at the inlet so that the final sample is almost completely pure as shown in figure 2.1.

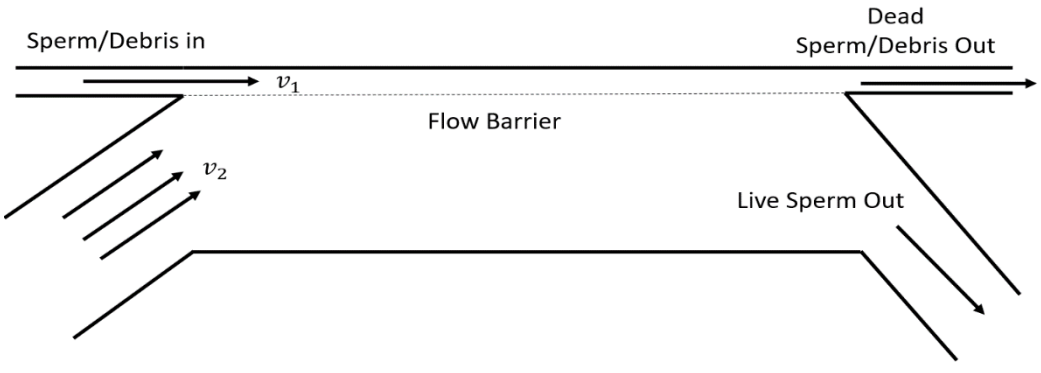

Figure 2.1: Schematic of laminar flow channel design from [61] for motile and nonmotile sperm. Nonmotile sperm and debris stay in the laminar channel and move to the waste outlet and only motile sperm exit out of the collection channel.

Figure 2.1 highlights the differing velocities between the top and bottom inlets, this creates a boundary between each of the flows which only live sperm can pass to move to the oulet. This device was tested twice, initially only using a sample of washed human sperms with 42% motility and 9.5% Kruger strict morphology at inlet. The device was evaluated using sperm tracking by phase contrast microscopy for motility analysis, sperm tracking by fluorescence microscopy to aid with motility analysis and utilising a Makler counting chamber to evaluate sperm concentrations. As a result, the outlet motility was found to be 100% and the Kruger strict morphology was 22.4% [61]. This same device was then evaluated again using germ cells along with human sperm cells within the inlet sample and evaluated in the same way. It was found that motility increased from 69% at inlet to 98% at outlet and the Kruger strict criteria increased from 10% at inlet to 22% at outlet. As a result, it was seen that between both tests the results led to almost 100% motility at the outlet showing that this technique can purify any cells lacking vitality. It also resulted in an increase of around 12% in Kruger strict morphology criteria, which means that there are more normal sperms at the outlet. DNA effects of the device weren't examined; however, only using a microfluidic device implies that it is still better than conventional techniques [62].

Furthermore, it was discovered that a micro diffuser type movement can be used to sort sperm using a gradient flow velocity [63] as shown in figure 2.1.

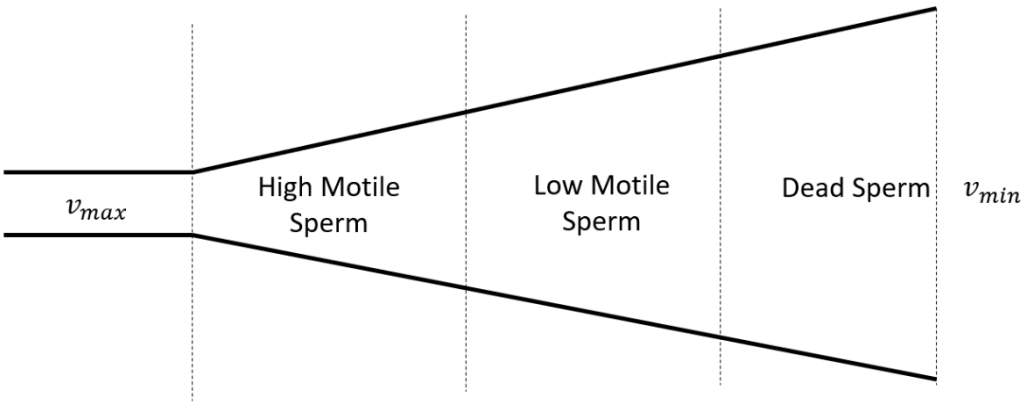

Figure 2.2: Schematic of the diffuser design from [63]. The increasing channel width reduces fluid velocity where at >70 µm/s highly motile sperm turn against the flow due to rheotaxis, with lower motile sperm turning at lower fluid velocities.

This takes advantage of the rheotactic behaviour sperm exhibits when it flows in fluid velocities below 70 µm/s, causing it to turn against the direction of the flow [64]. This idea was deemed inefficient for the chip presented in the present research project, since, although the sperms can be chosen quantitatively depending on their position in the channel, it also makes extracting of them out of the channel more difficult to do automatically. The streamline system almost guarantees motile sperm at the outlet for further sorting/isolation.

Another device that was developed involves using long, radial microchannels which can transport a high volume of sperm through a high viscosity liquid, causing them to separate themselves out [65] as shown in figure 2.3.

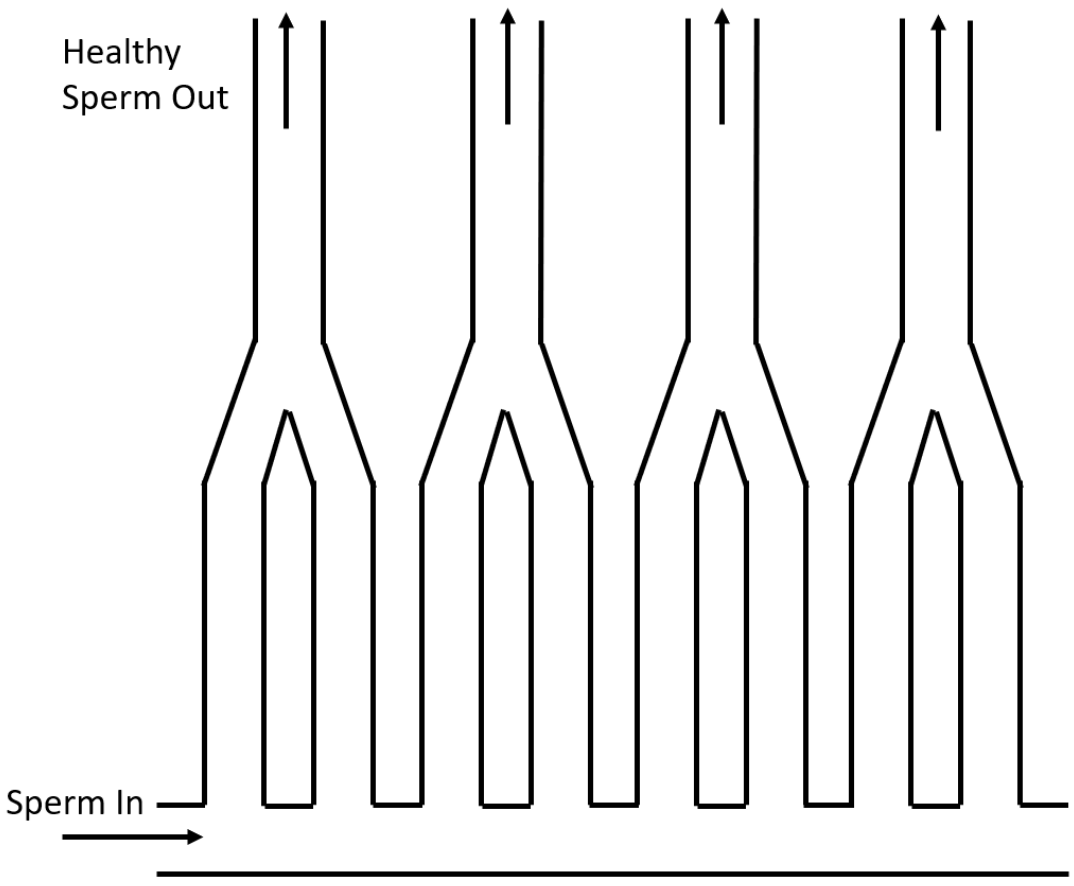

Figure 2.3: Schematic view of the microfluidic device developed in [65]. The channels are repeated radially for 500 parallel channels in total. Viscous fluid allows the sperm to be sorted by progressive motility with high throughput.

Sperms are collected at the end of the channels by taking the lid off the device and extracted using a pipette. Imaging of the sperm was performed using a conventional

Computer Aided Sperm Analysis (CASA) software along with fluorescent staining of the sperms to assist in tracking them. The device was initially tested using bull sperm for different microchannel lengths to assess the sperm concentrations and percentage vitality at the end of the lengths. It was found that there is a link between rapid progressive sperm motility and vitality, and that increasing the distance that sperms travel does not have a negative impact on sperm vitality. The device was tested again using human sperm with the aim to determine the effects the device has on the DNA of the sperms. It was discovered that sperm viability increased by 9% utilising each device, percentage DFI (DNA Fragmentation Index) decreased by approximately 10% and percentage HDS (High DNA Stainability) reduced by approximately 3%, all implying a higher DNA and chromatin integrity when being sorted by the device. The effects that the specific device design had on overall motility or morphology were not examined along with the ability of the device to only provide a 'purer' concentration of a still large batch of sperm.

Valves have been developed by Quake et al. (named Quake valves)[66] where multilayer soft lithography is used in order to create channels that overlap each other, where a pressure applied to a channel causes the elastomer to deform and shut the corresponding channel below it as a valve would.

These Quake valves offer a way to integrate all components onto the chip itself; however, it also requires significantly more complicated manufacturing (multilayer lithography and different channel geometries between layers) as well as design methods (ensuring channel overlap) which could lead to increased costs and more sophisticated control [66]. Other valves used in microfluidics include using a modified solenoid valve where a 10 mm diameter solenoid armature was placed above a channel with a small poly(methyl methacrylate) (PMMA) bead attached to the bottom of it, thus decreasing the contact area of the solenoid such that it only presses against the channel. This causes the channel to deform in a similar fashion to the quake valve by bending the elastomer while being an external component working from applied voltages [67].

2.4 Imaging Techniques

2.4.1 Diagnostic Imaging of Sperm

Imaging is generally performed to either check the morphology of a sperm cell or to determine the motility of the cell using various factors that give information about the health of the sperm. VAP (Average Path Velocity), VSL (Straight Line Velocity) and VCL (Curvilinear Velocity) indicate the activity of dyneins and axonemes (proteins within the flagellar that slide over each other to facilitate movement). LIN (Linearity) shows the direction of the sperm moving towards the appropriate direction (e.g., towards the egg for fertilisation). ALH (amplitude of lateral head displacement) detects hyperactivity in the cells if it is found to be too high which is also determined by WOB (Wobble = VAP/VCL) [8].

A full investigation has been performed on the current state of CASA, current professional opinion and where it can be used, as well as the future requirements to allow CASA systems to be utilised within a clinical environment for successful sperm assessment [68]. In-depth discussion has been undertaken regarding the advantages of using CASA to determine flagellar tracking and analysis as an advantage over traditional techniques where a combination of flagellar tracking and viscosity analysis can be combined in the future for better clinical and diagnostic techniques. The study highlights the current opinion that CASA systems cannot outperform the assessment of WHO-trained staff for counting, and that improvements are needed for routine clinical use. Moderate voices on the issue suggest that CASA can be used for categorising the kinematic measures of semen quality and new/innovative tests for this should be an aim moving forward. Flagellar analysis is also recommended in this study to push motility analysis forward (although this opinion may be biased). Current imaging technology can observe sperm motility in 3D using a 4200 fps (frames per second) camera, and modern algorithms have been developed rapidly to analyse the data from the cameras. Differential dynamic microscopy has also been developed to allow for analysis of approximately 10^4 cells in a few minutes to offer a rapid screening of samples. 3D analysis of human sperm motility may not be relevant for analysis due to sperms normally only swimming in approximately 80-180 µl of fluid in the cervix, so free swimming-analysis is not particularly useful for clinical analysis. This is also the case because there will be surface effects on sperm within the reproductive tract, so 3D motility

analysis may only be relevant for diagnostic analysis. Viscosity may also be an indicator as important as kinematics as this allows for the penetration of sperms.

2.4.2 Cell Imaging in Microfluidics

Microfluidics is a rapidly expanding field with a wide range of uses especially within the realms of Lab-on-a-Chip. One important field that has seen much exploration is single-cell analysis with many developments such as utilising fluorescence-activated cell-sorting [69], microfluidic technologies like introducing impact forces, for instance [70], and digital microfluidics [71].

However, to successfully implement these techniques, there are several requirements to be met. For instance, sophisticated vision and camera systems are necessary. Moreover, in cases where the cell is isolated for observation, its retrieval from the chip for further use in an operation becomes more difficult [72, 73]. Additionally, many techniques require labelling or highly tuned sensors or setups to detect the cells passing through the microchannels in order to manipulate them, such as using antibody-labelled cells by making them, for instance, fluorescent. Tagged cells can then be isolated into individual groups using optical force-based-manipulation or by utilising acoustic waves [74, 75]. Another method of tagging that can be employed is magnetic activated cell sorting where tagged cells can be controlled using a magnetic field. More typical methods include introducing sheath flow and using the magnet to pull the tagged cells into the target outlet [76–78]. These methods, however, all require labelling of the target cell to allow for manipulation and are typically used for isolating entire cell types from a mixture, rather than isolating an individual cell from a species.

It has been further demonstrated that a fluorescent particle, 6 µm in size, moving past a laser diode can generate a detectable signal and be sorted between two channels [79]. However, this requires that the sperms be tagged in order to be fluorescent under the detector. There have also been developments that have shown the ability to detect the image of a bead at 50 µm in size using a capacitive array which is on-chip but is much larger than a typical sperm, which means that this sensor type is unlikely to have the resolution required [80].

A new development in imaging methods utilises on-chip techniques using various electronics in order to move away from the small field of view that is available with currently used microscopes in practice. One such technique utilises lensless imaging to trace shadows of sperms via a charge-coupled device which has been tested on mouse sperms [81]. This has the added advantage of the capacity to track the motility vectors in both horizontal and vertical axes without combining two microscopes perpendicular to each other which is required traditionally. This technique successfully determined sperm VAP, VSL, VSL/VAP and acceleration. Additionally, it allows for on-board monitoring of sperm cells while they are moving within the chip so that motile ones can be selected at outlet after they have been sorted. Sorting was tested but only along a straight-line channel, so sorting is mostly only the random distribution of the cells. However, when a vertical configuration was used, it was found that there was increased motility, which agrees with current swim-up techniques for sperm sorting.

A sensor array with an LED light source can show images of Caenorhabditis Elegans nematodes giving a resolution limit of 490 nm. However, this required the channel height to be approximately 300 nm to prevent under sampling which would make it difficult for a sperm to fit into the channel [86]. The current and most successful way to count a single cell utilises impedance analysis that postulates that, when a cell (4 μm diameter tested) moves between two electrodes, the impedance changes causing a voltage change, which means that something other than the fluid has passed through the channel [87].

2.4.3 Label-Free Cell Imaging

An important transition to analysing sperms on-chip is through the use of label-free techniques to prevent introduction of foreign material prior to fertilisation. These include methods that do not require tagging or fluorescent labelling but instead utilise different versions of microscopy.

One method that has been used is interferometric phase microscopy technique which determines DNA fragmentation in human sperm [82]. Sperms are placed into a static Makler counting chamber and a picture is taken using an interferometer. This examination is then compared to current acridine orange staining to validate the results of using this technique. Images showed that direct analysis of the WHO parameters was possible

without having to stain the sperms, specifically for DNA fragmentation and acrosome size. Therefore, the technique can be used to monitor these parameters stain-free such that they can be examined during the ICSI operation and eventually utilised for sperm selection without harming the sperms.

Another system allowing for individual selection of sperms within a small flow rate was developed. The device consists of a single junction and an interferometer that monitors an area before it, where if it detects good morphology, a pump is activated to move it to a collection outlet while any that do not pass the scan are left to continue on the same path to the waste outlet [83]. The technique demonstrated sorting for a 2 µl/hour flow rate for human sperms to give approximately 8 sperms per minute from a 3000 sperm batch. The drawback of this device is that once one sperm is selected, an inactive section is used and all other sperms that pass through during that time period are sent to waste, including potentially good and healthy sperms. This device further showed a 90% selectivity with similar selection criteria to that of an embryologist, which means that having a lower throughput allows for the function to be performed successfully. Current WHO (World Health Organisation) parameters were used to identify the correct morphology of sperms which include: an acrosome that composes 40% to 70% of the sperm head area, a typical head shape, no excessively large external cytoplasmic droplets, no more than two small cytoplasmic vacuoles (<20% of head area) and only in the acrosome area along with a straight and smooth midpiece. The technique, although promising, requires an extremely low flow rate to function appropriately, thus sorting could take a long time and currently requires a batch size of sperms several factor times lower than current practice along with a potential to miss healthy sperms that may be better than those chosen by the interferometer.

Quantitative phase microscopy has also been developed using LED microscopes to image human sperms where when placed under the microscope, different phase contrast images are recorded because of the varied height and refractive index of the sperms to the rest of the medium. This technique was used to find sperm trajectories and observe their kinematics assuming that the detected cell was motile if it had specific kinematic properties (e.g., VAP > 25 µm/s or VSL > 11 µm/s) and would then be tracked by the system. The results of the technique were compared to a current CASA system, and it was found that there was only a <5% difference between the two systems [84].

Lens-free 3D tracking of human sperms has been developed using two partially coherent light sources (red and blue) which are shone onto a microchip [85]. A CMOS sensor chip records the dual view holograms that encode the position information of each sperm, then the 3D location can be determined by the centroids of its head images reconstructed in the vertical and oblique channels. High accuracy of the sperms cannot be found with current technology in 3D due to the lack of a high enough temporal resolution as the sperm has a helix radius of 0.5-3 μm and rotation speeds that reach around 15-20 rotations/s. Using this imaging technique, the sperm flagellar trajectory was found to have a helical movement along its path depending on which stage of hyperactivation it was in. If the sperm was normal, then the trajectory would be a normal helix; if it was hyperactivated, then it would move in a more 'wonky' fashion, likely due to the excessive yawing of the cell.

Raman spectroscopy has been of great interest recently as an imaging technique since it allows for direct imaging of sperm DNA fragmentation. Indeed, it has been found that morphological discrepancies may just be an indicator of fragmentation within the cell (but not a perfect one). Raman spectroscopy has therefore been employed to analyse sperms that were able to undergo capacitation by being exposed to heparin for periods of time and to examine the loss of surface proteins coating the cell membrane [88]. This technique has not yet been applied to moving cells due to the longer acquisition time but could be utilised if motile cells were able to be trapped so only the use of optical tweezers has been used so far which may lead to some damage to the cells [89].

Another imaging technique utilises a combination of piezo technology and a segmentation algorithm to track swimming unlabelled cells in three dimensions [90]. To do this, a microscope is attached to a piezoelectric actuator which covers a range of 250 um scanning distance. The actuator moves at 30 Hz and a 2000 fps camera takes a picture at every 8 μm in the z-direction. The system can differentiate between live sperm, dead cells, and any additional debris in the system. Additionally, the tracking of the sperms in 3D is quite good and almost matches the 3D kinematics of the sperm. This matching, however, requires a manual template to be determined first and which can then be matched from the results. The other concern regarding this technique is that the sperms must be in a relatively thin film which is not easy to create for embryologists to select a sperm out of.

An additional system that has been developed for imaging and is now moving to commercialisation is the Bohboh system which has been developed as a new version of CASA and that can track the waveform of the flagellar to determine a new mode of motility. Other methods include utilising strobe pulses (approximately 200 μs) to image the flagellum due to fluorescent light in a microscope with a continuous light source being too weak [91].

2.5 Sperm Microfluidic techniques

Sperms can be manipulated depending on the environment they are placed in. One of the first ways this has been tested was to place the same sample of sperm, diluting it into smaller samples and then inserting it into different channels of different lengths [92]. This was done using mouse sperm where the VSL, VCL and LIN of sperms as well as the percentage of motile sperms were found at the outlet channel. It was discovered that, for passive sorting of sperm cells using only straight-line geometries, 15 mm was the best as this led to the highest values of the results reported and attributed the failure of longer channels to the exhaustion of sperms after around 30 minutes while under incubation.

Another way this was examined was through the use of a filter placed halfway through an upright cylinder so as to emulate the swim-up method [93].

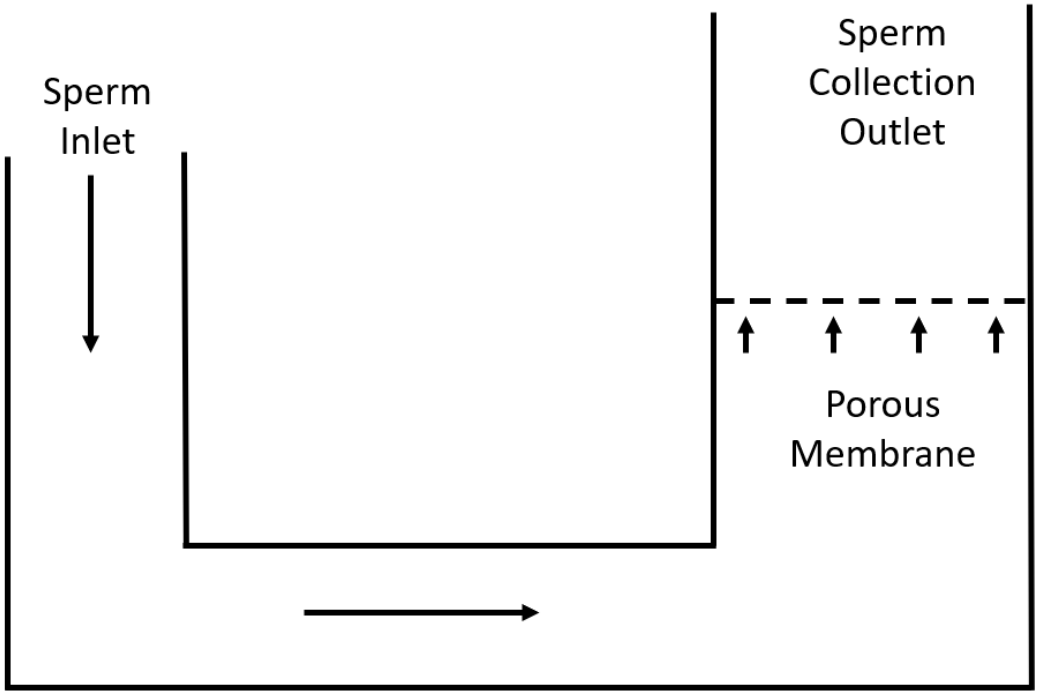

Figure 2.4: Schematic of swim-up design in [93]. Sperm are placed into the inlet and allowed to swim along the channel. At the outlet there is a membrane of various filter sizes to allow only highly motile sperm to pass through.

Human sperm is allowed to swim through a small channel and then upwards in the cylinder with the pore size of the filter changed between 3, 5 and 8 µm. It was determined that the percentage motility increased to near 100% at the outlet (as is expected of the swim-up method). However, the VCL, VSL and VAP were also observed to increase with all the filters, but the effects were best observed with the 5 µm filter which could be due to having the most normal head size. The 8 µm filter increased morphology normality by 14%, leading to a near 30% overall normal morphology. Therefore, perhaps the best filter would sit somewhere between these two sizes to maximise both motility aspects and morphology aspects. It was also highlighted that, whenever microfluidics is used as opposed to the regular centrifuge methods, there is a reduction in reactive oxidative species generated while also giving similar DNA fragmentation results as the standards do.

Attention was also paid to the effects of viscosity on sperm migration by analysing the effects of 50 µm long cells travelling well over 20 cm (especially considering the complex architecture of the reproductive tract) [94]. Thought was given to hyperactivation of sperms where it is suggested that this is due to an out-of-control increase in sperm yaw without enough viscous damping to control the flagellar bending since such studies have only been performed in saline solutions. It was also assessed that current research only focuses on chemotaxis as a sperm guide without considering the viscosity of the mucous layers. This is true as the viscous effects are essential in allowing sperm to enter the cervix during the ovulation phase or in denying entrance through action of the contraceptive pill.

Capture of sperms using gate restrictions has been previously demonstrated [95] utilising photolithography techniques with 1, 1.5 and 2 µm trap height and 2 µm trap width. This system was set up using two parallel channels moving in the same direction, with one driven by positive pressure and the other driven by negative pressure. It was showed that reducing the channel diameter increased the chances of single cells being trapped, but this also led to more cells missing being trapped entirely. It was also determined that, with the peak flow rate of 2.5 µl/min, cell viability after being isolated by the device was not impacted significantly.

Another technique was developed for retrieval of cells that have been captured by restrictions [96]. This technique used capillary burst valves to gradually increment cells through a channel and capture them in a restriction with counter current flow. However,

this system requires precise flow rate values of 110 nl/min and requires precise manufacturing of capillary valves to control the flow against air pressure. The technique did nevertheless demonstrate the potential of counter current flows when used for cell release.

Individual cell-isolation methods have also been developed on microfluidic devices such as using droplet-based microfluidics [97]. This method allows for individual droplets to encompass a single cell but, without further improvements to the method, there is still a high potential of either empty or multiple cells within a single droplet to be present [98, 99]. Other methods include utilising valves within a microfluidic system and the use of hydrodynamic trapping. However, the former method has yet to be demonstrated for individual cell capture [100]. Likewise, even though several trapping mechanisms have been suggested, they all present issues or complications in retrieving single objects once they have been captured [101–103].

A short study has also been performed on the rheological and boundary effects on micro-swimmers utilising a simulation [104]. A new finite element technique was developed to show a force representation of the swimmers with a body-fitted mesh where the effects of shear-thinning were shown as well as swimmers that violate Purcell's Scallop Theorem. The simulation was validated by comparisons of the results with swimmers in microchannels where they scatter over features such as steps and ripples. A different study has also been performed on the effects of human sperm swimming in a high viscosity mucous analogue as a simulation [105]. By testing the effects of changes in rheology, it was found that sperms tend to be pushers at high viscosity but pullers in low viscosity at certain points in the beat cycle. This study further determined that the effectiveness of sperm swimming in high viscosity media is by the loss of cell yawing and provided cell-level information that may ultimately be incorporated into sperm population models.

Further ideas for the simulation of micro-swimmers with a flagellar are similarly shown along with a methodology as an approach. Experimental data is used to generate a waveform for the movement of a singular flagellated microorganism where this information is then used to inform a model of sperm moving in a non-Newtonian flow [106]. Experimental data is inputted to prescribe the waveform and inputted into a finite element code to allow for shear-thinning, Newtonian rheologies and regularised Bingham

fluids to be seen (2D and 3D). Future work mentions analysing human sperm beat patterns and then using the same model to determine fluid flow, swimming velocity and beam stress. From this, internal forces in the flagellum and associated theories of beat control can also be found. Another investigation into simulation of cells is using slender body theory. A study was performed to determine the fastest a cell can swim with subjection to a maximum magnitude of internal actuation rather than using the conventional mean rate of working for inverse efficiency where the equations can then be solved numerically [107]. A bending moment 'fitness' function can be found using equations related to hydrodynamic calculations and estimates for bending and shear stiffness. From the simulation, it was suggested that meandering waves may infer competitive advantages in the movement on sperms.

A simulation has also been created for coarse-graining of the fluid flow around a human sperm. Experimental data was captured and then recreated into MATLAB custom software to determine the angle between the head and flagellum [108]. Principal component analysis was then used to reduce the dimensionality of the data and a flow field was found based on the sperm beat pattern. Quantitative analysis of sperm movement can be found using the model; however, the effects of sperm yawing cannot. A flow field can be summarised and coarse-graining can be used as a way of developing population models while retaining individual cell dynamics.

Cell populations are difficult to simulate due to the large computational time required, especially in 3D. An effort to improve this has been made using meshfree modelling of swimming cells for higher efficiency [109]. A 3D simulation of smaller cells was found to be a difficult challenge due to moving boundaries and complex geometries. In this model, flow fields are determined for multiple uniflagellate sperms swimming between no-slip surfaces to obtain a result. 3480 scalar degrees of freedom were used for a simulation of 5 cells. Velocity and distance results conformed with experimentation (42 μm/s velocity and 0.2 flagellar lengths from the surface) and took 127 s for full calculations to finish. This method allows for the background of a flow (e.g., changing walls/oscillating flow actuation from the wall) to be calculated at the same time as that of the swimmer efficiently and quickly.

Sperm cells have also been examined to determine the accumulation near surfaces through simulation [110]. Slender body representation is used to analyse the sperm movement

along with the fluid-structure interaction. Model validation was found by comparing the results to previous studies using qualitative matching of glancing, reversing, and colliding and their respective angles. The model showed that sperms swim stably within the model, approximately 17 µm from a surface with a 0.4-degree inclination towards it. When cells move towards the surface, if the initial angle is between 0 and 2 degrees, the cell converges to a constant height. For angles of 4 to 6 degrees, the cell rebounds from the surface and escapes. At 8 to 20 degrees, there was no results from the simulation, which implies a direct collision of the sperm head with the wall. This indicates that for a smooth microchannel, degrees should be kept at a maximum of 6 degrees to prevent wall collisions with less than 2 degrees being optimal to allow the sperms to flow along the surface.

Human sperm cells swimming in micro channels have also been tested to explore what happens when inside a microfluidic device [111]. Cross-sections of 100x100 µm microchannels were explored with a 100 µm height. A typical microscope was used, and the sperms were also examined in three different rheologies. All movement is passive of the cell with no influence of a flow field or external environment parameters. It was observed that cells tend to swim along the channel corners and depart from walls on sharp turns forming fans of trajectories such that no cells flow along the inner sides of walls. A running track was made to influence the direction that the cells passively move in within a microchannel. Future work is to observe sperms in micro channels to see if there are additional swimming parameters that can be categorised.

Animal studies have been performed on squid sperm to examine the use of pH-taxis to see how they influence their movement [112]. The pH-taxi was used to make a sperm turn a sharp corner in a low Reynolds number environment. Sperms are placed into a microchannels and having a large proton gradient (>0.025 pH/s) crossing a threshold pH value of around 5.5 causes the sperms to move along the gradient. In the gradient, sperms were observed to move around the edges of it, causing in most cases a turn angle of 120 degrees directing them in a specific direction. This is caused by a specific change in the flagellar beat pattern and head movement when they are affected by the gradient.

Stallion sperm has also been analysed to determine the effects of microfluidics on fertilisation all the way to blastocyte formation [113]. Sperm samples were analysed using: a control group, the traditional method, single-layer colloidal centrifugation (SLC), the

swim-up method (SU) and utilising microfluidics where the device is a series of channels in length and a sperm is picked out of the chamber end manually using a micropipette. From the series of experiments performed, it was reported that microfluidic sorting had either approximately the same or better values for sperm quality factors, particularly with relation to morphology, vitality, and DNA fragmentation. The cleavage and blastocyte rates were similar between SLC and microfluidics, although microfluidics was slightly lower. This was determined to be because of the small sample size of the sperms used which may compromise which one was chosen from the population. Therefore, this indicates that microfluidics can be comparable to current techniques for blastocyte production, but perhaps additional channels or design should be used to maximise the throughput of examined sperms.

A microfluidic device has also been made to improve the treatment time of ICSI for porcine sperms [114], and the study offered a comparison between the speed of a microfluidic device and a traditional microdroplet method for ICSI fertilisation in terms of treatment times.

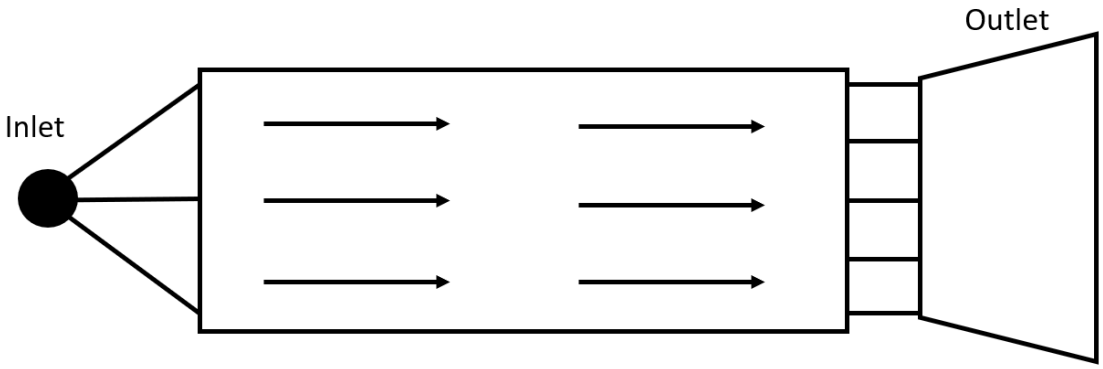

Figure 2.5: Schematic of sorting device utilised in [14] for porcine sperm for ICSI. Sperm are allowed to move passively from inlet to outlet.

The microfluidic device achieved a quicker treatment time by 82 s when a poor-quality sperm count was used; however, for normal sperm (2x10^2 cells/mL), there was no significant difference between treatment times. This implies that microfluidics may be more beneficial to be used for those with oligozoospermia, especially for increased treatment times as it seems to be easier to select a healthier sperm when microfluidics is used as a sorter.

Microfluidics have been used to test chemotaxis for sperms using a chamber with chemicals allowed to flow through certain sides of it (as it is in the shape of a hexagon) [115]. Due to 3 sides of the hexagon having a gradient, 3 separate gradients could be tested simultaneously, yet only 2 were tested in this experiment. Progesterone concentrations were studied at 100 pM and 1 mM where the 100 pM group had a small chemotactic behaviour towards the concentration gradient, but at 1 mM there was a larger chemotactic response. This is because of the chamber itself having a lower amount of progesterone, hence demonstrating that chemo-attractants can be used to influence sperm movement.

Although chemotaxis is thought to be short range, investigation has been conducted on thermotaxis also as a long range guidance mechanism for sperms [116]. Thermotaxis seem to only work on capacitated sperms as they are ready to fertilise. One such device was made and tested with a temperature gradient from 35 degrees to 36.3 degrees over 15 minutes [117]. It was reported that around 24-27% of the sperms moved towards the hotter area of the device by moving along this gradient with only 2% moving with the control temperature (no gradient). The optimal temperature range recorded was 35-36.3 degrees for the device while other temperatures performed well such as the 37-38.3 degrees temperature range.

2.6 Conclusion

Microfluidics is a powerful technique to capture and isolate a single sperm from a larger population. This also offers elimination of human involvement, for which, many techniques have been developed utilising microfluidics as the main platform. The literature has determined that it is possible to manipulate cells, including active cells by controlling active flows within microfluidic channels.

Microfluidic manufacturing techniques have also been explored and each of their niche use-cases have been identified along with evaluating their potential for commercial viability. For this application, replica moulding from 3D printed devices was seen as a useful tool to generate the required 3D geometry as well as micromilling to approach the fine resolution required for the device function while still being able to develop 2.5D geometries.

Imaging techniques have also been discussed as methods for potential automation of the device, particularly with regards to visual sensing of sperms in microfluidic channels. It is theorised that by integrating visual sensing techniques, the pressures within the system can be automated and the entire process can be completed without any human intervention.

Finally, a review was undertaken with regards to present sorting techniques to enrich a population of sperm. Due to the modular nature of microfluidics, it would be possible to integrate this into the currently developed device proposed in this thesis to enhance the selection procedure for ICSI.

3. Rapid Prototyping for 3D Microfluidic Devices

3.1 Introduction

Developing an inexpensive method of manufacturing microfluidic moulds for proof-of-concept testing is a useful tool in developing a new technology from basic conceptual stages all the way up to a prototype. Typically, microfluidics requires clean room facilities and high capital cost photolithography techniques, so finding solutions that have the potential for rapid prototyping to reduce either the capital cost of expensive manufacturing machinery and/or eliminate the need for cleanroom facilities for mould manufacture is paramount. In this chapter, two manufacturing methods are explored: femtosecond laser ablation of a steel mould and low force stereolithography (SLA) 3D printing as they share the design characteristics to allow for trapping and isolation of singular cells from a larger population. The steel mould is analysed for device replication using a PDMS as it is a novel technique for manufacture, particularly at relatively large sizes for what the technique is normally used for. Demonstration of the requirements for the manufacturing of PDMS devices is also discussed for the 3D printed mould, particularly with reference to the specific requirements for the target design to achieve good replication of the mould.

3.2 Materials and Methods

Commercially available 430 grade ferritic stainless-steel discs (50 mm diameter, 0.7 mm thickness, surface roughness 0.197 µm) were ablated using a femtosecond pulsed laser (Satsuma from Amplitude Laser) and was used to ablate the channels directly onto the steel mould as a destructive manufacturing technique (Lasea Multi-Axis Micro Machining Centre). The full manufacturing process and laser parameters are discussed more comprehensively within [25]. Briefly, a design was developed in SolidWorks CAD software (Dassaut Systèmes) with main channel dimensions of 300x300 µm square channels and a gate restriction reducing the dimensions to 100x100 µm linearly as a 3D structure. The CAD model was sliced using the Autodesk ArtCAM software (Autodesk, Inc.) and machine code was generated using the laser control software Kyla (LASEA). A Raster Mode scanning strategy was utilised with 4 lines at 45-degree angles in each layer with no contouring of the geometry, with a 4 µm lateral overlap for each laser pulse. Lasering was performed at room temperature and atmospheric pressure with a processing time of 150 minutes.

Including replication, vacuuming, and curing of the PDMS devices, the entire process took approximately 6 hours.

Subsequently, a scaled-up version of the design was 3D printed using a Form 3+ SLA 3D printer (Formlabs) with main channel dimensions of 3x3 mm and descending gate dimensions of 500 to 100 µm with 5 gates total. 3 gate types were designed with the gates positioned at the top, middle and bottom of the channel respectively to evaluate the ability for removal of the PDMS from the structure. A CAD model was again developed in Solidworks, converted to a .STL file and imported into the PreForm (Formlabs) software, and then uploaded directly onto the 3D printer. The resin used for printing is White Resin (Formlabs, Product Code RS-F2-GPWH-04) as this supports printing of down to 50 µm resolution. Once printed, the moulds were cleaned with agitated Isopropyl Alcohol (IPA) fluid using the Form Wash (Formlabs) for 10 minutes. Any remaining large pieces of debris were removed using tweezers manually to clean the device surface. After first replication tests, devices were UV cured for 30 minutes, then 1 hour using the Form Cure (Formlabs), and then again oven cured for 48 hours at 60°C for the final replication tests.

PDMS (SYLGARD® 184, Dow Corning, MI) was prepared as a mixture of 1:10 ratio of curing agent to elastomer. The mixture was dessicated under a vacuum of -0.8 bar for 60 minutes before pouring over the mould. Curing time was either from 45 minutes at 100°C as recommended by the manufacturer for the steel mould tests and 3D printed mould tests, as well as 24 hours at 25°C for the second 3D printed mould tests with peeling of the replicated structure performed manually.

3.3. Results and Discussion

3.3.1 Laser Ablation Manufacturing Method

An image of the stainless-steel mould is illustrated in Figure 3.1 below:

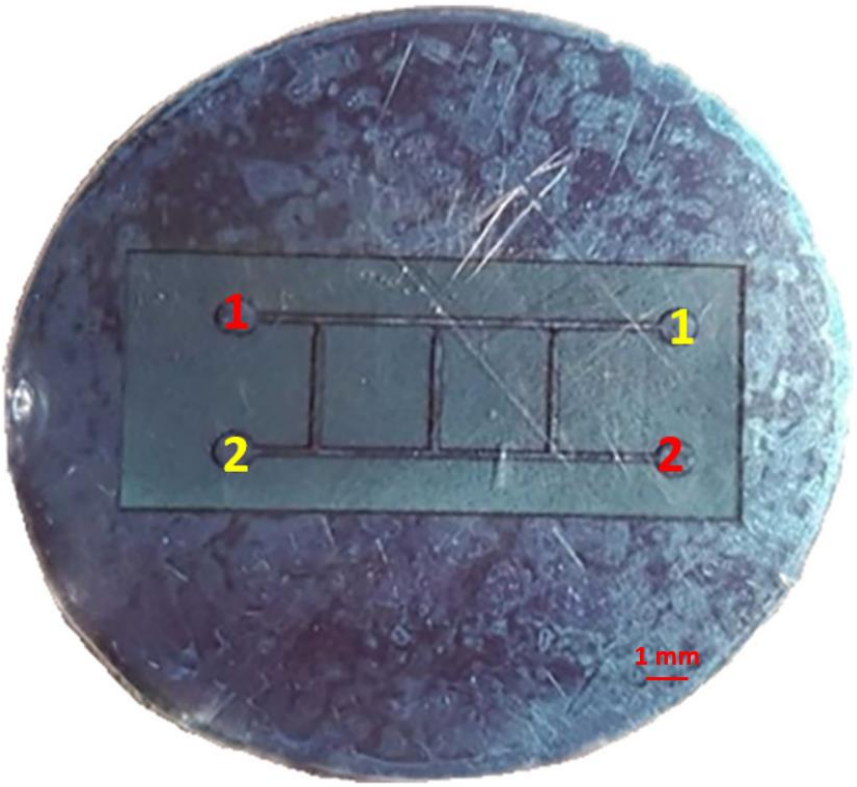

Figure 3.1: View of the stainless-steel mould manufactured from laser ablation [18].

The mould shows the typical structure required to trap and release cells with 2 inlets marked in red and 2 outlets marked in yellow. The gate restrictions are on the '1' side at the channel junctions which is considered the bulk flow area, while the control flow is on the '2' side.

Two main areas were examined for their replication ability in relation to the steel mould and were analysed using an Alicona G4 InfiniteFocus (IF) system to obtain the surface profile measurements. These areas are across the main channel areas and along the gate restrictions, which is of particular importance due to any undershoots, meaning that the object of interest may now pass through the gate leading to it being unable to be captured. The surface measurements are shown in Figure 3.2 below.

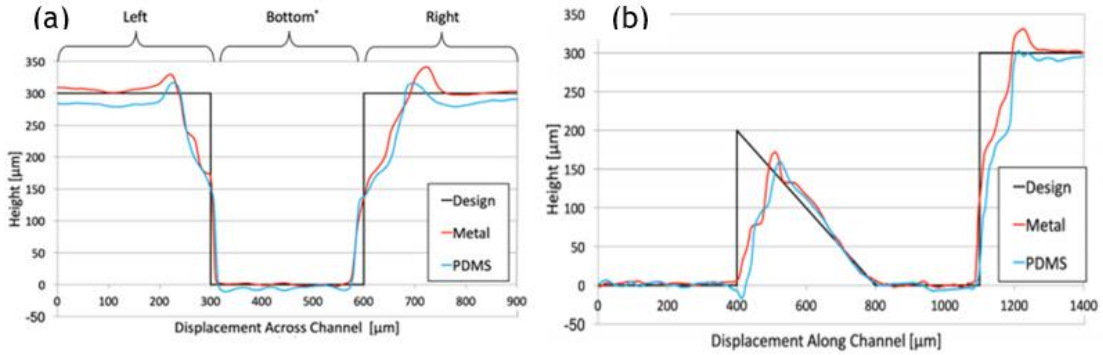

Figure 3.2: Surface measurements of key structures in the device. 3.2(a) is across the general 300x300 µm channels in the device. The bottom of the channel has been truncated 30 µm on either side to remove large errors at the walls of the channel. 3.2(b) is of the gate restriction in the device [18].

Figure 3.2(a) highlights the replication ability of the mould within the main channels. The replication of the channel is fairly good along the bottom of the channel with only small fluctuations occurring along the surface. The channel wall, however, exhibits much worse replication with the tops of the channel forming two angles at the edges, rather than being perfectly vertical. This is due to the raster scanning strategy of the laser where it decelerates and accelerates at channel edges in the raster scanning mode. This leads to additional laser pulses reaching the surface at these points, thus causing more ablation at the channel edges, along with the spot size of the laser not being infinitely small. This means that if the position of the laser is directly over the channel walls, the edges of the laser will still have a weaker ablation effect at the edges of the channel, where the extremities of the laser spot are hitting the surface causing the tops of the channels to also be ablated. This overshoot, however, due to the requirements of the design, was deemed acceptable as the main channel shape does not have an overall impact on the design function. Specifically, the metal mould has a maximum undershoot of 150 µm vertically reducing to a 0 undershoot almost linearly across a distance of 87 µm where an overshoot occurs. Because of the shrinkage of PDMS during thermal curing, this undershoot is slightly higher in the replica by up to 20 µm when compared to the steel mould. Optimising the scanning strategy would lead to better channel replication, notably by adding 'off times' during scanning when the laser is decelerating/accelerating during direction changes [118], or by using PID controllers to minimise errors in the galvanometer's movement [119].

There is also an undershoot of a maximum of 42 µm at the edges of the channels (at 200 µm and 700 µm displacement based on Figure 3.2(a)) for the metallic mould, which are in

turn replicated in the PDMS with 30 µm overshoot that is lesser again due to the shrinking of the PDMS during thermal curing. This is likely a result of channel debris forming around the edges of the ablation from the long exposure due to the raster scanning mode mentioned previously.

Figure 3.2(b) shows the replication ability of the mould for the critical gate restriction. Similar effects to the square channel can be seen along the vertical walls as previously explained, and this has led to a fairly significant undershoot of the design height at the gates due to this being designed as another vertical wall and converging into a point as a sharp geometry. This further led to the tip of the gate, which was intended to be 200 µm high, being overshot by 28 µm by the metal mould vertically and has a horizontal error of 110 µm. This is again closely replicated by the PDMS but with larger errors due to the shrinking effect with a vertical overshoot of 40 µm and horizontal overshoot of 122 µm. For both the PDMS and steel moulds, however, the angled surface was fairly well-replicated up to the tip of the restriction. This means that, as a potential for redesign with this method, rather than having a tip there, there should be a ramp on either side, and a flatter surface at the top of the channel.

The Root Mean Square (RMS) deviation of the height of the metal and PDMS compared to the design height was calculated and is displayed in Figure 3.3 below:

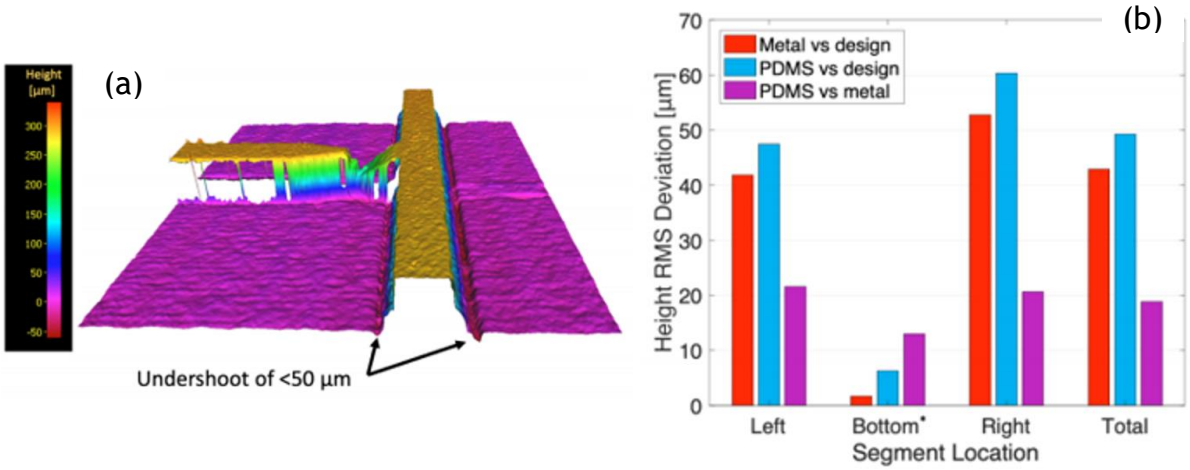

Figure 3.3: Alicona surface measurements of the mould and RMS values for the device. 3.3(a) shows the scan of the mould across one of the gate restrictions with the colour showing the relative height of the mould. 3.2(b) is the RMS deviations in the height between the original design, the metal and PDMS across the main channel [18].

Figure 3.3(a) offers a general overview of the heights and surfaces that were manufactured in the steel mould, along with highlighting the undershoots of the design horizontally. The general shape of the main channels can be seen to be almost trapezoidal rather than square due to the previously discussed undershoots. Figure 3.3(b) demonstrates the RMS deviation of the device for the main square channel (calculated from the values and geometry shown in Figure 3.2(a), including indications of the Left, Bottom and Right locations). Again, the values were truncated at the channel walls by 30 µm to remove large errors and give a representative RMS along the channel bottom.

At the left and right segments of the channels, the deviation is large, at 41.9-52.7 µm and 47.5-60.4 µm for the metal and PDMS channels respectively due to the previously explained errors during the manufacturing process. Along the bottom of the channels, however, the RMS values were, as expected, small: 1.68 µm and 6.3 µm for the mould and PDMS. Across the entire channel, the RMS error of the metal mould was 42.9 µm and 49.3 µm for the PDMS replica.

Finally, the RMS was calculated between the PDMS and steel mould to evaluate the shrinkage that occurs during the curing process. Across the entire profile, the total RMS difference between the metal and PDMS was found to be 18.8 µm. By determining the RMS difference of the PDMS to the mould, the original design could be altered to manage these effects to better replicate exactly the desired geometry. This, combined with further optimisation of the laser strategy, could greatly improve the RMS values along with the replication of the critical gate restriction structure as well as the main channels across the entire device.

3.3.2. Low Force Stereolithography 3D Printing Methods

Due to 3D printing technology rapidly evolving, a pilot study was developed to determine its effectiveness at developing microfluidic channel-like structures along with its ability to replicate PDMS for the individual isolation/release structure. The entire three channels printed are illustrated in Figure 3.4 below:

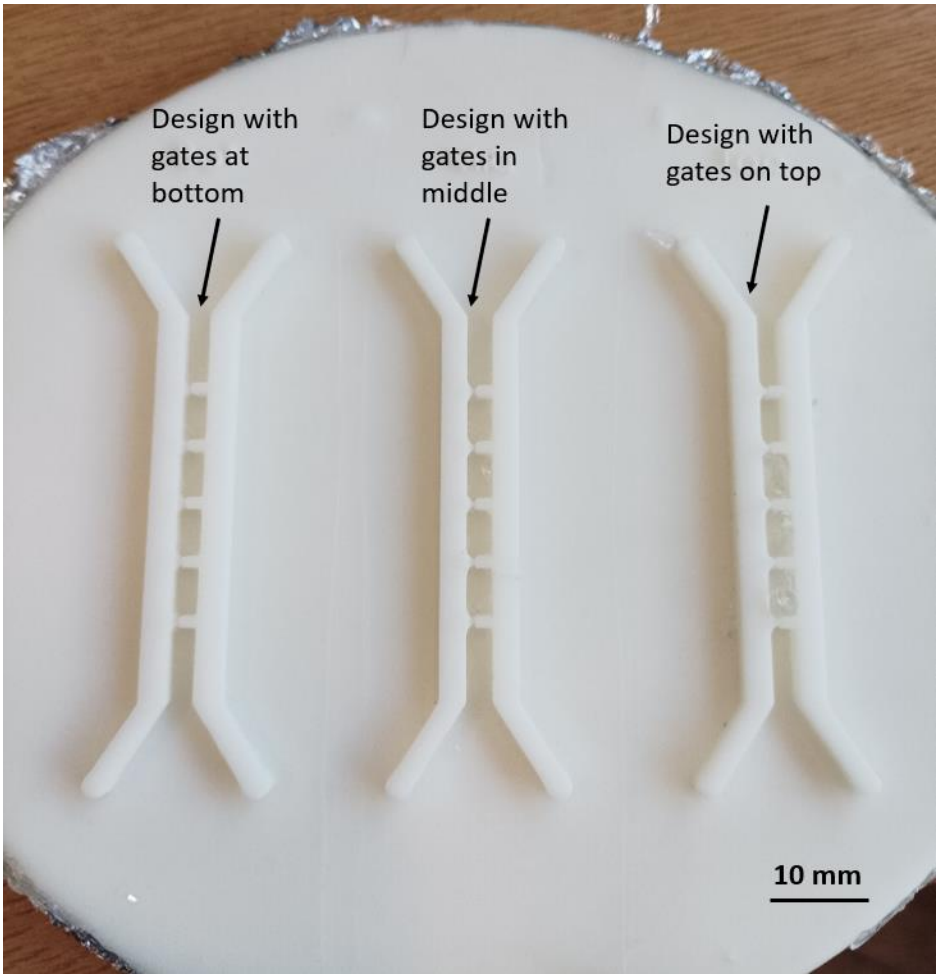

Figure 3.4: 3D printed mould design of the capture structures. The overall size of the entire print is 140 mm in diameter. Main channel dimensions are 3x3 mm and gate restrictions are 100 µm up to 500 µm ascending by 100 µm for each gate from the top of the design to the bottom. Bot indicates the restriction is on the bottom. Mid indicates the restriction is in the centre of the channel. Top indicates the restriction is at the top of the channel.

Figure 3.4 shows the overall printed design with gate restrictions between each of the channels as a test for rapid prototyping scaled-up devices for experimentation with a total printing time of 5 hours and 30 minutes. The gate position relative to the channel is in the same place for each of the 3 designs and is further displayed in the subsequent Figure 3.5:

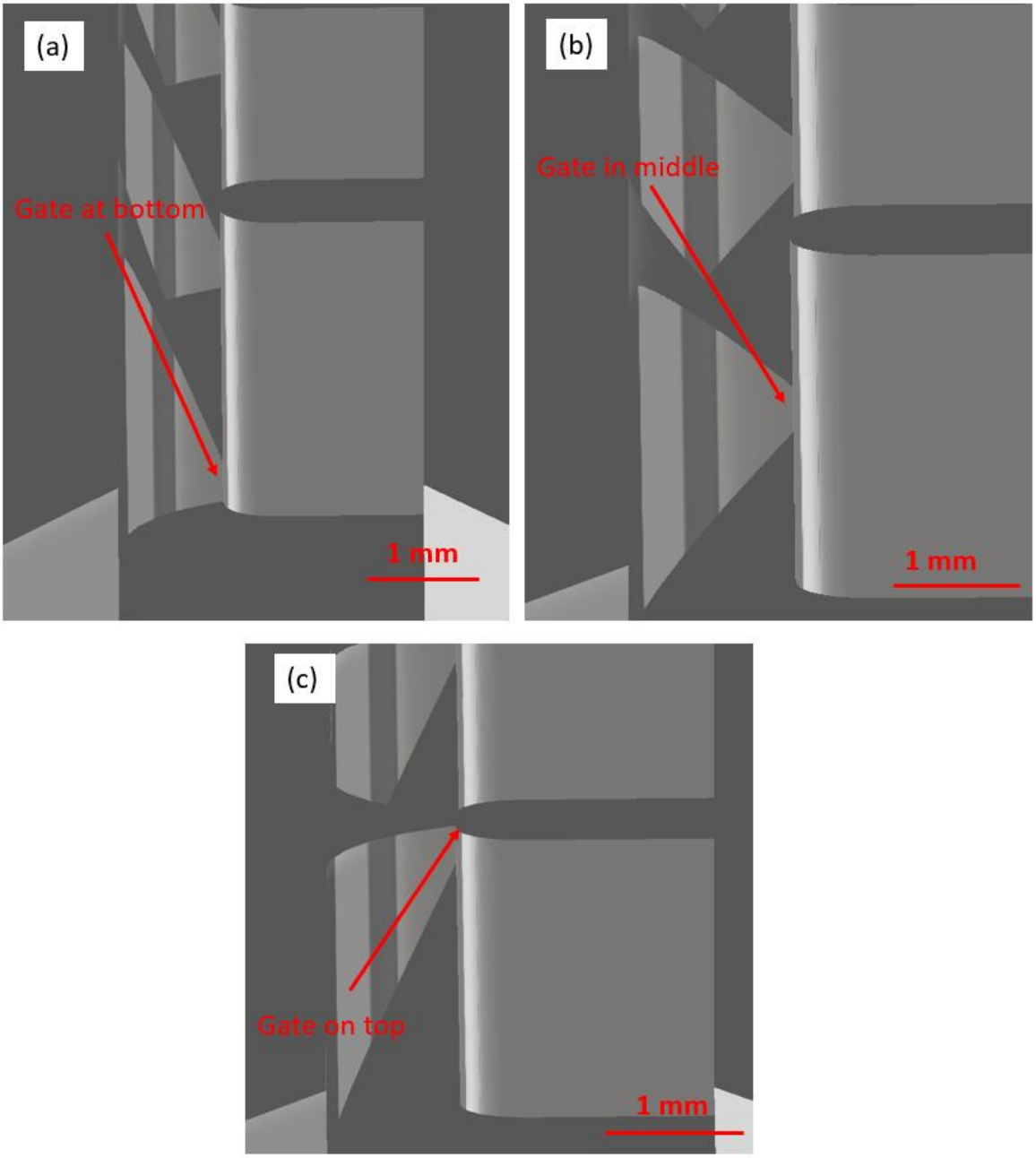

Figure 3.5: Various gate positions within the design for the 500 µm gate. 3.5(a) Shows the gate position at the bottom of the channel. 3.5(b) Shows the gate position in the centre of the channel. 3.5(c) Shows the gate position in the top of the channel.

Figure 3.5 exhibits how the gates are positioned between each of the three designs. There is a linear reduction in height from the main bulk channel for all designs down to the restriction, with a sharp increase after back to the 3 mm height. This means that the middle and top gate positions have overhangs, which, when the PDMS is poured, fills underneath the channel, while for the bottom channel it is similar to conventional mould manufacture/PDMS peeling techniques. Initial replication was tested without curing the mould, which led to much of the PDMS surface not curing and not successfully replicating the internal structures. As such, the long UV and thermal curing processes were used to

evaporate any active monomers remaining on the surface of the 3D print [120]. Subsequently, primary testing was performed using the fast cure method at 100°C in 45 minutes and first conducted with the 3D printed design. In this process, for all the designs, there was a rupture during the peeling process surrounding the gate structures as shown in Figure 3.6:

Figure 3.6: Rupture across the channel centre for the top gate design with the 45 minute at 100°C thermal curing method for the PDMS. The top of the device thickness is 2 mm.

Figure 3.6 shows an example of what occurred for each of the PDMS peeling processes for each of the designs. There was tearing around the key structure of the device where peeling was not feasible for anything past the first gate particularly due to the nested inner structure of the gate designs. This was thought to have been due to the curing processes, giving PDMS a much lower elongation limit prior to rupture [121]. To remedy this, the curing process was changed to 24 hours at 25°C as this allows the PDMS to be stretched further prior to failure. This is because the failure mode was unlikely due to the applied pressure but rather due to the high surface tension between the gate areas and the channel

walls and the inability to access them effectively before the PDMS ruptures. By changing the curing ratio, and letting the PDMS stretch further, there was better access to interact with the central geometry, as illustrated in Figure 3.7.

Figure 3.7: Replicated structure of the 3D printed mould for gates in the bottom position with thermal curing at 25 °C for 24 hours. The top of the device thickness is 5 mm.

Figure 3.7 displays a successful peeling of the structure for the bottom gate design. Peeling the middle and top designs from the mould was still unsuccessful due to tears forming from the underlying PDMS, rather than just separating cleanly from the mould, which then propagated along the rest of the structure. This means that the middle and bottom designs were deemed unviable at this stage for replication.

The bottom gate design was effectively peeled because of the ability to access the central structures due to the theorised increase in allowed elongation, along with the addition of further PDMS to increase the thickness of the device by 3 mm compared to the first test.

This allowed the device to be released, however, as seen in figure 3.7, plastic still occurred around the central structures as indicated by the lighter regions replicated structure. This plastic deformation meant that the 100 µm gate was damaged during peeling, and all the central structures were inaccurate when compared to the original mould. The restrictions, however, were still able to be developed, and the device would still be suitable for analysing capture of objects/cells with diameter greater than 500 µm. Therefore, for a potential redesign, it would be useful to round the edges of the device to allow better access during peeling and to reduce the surface tension of the central structure for easier peeling. Better peeling techniques may also aid with reducing any damage to the structure such as performing the process much slower and applying a constant force to alleviate the device from the mould.

3.4 Conclusion

A novel rapid prototyping technique has been developed to produce microfluidic moulds using a red femtosecond laser and has been extensively demonstrated throughout this chapter. This method allows for quick production of microfluidic devices if laser ablation facilities are available but not traditional microfluidic manufacturing facilities. Overshoots were observed at channel edges and can be attributed to low laser parameter optimisation. Indeed, more optimisation of micro-processing by minimising the impact of the raster scanning method and optimising the laser movement control would lead to better replication of 3D features. Additionally, low force stereolithography 3D printed moulds were tested for this particular design, resulting in the conclusion that the peeling of the PDMS replica was a difficult process with ruptures occurring when curing it at 100°C for 24 hours, mainly due to the nature of the design, with many closed-off features embedded around the central structure. Therefore, the most ideal method tested in this chapter involved curing the PDMS for 24 hours at 25°C to allow for more elongation of the device prior to rupture. The gate designs in the middle and top unsuccessfully peeled; however, the gate designs in the bottom were effectively peeled from the mould, although not without some plastic deformation occurring.

4. Single-Object Isolation and Retrieval Utilising Microfluidics

4.1 Introduction

Capturing single objects has been performed previously with microfluidic devices, however isolation of the single objects from others is rarely attempted due to the continuous nature of fluid flow. Most current methods can isolate an object type but cannot extract a single object from a group. In this chapter the design and development of a countercurrent microfluidic method is analysed for single object isolation. Simulation of the design is developed for key parameters such as gate sizes (2 µm and 30 µm), fluid speeds and their resulting pressures within the design. A proof-of-concept experiment is performed using microbeads to demonstrate the validity of the method for single object isolation with 100 µm gates.

4.2 Methods: Microfluidic Design and Simulation Methods

The microfluidic device is simulated as two parallel channels with concurrent flows between them. The gate sizes examined are 2 µm (smaller gate size) and 30 µm (larger gate size). Each channel has widths of 300 µm for the larger gates, and 100 µm for smaller gates, with the addition of 100 µm width channels between them. Moreover, several designs were explored to examine the impact between the parallel channels, such as the distance between them, and whether adjusting the distance between each gate is impactful.

The gate dimensions are different from those of other areas of the device where the channel entrance begins at the edge of the channel and decreases as a curve to 20 and 5 µm across a distance of 150 µm. This is to provide a way of capturing a singular object as only one will fit into the gap at the end, thus sealing it and reducing the pressure difference at this gate so that any other object that follows will continue moving down the bulk flow channel. Should the captures fail on the first pass, there is potential to allow for objects to loop back through the system or to continually add objects into the flow within the left channel.

The device then operates in three stages. The first begins with high pressure in the left channel and low in the right channel to allow the objects to be trapped due to the flow

moving between the channels. Each object captured then blocks the channel to prevent others from entering, while also being held in place by the consistent pressure difference. Once trapped, the flow is then switched as the second stage consists of low pressure on the left, but high pressure on the right. Due to the pressure gradient across the channel, objects closer to the left inlet are held in place, while objects further from the left inlet are pushed out. The final stage is increasing the pressure of the right channel sequentially until each of the objects has been pushed out individually, allowing for the retrieval of each one isolated.

To test this, simulations were developed using COMSOL Multiphysics. Flow was considered laminar for the simulation because of the low Reynold's number (with the maximum flow rate expected to be 3200 μm/s leading to a Reynold's of 0.0734 or <<1) as calculated by:

$$Re = \frac{\rho u d}{\mu} \quad (4.1)$$

where ρ is the fluid density, u is the average fluid velocity, d is the characteristic channel diameter and μ is the dynamic viscosity for which all fluid properties are considered to be those of water. All other velocities are lower so the simulation of flow for each stage can always be considered completely laminar for all fluid flow. The fluid motion modelled by COMSOL is found using the reduced form of the Navier-Stokes equation where the transient and inertial terms are ignored, as well as any additional forces not present, leading to:

$$\nabla p = \mu \nabla^2 \vec{\boldsymbol{u}} \quad (4.2)$$

where p is pressure and $\vec{\boldsymbol{u}}$ is the velocity vector. Finally, the boundary conditions for the simulation are firstly the laminar conservation of mass:

$$\nabla \cdot \vec{\boldsymbol{u}} = 0 \quad (4.3)$$

And then the no-penetration and no-slip conditions at the walls:

$$\vec{\boldsymbol{u}} \cdot \hat{\boldsymbol{n}} = u_n = 0 \quad (4.4)$$

$$\vec{\boldsymbol{u}}_t = 0 \quad (4.5)$$

where $\hat{\boldsymbol{n}}$ is the unit normal vector to the wall, u_n is the normal velocity into the wall and $\vec{\boldsymbol{u}}_t$ is the tangential velocity vector to the wall [95]. Ultimately, to examine how the objects move within the system, the particle tracking module was enabled, for which the particles are assumed to be spherical, and the drag force is determined by Stoke's drag law:

$$\vec{\boldsymbol{F}} = 6\pi\mu a\vec{\boldsymbol{u}} \quad (4.6)$$

where $\vec{\boldsymbol{F}}$ is the drag force and a is the radius of a sphere [96]. The radius of the spheres chosen were 30 µm for the larger gate sizes, and 5 µm for the smaller gate sizes to examine the ability of the capture-release mechanism for varying objects. The number of particles released in most cases was 30, only increasing for the alternative design examined to 100.

The simulation performed was 2D to determine the viability of the mechanism as ceiling effects would only require an increase in pressure, while, due to the fluid being laminar, it would follow the same streamlines. The only consideration when moving to 3D would be to ensure that the height of the gate is of the same size or less than the width so that objects can still be trapped.

Lastly, a limitation of the simulation would be that it was unable to demonstrate what happens with a blocked channel. However, it is assumed that once the channel is blocked, the pressure difference is eliminated. As such, each of the possible scenarios was simulated one by one, where once a particle reached a gate or an outlet, they were left to freeze in place to track their general movement as well as the general pressure trends required to achieve the trap/release mechanism.

The microfluidic mould for the microfluidic device was developed using the laser ablation of a steel disk [25]. Traps in the design were set to approximately 90 µm, and 100 µm diameter latex microbeads (Sigma-Aldrich, product no. 56969) were used as objects to be trapped with two syringe pumps to supply flow (InfusionONE Syringe Pump, New Era instruments). The microbeads were diluted in a ratio of 1:10 with deionized water for a concentration of 0.5 % solids to prevent clogging of the channels. The PDMS (SYLGARD® 184, Dow Corning, MI) was prepared by mixing the elastomer curing agent with the elastomer at a 1:10 ratio, desiccated for 30 minutes and then cured at 100°C for 45 minutes. The device was then removed from the mould and thermally bonded to a glass slide by

applying a thin layer of PDMS to the top of the PDMS and curing it in an oven at 100°C for 45 minutes again.

4.3 Results and Discussion

4.3.1 Capture Mechanism and Simulation

The first simulation that was performed was to check the ability of the mechanism to catch objects within each of the gates. This was tested for each of the scenarios being discussed as shown within Figure 4.1 below.

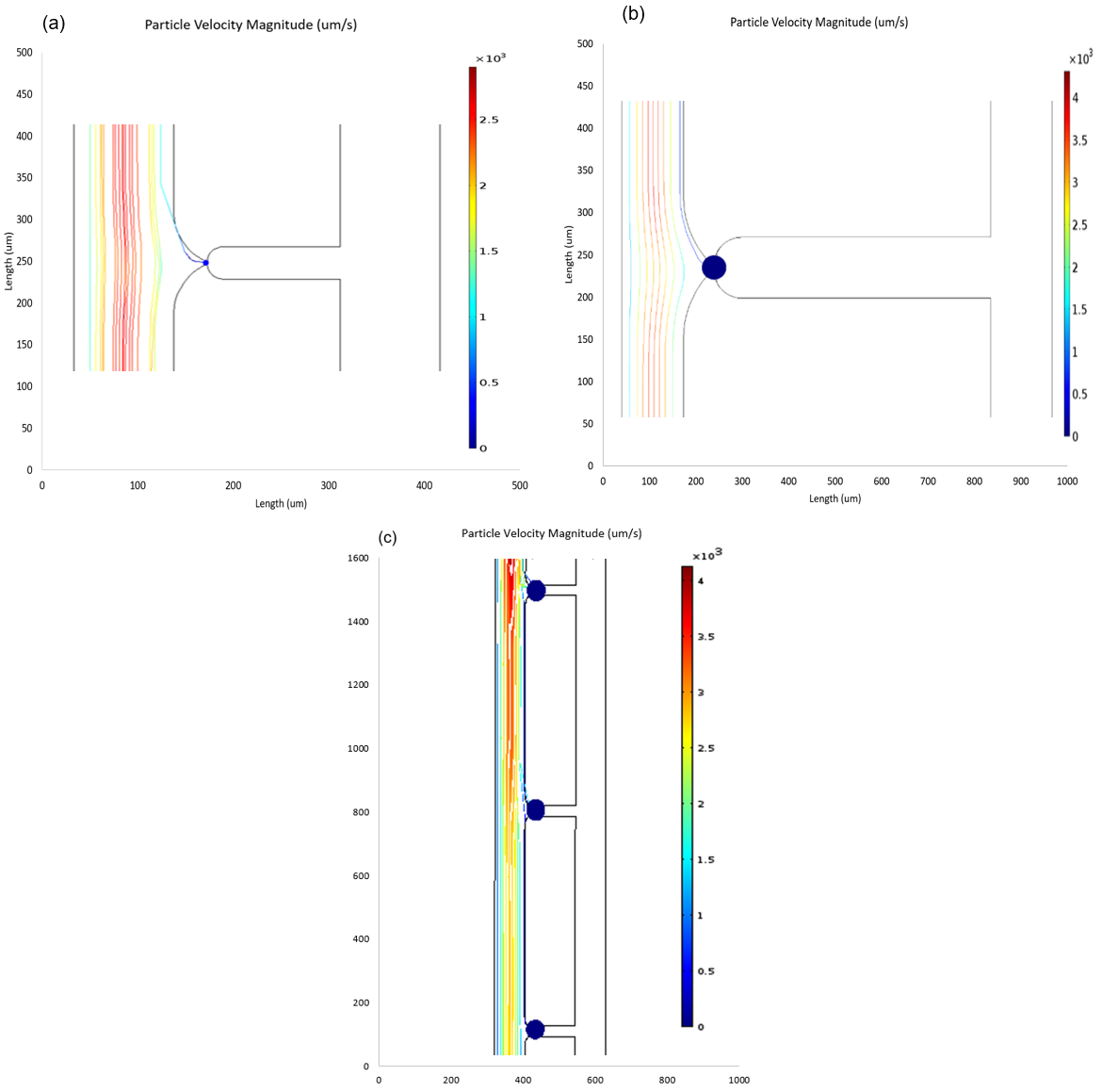

Figure 4.1: (a) The approach of a particle into the top gate with a 2 µm gate. (b) The approach of a particle into the top gate with a 30 µm gate. (c) The approach of particles being trapped into all 30 µm gates. All fluid velocities on the legend plots.

Figure 4.1 demonstrates, as predicted, that due to the pressure difference created from left to right, the fluid flow is also pushed that way. The parameter of Figure 4.1(a) has the fluid flow speed set to 1800 µm/s at the inlet in the left channel and 100 µm/s at the inlet in the right channel. However, the requirement to achieve capture in the channels with larger diameters shown in Figures 4.1(b) and 4.1(c) was much lower with 1000 µm/s being required at the inlet in the left channel while the right channel still being set to 100 µm/s. It should be noted that, as particles pass by empty gates, they are still drawn towards the right-hand side of the channel so that if the first gate is unable to capture, they will be much closer to each successive gate allowing for easier capture. If the particle is on the left-hand side of the capture channel initially, this effect is felt much less as can be seen in Figure 4.1(b). The curve of the path line of the particles is much more extreme the closer the particle was to the gate, and after passing, is closer to the gate side of the channel. The particles on the left also share this effect but to a much lesser extent.

Once the capture mechanism was determined, fluid flow parameters were altered for the channels by reducing the flow in the left channel and increasing the flow in the right channel. The gates are numbered from top to bottom, meaning that the first gate is at the top, the second is in the middle and third is at the bottom since this reflects the sequence of particle capture. Contrastingly, when speaking about the sequence followed by particles as they are released from the gates, it is a bottom to top sequence where the first particle to be released is that at the third and bottom gate. The particle flows within the 2 µm diameter gate channels for the bottom gate are displayed in Figure 4.2 below.

Figure 4.2 highlights the key concept of this mechanism. Figure 4.2(a) shows the pressure values at each point in the channel while Figure 4.2(b) shows the result of the pressure difference. The velocity of fluid in the left channel is set to 1000 µm/s and the right channel at 500 µm/s. It can be observed that only the particle in the third (bottom) gate is released due to the pressure difference, while the particles at the top are held in place as they are forced back into the gate. The velocity value for the right channel was found by performing a parametric sweep in intervals of 100 µm/s for the inlet velocity where in this setup, 500 µm/s was the minimum velocity required to dislodge the first object.

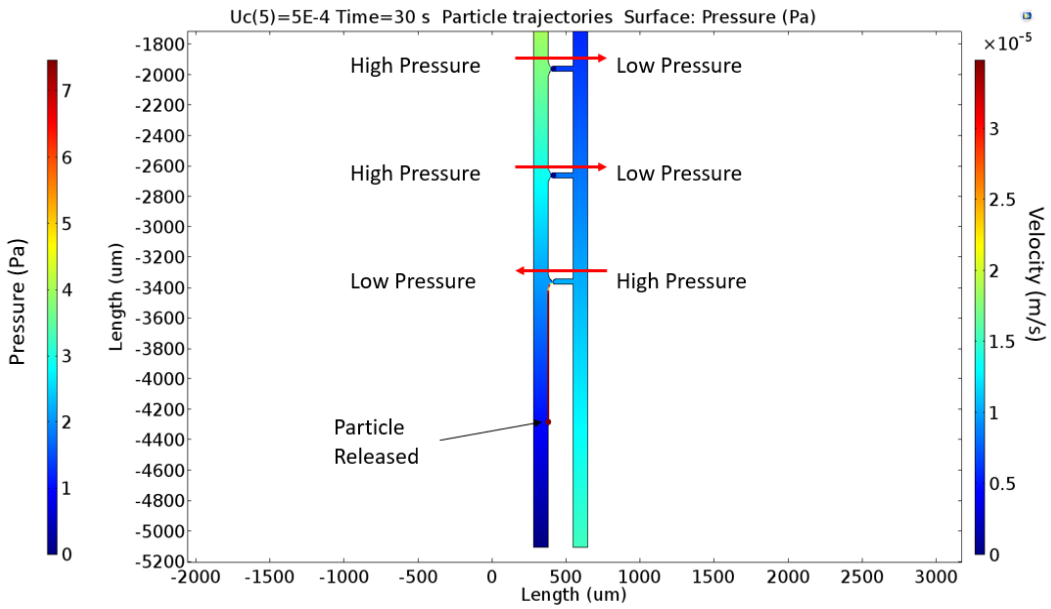

(a)

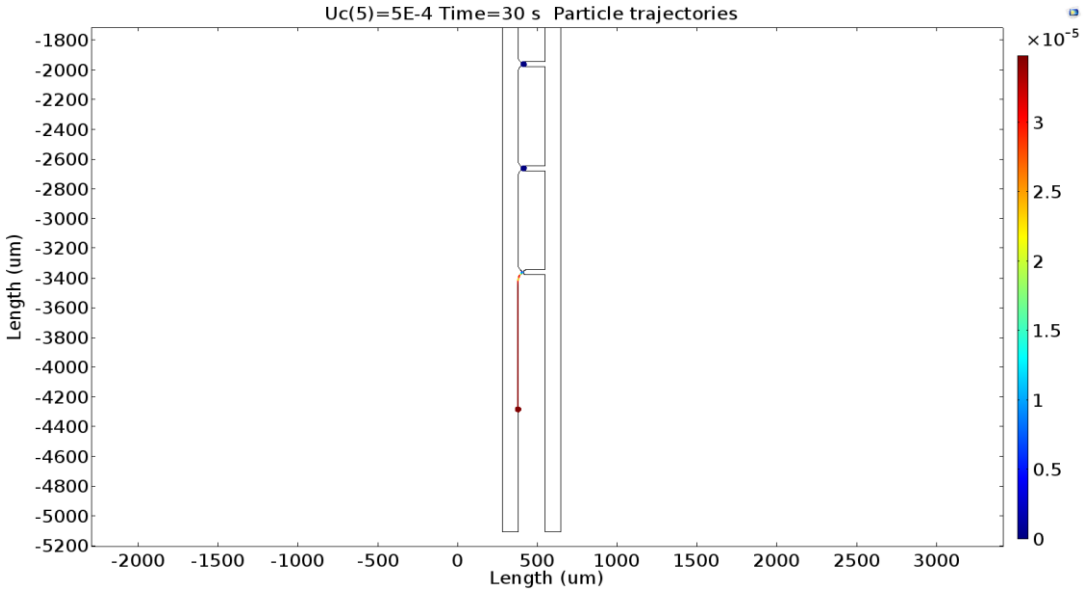

(b)

Figure 4.2: (a) Pressure values throughout the design for the release of the particle in the bottom gate. (b) Trajectory of the particles with the bottom particle moving to the outlet with other particles held in their gates.

This setup can be repeated by maintaining the velocity within the left channel, but then increasing it in the right one until the second object is released as shown in Figure 4.3 below.

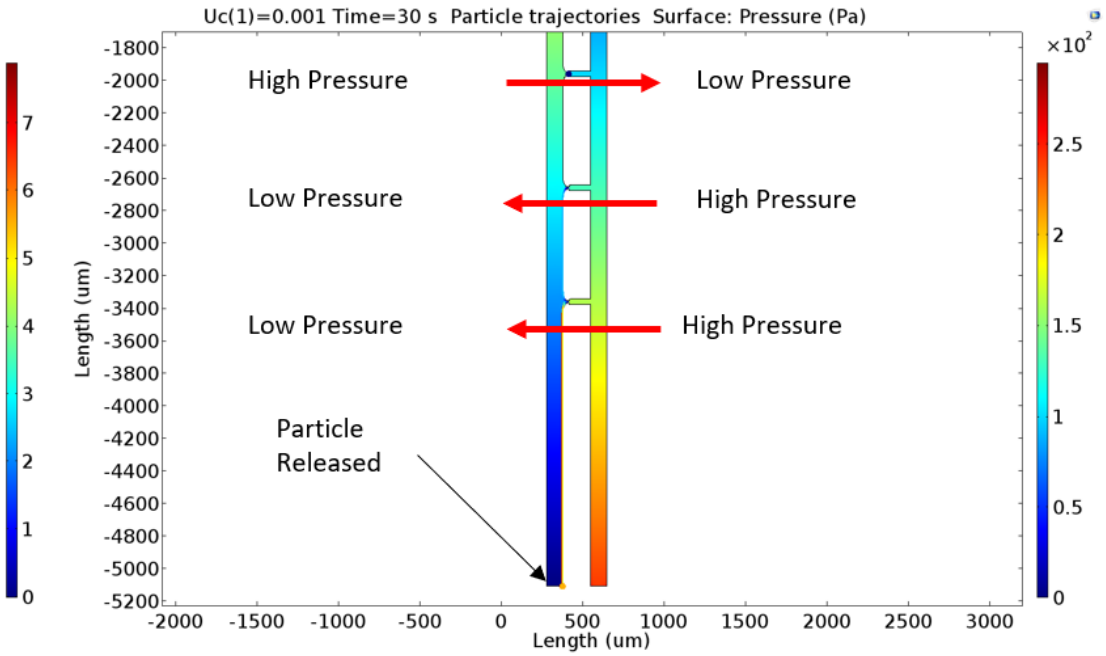

Figure 4.3: The release of the second gate for the 2 µm diameter gates with 1000 µm/s capture channel flow speed and 1000 µm/s control channel flow speed.

Once more, it is demonstrated that the top particle is held in place by the pressure difference while it is the second particle that is now released from the middle gate. This scenario keeps the fluid velocity the same in the left channel at 1000 µm/s while increasing it in the right channel to 1000 µm/s. It should be noted that this can be expected due to an almost linear distribution of pressure from inlet to outlet for each of the channels with the middle gate being at the centre of the length of the two channels.

Ultimately, the third release is demonstrated in Figure 4.4 by increasing the fluid velocity again. The final step then only requires increasing of the fluid velocity on the right-hand side enough to trigger the release of the final particle. For this scenario the left channel velocity was again kept at 1000 µm/s and the right velocity was raised to 1500 µm/s, which successfully released the final particle from the small diameter channels.

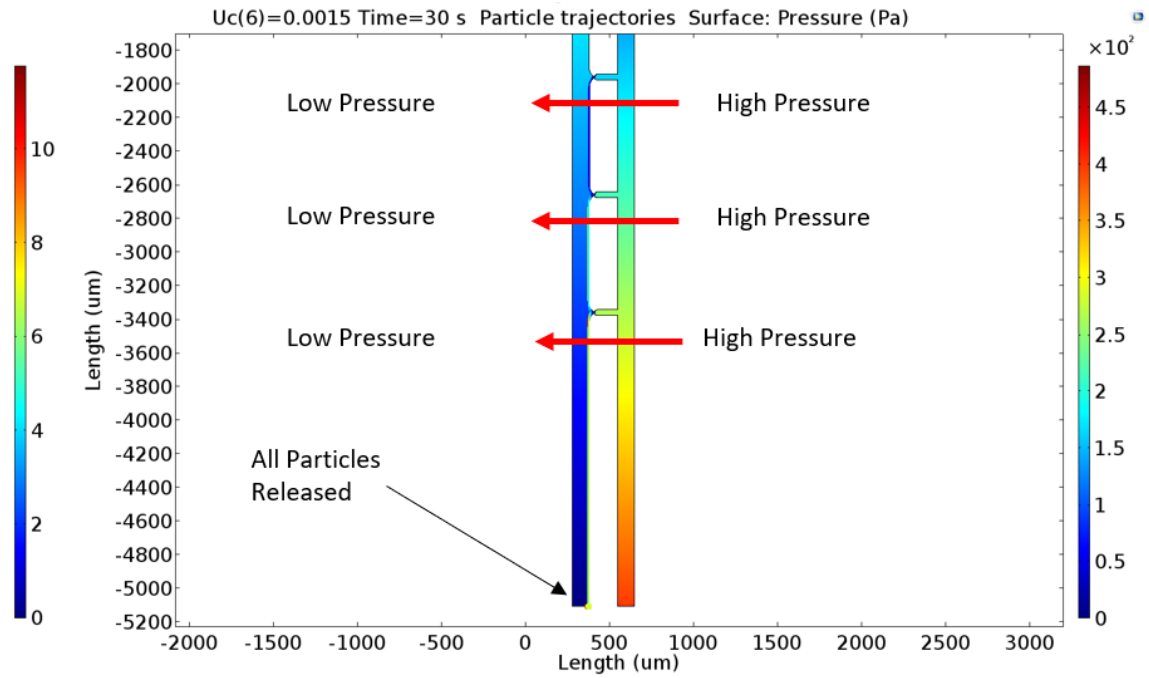

Figure 4.4: The release of the first gate for the 2 µm diameter gates.

Finally, the pressure differences at each gate are summarised in Figure 4.5 below with 1000 µm/s in the left channel.

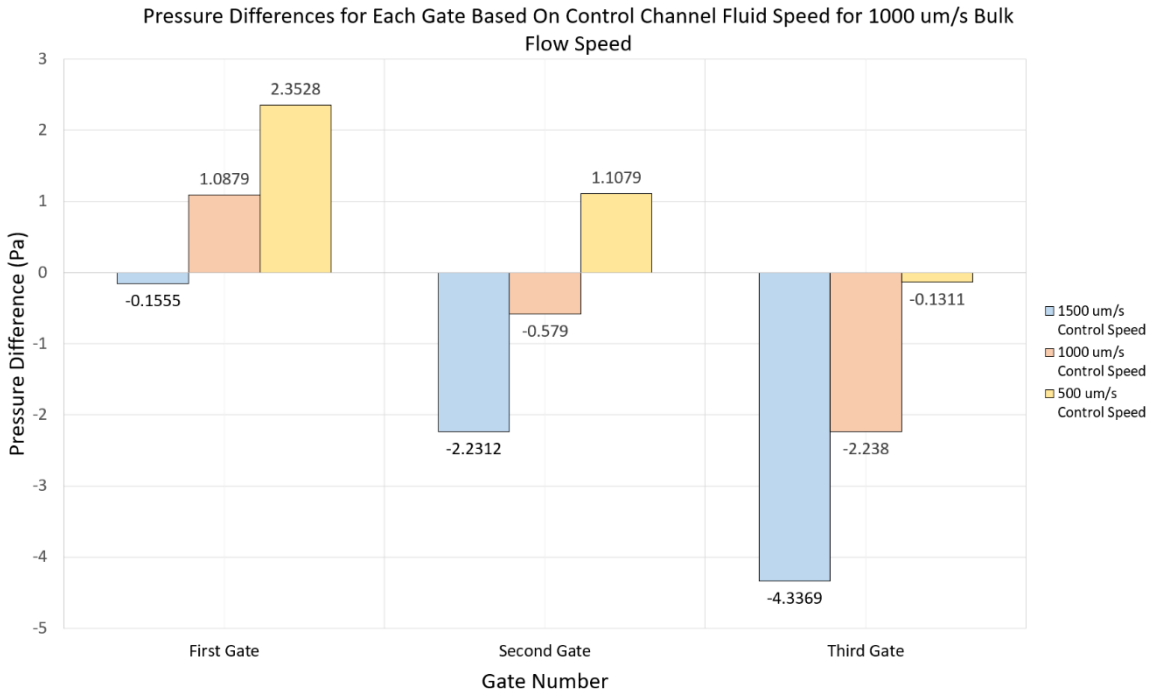

Figure 4.5: Pressure differences at each of the 2 µm gates for 1000 µm/s bulk flow speed.

The calculation for each of the pressure values is:

$$\Delta P = P_B - P_C \quad (4.7)$$

where ΔP is the pressure difference, P_B is the pressure in the bulk flow (left) channel and P_C is the pressure in the control (right) channel. The values are found by determining the pressure on each side of the gate: when the pressure is positive, the particle is held in place; when it is negative, the particle is released from the trap. The graph displayed in Figure 4.5 therefore shows that, if there is a small but negative pressure difference, then the particle is released, as was proven with the third gate at 500 µm/s control speed and the first gate at 1500 µm/s control speed.

To examine the impact of the bulk channel flow speed on the fluid requirements of the control channel, the simulation was repeated for a bulk flow of both 500 µm/s and 1600 µm/s which is illustrated by Figure 4.6.

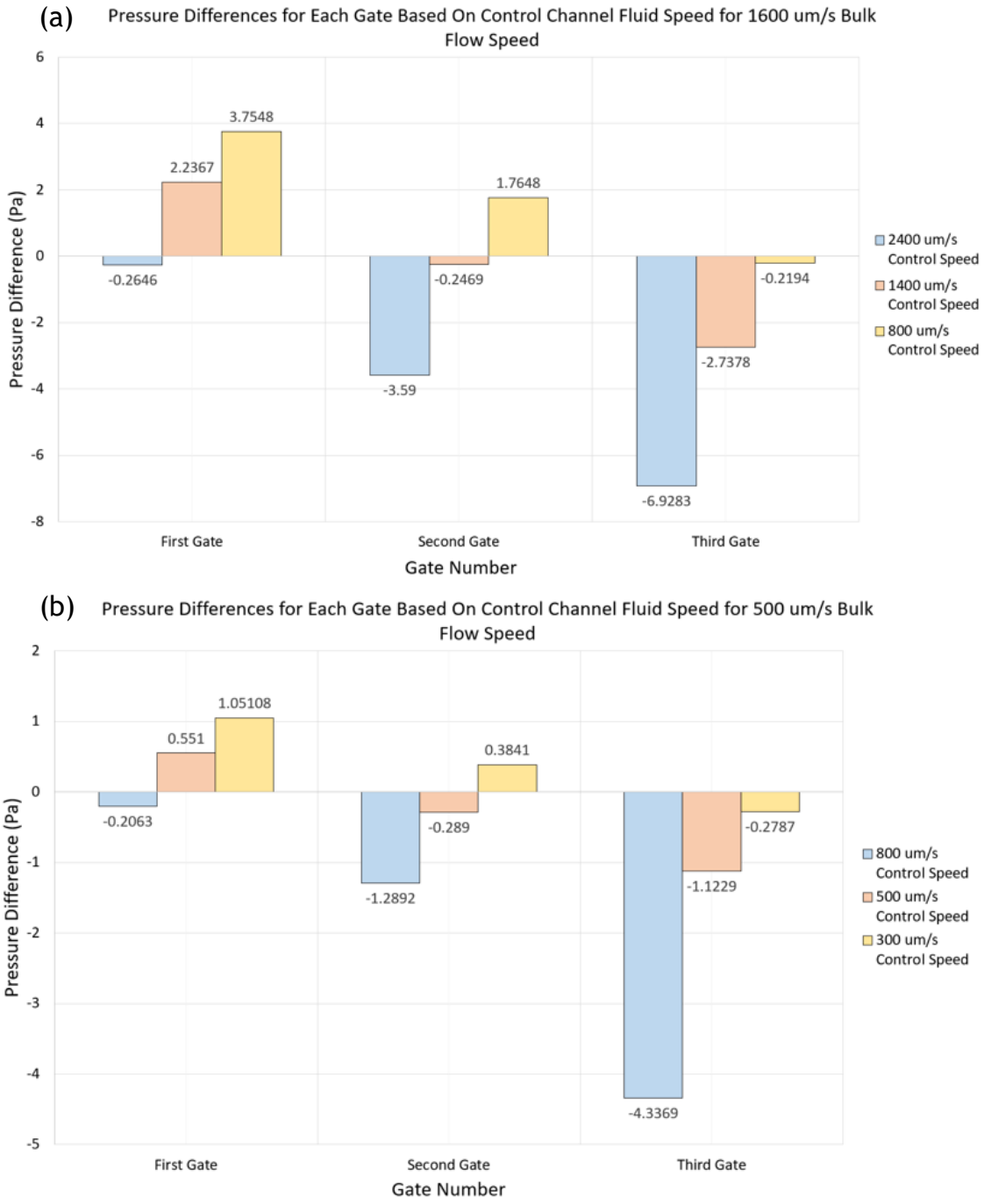

Figure 4.6: Pressure differences at each of the 2 µm gates at different control flow speeds. (a) Pressure differences at 1600 µm/s bulk flow speed. (b) Pressure differences at 500 µm/s bulk flow speed.

Figure 4.6 highlights the general trend requirement for the release mechanism of ΔP being negative but also shows some trend differences between the magnitude of the values reached. For example, for the third gate, the 1500 µm/s control speed to a bulk flow of 1000 µm/s resulted in nearly the same pressure difference as 800 µm/s to a bulk flow of 1500 µm/s, while the 2400 µm/s control speed to a bulk flow of 1600 µm/s had a pressure difference of 2.1 Pa higher. This means that the differences between the flow rates on each side do not indicate linearly the expected pressure differences as the geometric position

needs to be considered due to the nature of the pressure gradient across the length of the channel. It should also be noted that these were the minimum control speeds required to release the particles using the methodology outlined earlier. As such, there is a range where successful release can occur without disturbing particles in other gates. For instance, with the 1600 µm/s bulk flow speed, the third gate can be released anywhere from 800 µm/s control speed to 1400 µm/s control speed, at which point the second particle is released. This gives some lenience in the control required when implementing this method in physical models.

This same setup was then explored with the larger diameter gates with a 30 µm gap as can be observed in Figure 4.7.

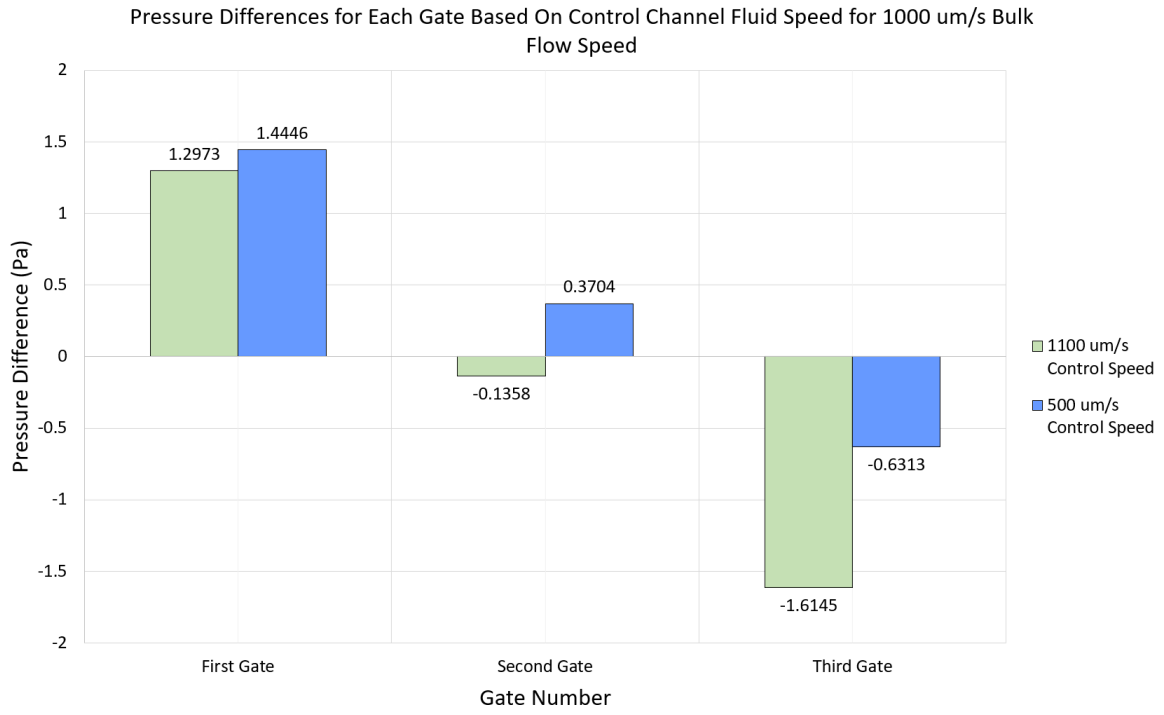

Figure 4.7: Pressure differences at each of the gates for 30 µm gate diameter for 1000 µm/s bulk flow speed.

Figure 4.7 above features the same trend of whether particles are held in place or pushed out depending on the fluid speed within the control channel as shown by the pressure difference. Interestingly, however, there was no way to release the particle within the first gate without moving into unrealistic control fluid speed values of above 6000 µm/s, which was a trend across all bulk flow speeds. This is due to the increased diameter of the gate allowing more fluid from the bulk flow channel and therefore leading to the channel

maintaining higher pressure regardless of the control speed, as well as the proximity of the gate to the inlet. There was a similar problem when trying to capture the particles with this gate size within the third gate (since the design is symmetrical). Because of the control speed being allowed to move down to very low values (to around 50 µm/s), a particle could still be trapped without increasing the flow within the capture channel to unrealistic values. This was also observed in other bulk flow speed channels as shown in Figure 4.8 below.

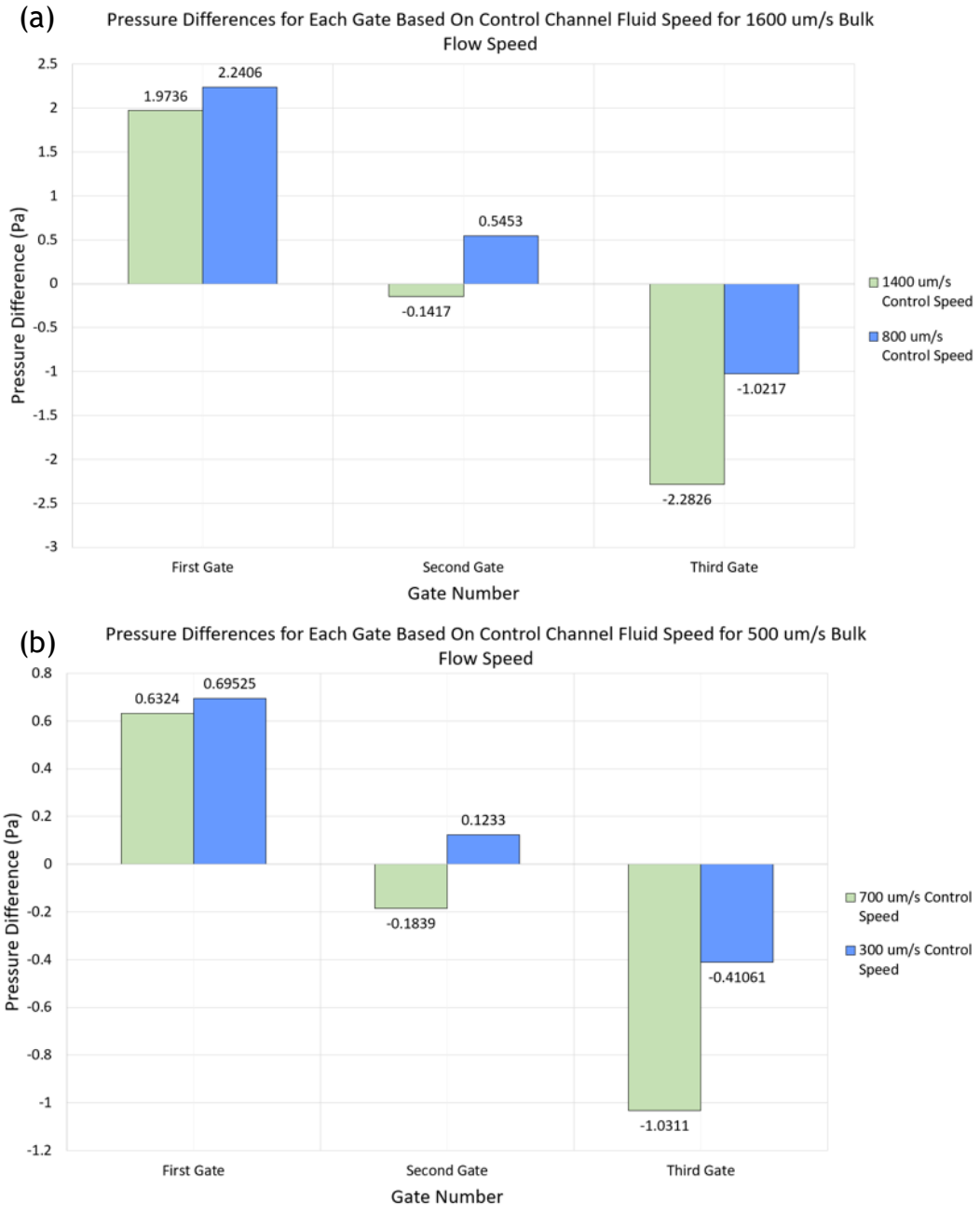

Figure 4.8: Pressure differences at each of the gates for 30 µm gate diameter at different bulk flow speeds. (a) Pressure differences at 1600 µm/s bulk flow speed. (b) Pressure differences at 500 µm/s bulk flow speed.

A similar trend can therefore be seen where the pressure difference can be reversed to negative for each of the gates, apart from the first gate where even with the 500 µm/s bulk flow speed, an unrealistic control flow speed, was required to release the particle from the gate at 4000 µm/s in this scenario. However, with the second and third gates, a similar approach can be taken for capture and release of the particles as with the smaller gate sizes. This trend nevertheless means that, to optimise the method and allow each side of the channel to influence each other better, or to use larger gate sizes, the gates themselves will need to be closer to each other and to the centre (i.e., away from the maximum pressure within a channel).

4.3.2. Modelling and Redesign

To observe this method optimisation, one final design was tested where the first and second gates are 600 µm apart, the second and third gates 1200 µm apart, the third and fourth gates 1500 µm apart and every additional gate up until the ninth increasing in distance apart by an additional 300 µm, along with 2 µm gate diameters. Demonstration of the capture using this design is highlighted in Figure 4.9 below. Inclusion of additional gates is due to the fact that many eggs are preferred to be collected for ICSI to be fertilised (in the region of 5-10 [122].

Figure 4.9(a) highlights the previous problem with the larger gates in the nineth gate, as without increasing the fluid velocity to unrealistic values, it is impossible to capture a particle within the bottom gate without allowing for the gate to be further from the control inlet. Figure 4.9(b), however, shows that particles can be captured in every gate up to the eighth with this setup so long as the simulation had enough particles within it. The number of particles in this scenario was increased to N = 100 to allow for more particles to move past the first gate and to allow each of the gates to pull the particles closer to the right side of the capture channel after moving past them.

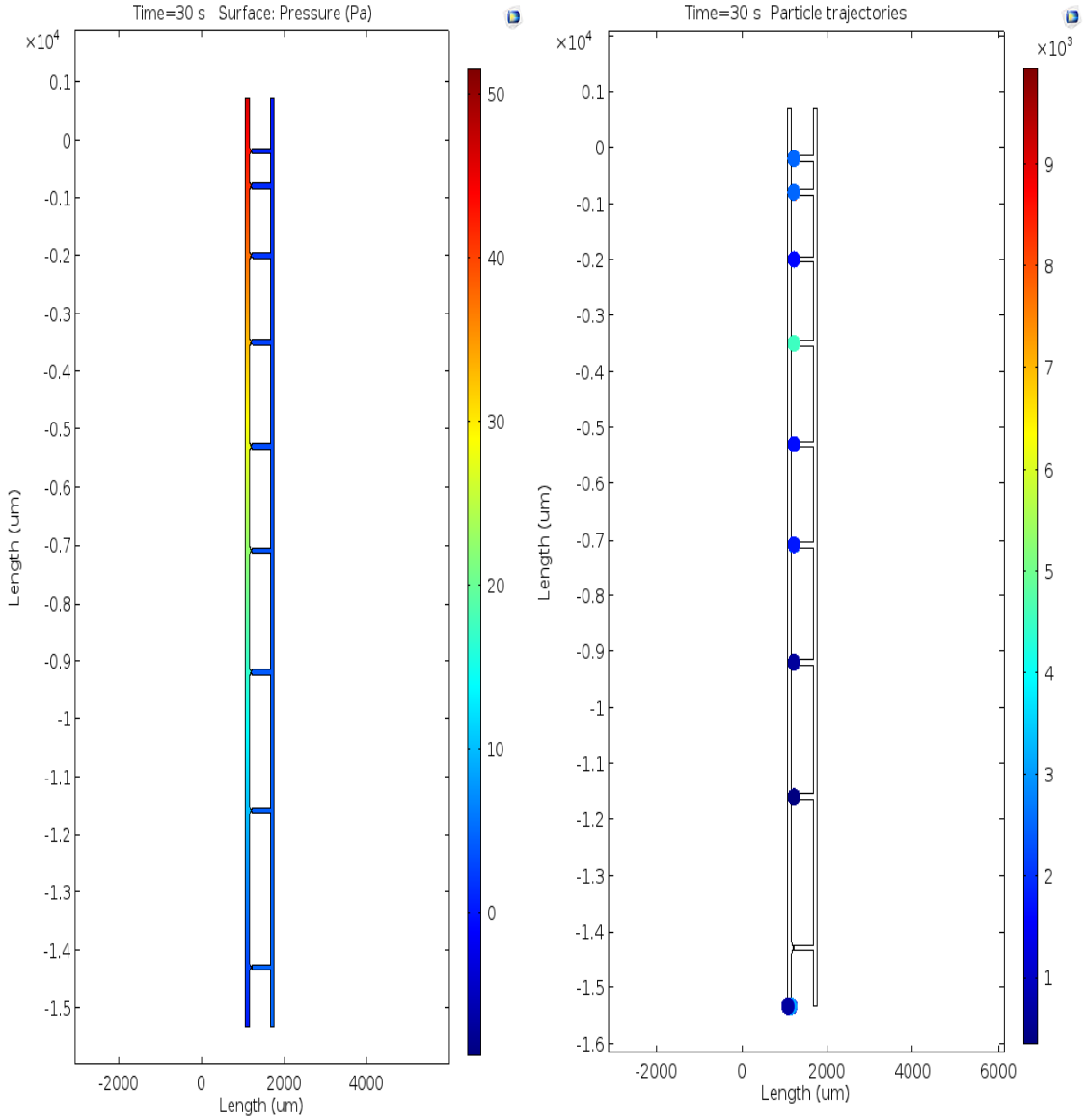

Figure 4.9: Overview of the design with distributed gates. Figure 4.9(a) highlights the pressure levels during the capture mechanism of the device. Figure 4.9(b) shows particles being captured in most gates of the design apart from gate 9.

The release mechanism was then explored as in the previous analysis for all 9 gates with the new geometry shown in Figure 4.10 below. 600 μm/s was chosen as the bulk flow channel speed due to the longer distance that the control channel must influence to release particles from higher number gates and to allow for easier switching of the flow direction.

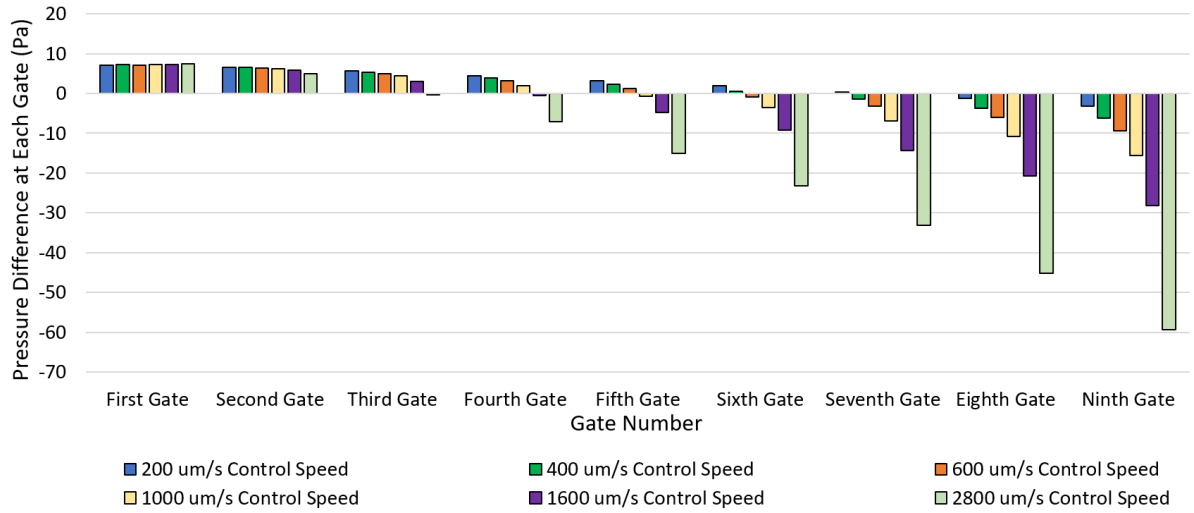

Figure 4.10: Pressure differences at all gates for the alternative design with 1600 µm/s bulk flow speed.

Figure 4.10 illustrates how the pressure differences between each side of the channel are impacted based on the location of the gate across the channel. Regardless of how low the flow speed was in the bulk channel; it was not possible to release the first and second gates individually. As such, the third gate should be considered the maximum distance that a gate can be from the control channel inlet which was at 200 µm/s control speed. The flow can then again be increased sequentially to release each particle successively to achieve the negative pressure difference required for release up to 1600 µm/s to allow for individual releases from gates 8 to 4 giving 5 gates in total that can be used with this method (considering that it is impossible to trap in gate 9 and 2800 µm/s is very high to release from gate 3). Not unlike the gates close to the control inlet, the two gates close to the bulk flow inlet were unable to be released. Interestingly, the pressure difference across gate 2 was found to decrease slowly but again unreasonable speeds would have to be reached, while the pressure across gate 1 was found to increase due to more flow moving across this gate as the others were 'sealed off'. This suggests that until a particle is released, the pressure difference increases across the channels that still have particles captured possibly due to the bulk flow pressure having to push against the pressure from the control channel.

Therefore, according to Figure 4.10, it seems that the only viable gates would be 4 to 8 (or 300 µm from the inlets), and this is based on their distance from the control inlet. However, there is a possibility that more gates could be built in between the locations selected for this simulation analysis. To examine this, the pressure difference between each of the channels was plotted against the y-value location of the gates, for each of the different control speeds which is shown in Figure 4.11.

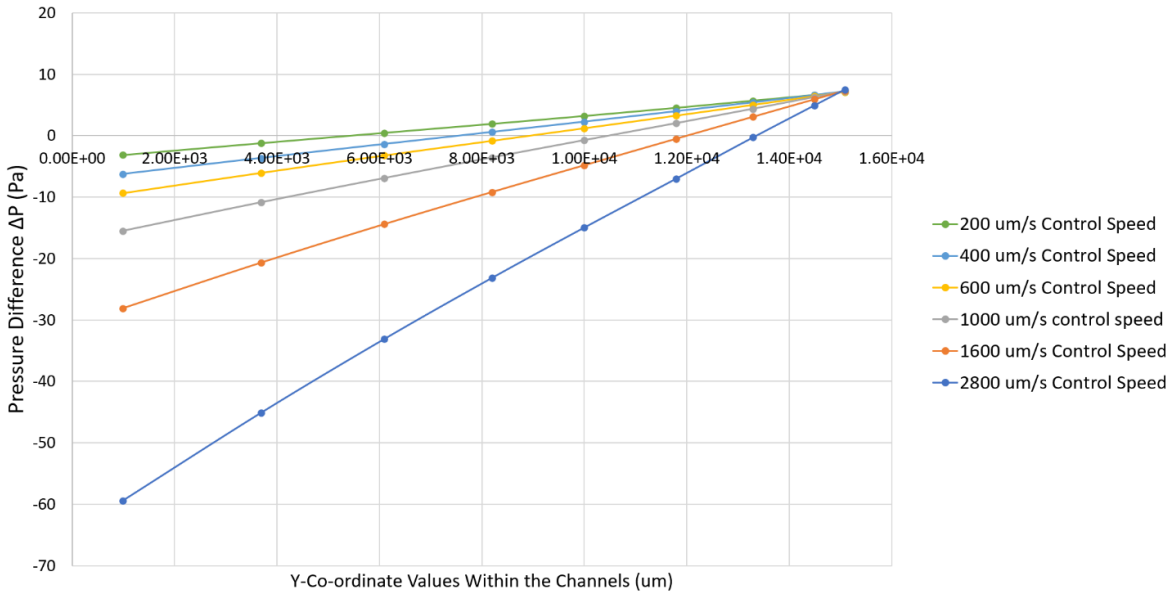

Figure 4.11: Pressure difference across the entire alternative design based on the y-coordinate position for different control speeds with 600 µm/s bulk flow speed.

Based on the data outlined in Figure 4.11, regression analysis can be plotted for each control speed to find out how the pressure difference varies along the channel as described by the following equations:

$$\boldsymbol{\Delta P = \phi(v)h - \psi(v)} \quad (4.9)$$

$$\boldsymbol{\phi(v) = 224 \cdot 83v^2 + 0 \cdot 843v + 0.0006} \ (\mathbf{R^2 = 0.99}) \quad (4.10)$$

$$\boldsymbol{\psi(v) = 3E + O6v^2 + 12160v + 1 \cdot 592} \ (\boldsymbol{R^2 = 0.99}) \quad (4.11)$$

where v is the fluid velocity of the control channel in µm/s, and h is the y-coordinate value within the channels in µm (with 0 being the control channel inlet). For the equations to hold true, the number of gates must be kept the same, the geometry of the gates must be the same (i.e., a 2 µm gap in this case) and the bulk flow equally must be the same but can be developed for other designs by further examining the pressures at different control speeds. This allows for application-specific models and redesigns for isolating objects as with this design; the gates must be closer to the centre and away from the extremes of pressure for both the control and the bulk flow channel but can be condensed as is illustrated in Figure 4.12.

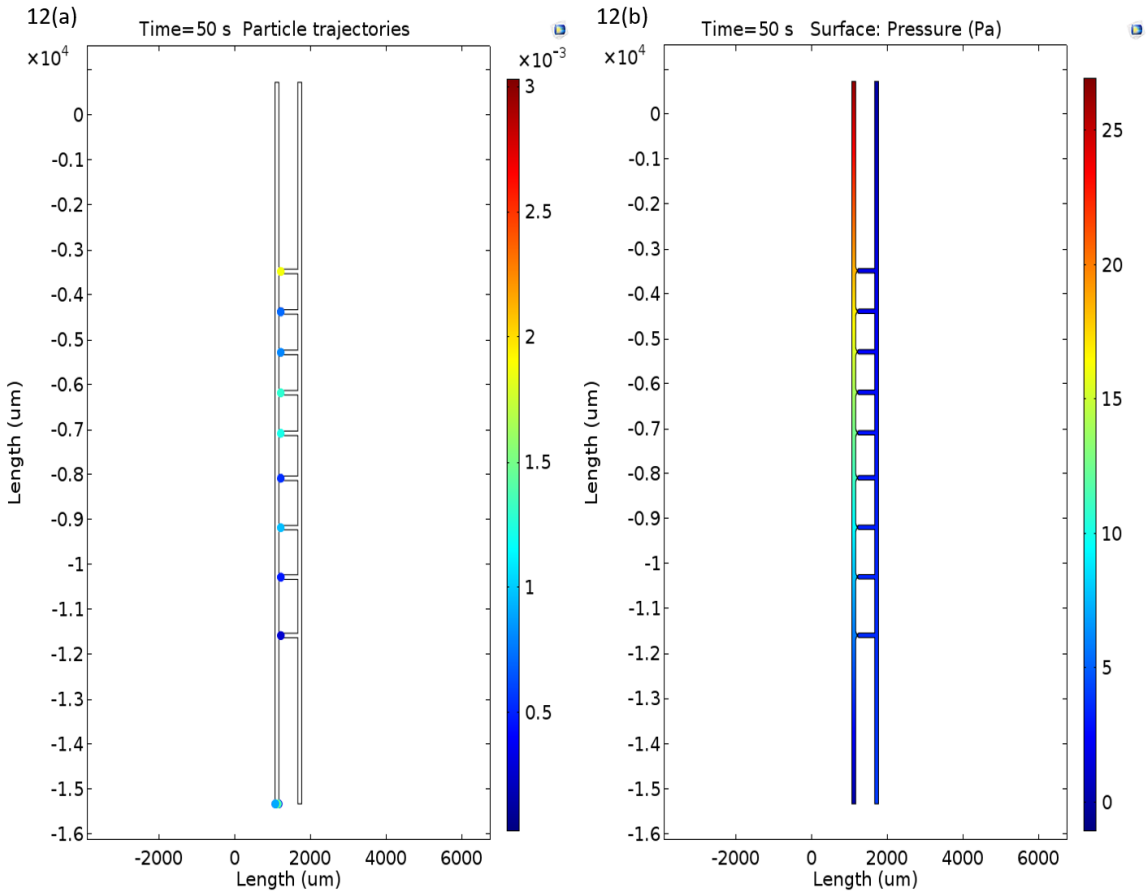

Figure 4.12: Particle trajectories and pressure of the 9-gate design. 4.12(a): Redesign of the 9-gate locations with particles all being trapped in each gate at 1600 µm/s bulk flow speed. 4.12(b): Pressure difference across the entire alternative design based on the y-coordinate position for different control speeds with 600 µm/s bulk flow speed.

The main feature of this redesign is to locate the gates closer to the centre and move any gates away from areas that could not be previously controlled by placing all gates between 4 to 8 from the previous design. This led to all gates now being able to capture objects, as well as being able to be released individually as predicted by equation 4.8. To determine

the corresponding control channel velocities from the new positions, the y-coordinates were put into equation 4.8 and a range of velocities were used, leading to a negative ΔP at each position of at least -0.5 Pa. The design was then re-simulated with these control speed values to determine the actual pressure for each gate predicted by the simulation and compared against the values predicted by the equation to determine the error at each gate for each control speed. Following this, the mean absolute error was then determined by averaging the error for each control speed to evaluate the ability of the function to predict the required control speeds for the new design as shown in Figure 4.13.

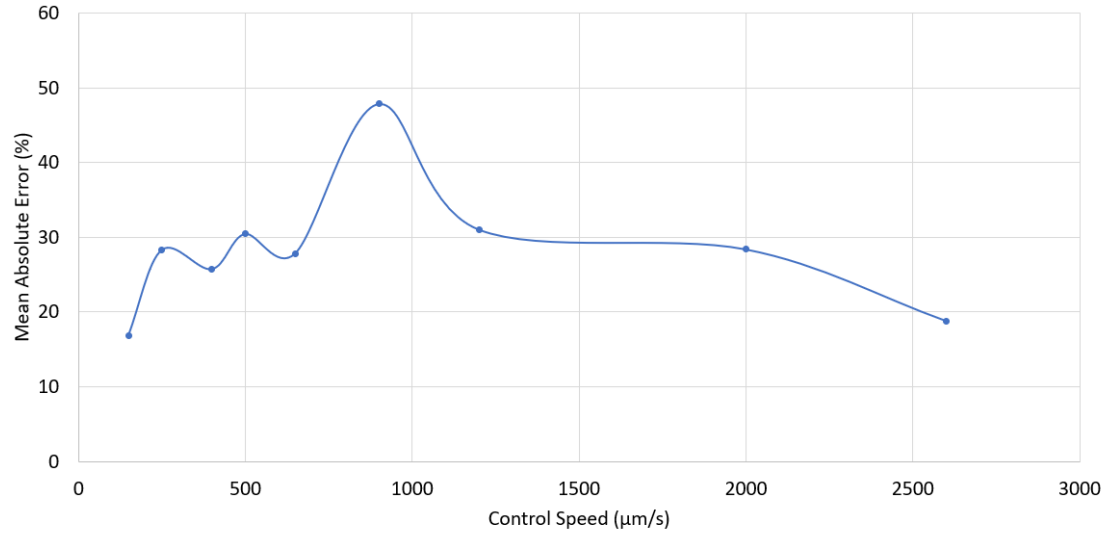

Figure 4.13: Mean absolute error of the equation predictions for the redesigned object capture structure for each of the control speeds.

As illustrated in Figure 4.13 above, the error of the equation is around 30% by magnitude apart from for the 900 µm/s control speed values. This is largely due to an error of 141% at the fourth gate resulting from pressure value approaching 0 (actual pressure -0.36 Pa, calculated pressure -0.9 Pa) leading to an anomalous magnitude of error for this particular control speed. However, for the other control speeds where the pressure magnitudes are higher, the equation predicts the pressure values between 18% and 30% even while the pressure magnitudes are still relatively small. It was also discovered that even though errors in the magnitude of the pressure were present, the sign change was accurately predicted for all values where for each control speed $'\Delta P'$ was at least negative, therefore satisfying the condition for object release from each of the gates.

4.3.3 Proof of Concept Experimentation

To demonstrate the technique, a scaled-up design was developed and tested using 100 µm microbeads as the object to be captured and released. Beads were utilised to test the trapping mechanism of the device with a micro-scale object so that laminar flow can be utilised for capture and release. Additionally, the roundness of the beads allow for checking of whether circular objects can appropriately seal square gates as is theorised.

Within these tests, 3 gates were used, for which gate number 2 is highlighted as an example of the capture and release mechanism illustrated in Figure 4.14 below. The main channel characteristic lengths were set to 300 µm and the restriction diameter was set to 150 µm to capture the beads. Two syringe pumps were used in a counter current setup as previously described, with the bulk flow rate set to 5.2 µl/min and control flow rate set to 0.6 µl/min for calculated flow speed conditions of 900 µm/s and 110 µm/s respectively for the conditions of capture of each bead.

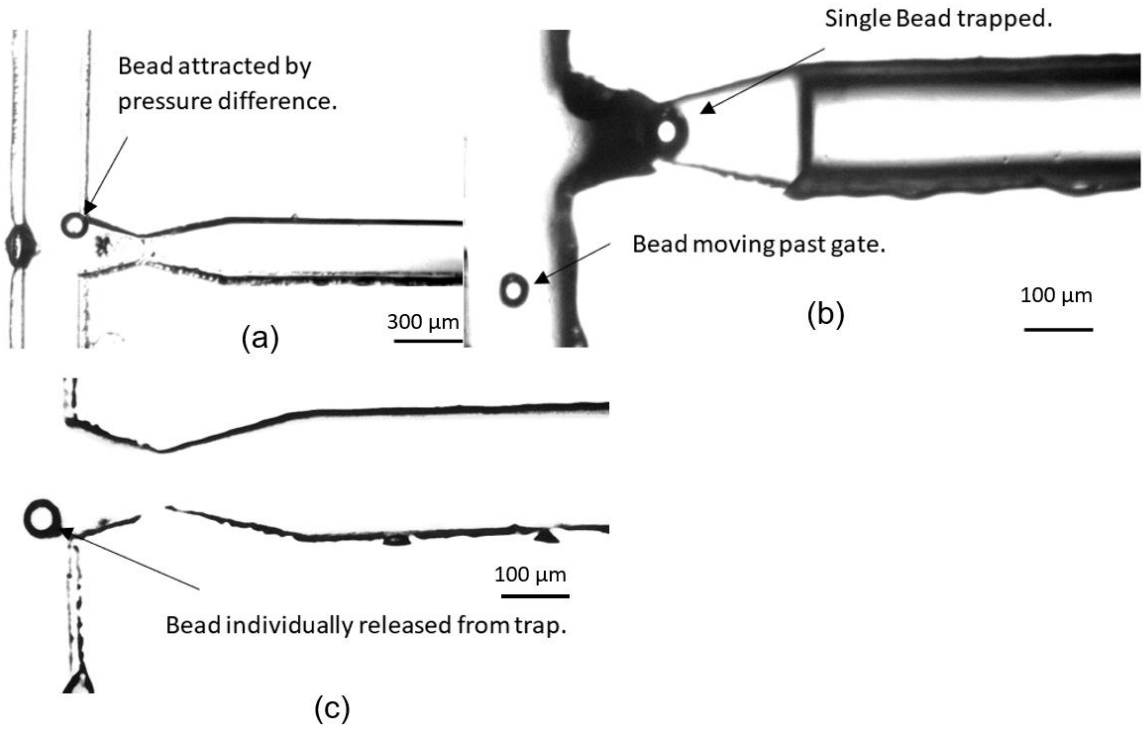

Figure 4.14: Capture release mechanism example for 150 µm beads. 4.14 (a) shows the capturing of a bead in the device. 4.14 (b) shows a single bead being trapped in the device, while any additional beads tend to move past the channel restriction. 4.14(c) shows the release of the bead from the trap.

Figure 4.14(a) demonstrates the bead moving towards the restriction in gate 2 due to the pressure difference set up from the counter current flows. It can be further observed that

as the bead approaches the gate, it is brought closer to the point where it is in the gate inlet and is then pushed into the restriction by drag. Figure 4.14(b) then shows the bead being trapped by the geometric restriction since it cannot move through the gate because of its low deformation under the low-pressure conditions (0.12 mBar calculated). Since the gate is now plugged, the flow is eliminated between each side so that additional beads flowing through the channel then move past while only a single object is held in position.

Subsequently, the inlet conditions were then altered, with the bulk flow rate now set to, and kept at 2.7 µl/min for 500 µm/s flow speed, and the control flow rate was set to 1.2 µl/min, 2.8 µl/min and 5.4 µl/min for 220 µm/s, 520 µm/s and 1000 µm/s speeds required for the release of particles in each gate. Figure 4.14(c) demonstrates the counter current flow set up allowing for the bead to be released from gate 2, at 2.8 µl/min flow rate while the bead in gate 1 was held in place, and the bead in gate 3 already released at a lower flow rate.

Although the design was able to capture and isolate individual beads, a better design would have included a smaller restriction of a much lower diameter than that of the object of interest. This is due to the shape of the channels resulting from the laser ablation manufacturing method not allowing the beads to create a strong enough seal. Consequently, some pairs of beads that were captured in each gate, were allowed to be washed away with continuous flow in the bulk flow channel. It was also found that the trend of requiring exponentially higher fluid speeds for objects close to the bulk flow inlet (gate 1) was seen in effect with this design also, indeed due to the relatively large gate diameter.

In the end, even in a larger design, the counter current flow design has been successfully demonstrated and is in agreement with the principles set up by the simulation for individual object capture and release within a microfluidic environment. Consequently, further exploration can be undertaken regarding smaller-scale objects to further validate the simulation models, as well as in relation to gate design optimisation for a more consistent individual capturing method.

Further exploration should also be given to examining cells and particularly sperm cells as the final target goal. Beads only follow the path of the fluid due to the drag force exerted

on them, however, sperm has it's own driving force from their flagellar motion. If the fluid speed is too low, the sperm will not be trapped as the pressure difference between each side is too small and if the fluid speed is in the rheotaxis zone then they may turn against the flow and not move as predicted by the beads. There is therefore a lower limit that must be found to make this method applicable to sperm which is sufficient to overcome the sperm's own velocity (approximately 90 μm/s) where their movement is dictated by fluid drag rather than their own movement [123][124]. Another consideration is the rigidness of beads when compared to sperm, as well as sperm having an upper limit of the pressure they can be subjected to before deformation and cell death occurs. There is little information regarding what pressures can lead to cell death or unviability for injection particularly for local deformation, however, sperm are routinely subjected to hundreds of g-force for sorting purposes during current ICSI procedures (approximately 64 μN) [8]. As an estimate, the maximum pressure a sperm can be subjected to is approximately 23 mbar to be below this limit assuming the that the entire sperm head is in contact with the wall (3x3 μm^2). Therefore, considerations should be also given for the design that reduce the forces and therefore pressures to below this threshold on the sperm head by eliminating sharp edges that can induce local deformation.

The final consideration is for manufacture of the device with medical materials as PDMS cannot be used in clinical settings. It was used in this research due to being easy to develop a master for and then cheap to manufacture multiple devices to demonstrate the capture mechanism of the device. Typically, medical device materials are required to be biocompatible and have resistance to chemical attack while maintaining their safety and functionality [125]. One method could be through a two-stage etching process as this will allow the required dimensions to be reached while maintaining different sizes for channels (eg. with SU-8) where the gates are etched first to the required dimensions and then the main channels after although this loses any potential of 3D geometries within the design and would need to be examined for cytotoxicity. Other potential options could be through injection moulding of PMMA or hot embossing after generating a master mould where the replication technique would need to be developed to ensure the dimensions are suitable for sperm capture.

4.4 Conclusion

A novel method for isolation and release of individual objects has been successfully demonstrated throughout this chapter. This method offers a new microfluidic method for researchers to isolate single objects for analysis or further interactions within a microfluidic device. Simulation has demonstrated the principle of the counter current setup and therefore offers theoretical methods of determining flow requirements for different designs, sizes, and amounts of objects captured. The method has additionally been experimentally validated using 150 µm diameter microbeads and has demonstrated the ability for individual object isolation and release. There is also potential, due to the laminar nature of microfluidics, to automate the flow-rate-switching process and increase the number of objects isolated simultaneously by increasing the number of gates.

5. Microfluidic Control and Theory for Individual cell Capture

5.1 Introduction

Managing the fluid within the microfluidic device is critical to manipulating any cells or objects of interest. In the present design, determining the direction of the flow within the gate channels is of high importance since these dictates whether a cell is attracted into the restriction or not. The fluid control also defines when each cell is released from each gate by determining at what input pressures the fluid reverses. In this chapter, the theory of fluid control is found for the device, a set of simultaneous equations are developed to describe this particular setup for fluid flow, and a theoretical model to calculate the fluid flows in the gate channels is established. The model is then evaluated against experimental values to validate its effectiveness at predicting the required pressure control scheme.

5.2 Theory and Microfluidic Circuit Analysis

It has been extensively demonstrated that adopting an electrical point of view can be used to analyse a microfluidic circuit due to the laminar flow condition. As such, there should be a linear reduction in pressure from inlet to outlet ΔP where the inlet condition is defined by the fluid pressure source, and the outlet condition can be considered as atmospheric (particularly because of the immediate length scale change once leaving the microfluidic system). Between the inlet/outlet, the channel lengths can be considered as 'resistors' which can be determined when considering the simplified Hagen-Poiseuille law:

$$Q = \frac{\Delta P}{R_H} \quad (5.1)$$

Where Q is the flow rate, ΔP is the pressure difference across a channel and R_H is equivalent hydraulic resistance across the channel. For circular channels R_H is simply:

$$R_H = \frac{8\mu L}{\pi R^4} \quad (5.2)$$

Where μ is the dynamic viscosity, L is the channel length and R is the channel radius. For rectangular microchannels, R_H can be calculated as the summation of a Fourier series:

$$R_H = \frac{12\mu L}{wh^3\left(1 - \frac{h}{w}\left(\frac{192}{\pi^5}\sum_{n=1,3,5}^{\infty}\frac{1}{n^5}tanh\left(\frac{n\pi w}{2h}\right)\right)\right)} \quad (5.3)$$

Where w is the channel width, h is the channel height, or as a simplification:

$$R_H = f(h,w)\eta L;\ \ R_H \propto L \quad (5.4)$$

Where it can be observed that the hydraulic resistance is proportional to the channel length as μ is a constant when assuming constant temperature for the flow, and $f(h,w)$ is geometrically constrained by the channel size. As most channels are of the same diameter within microfluidics, $f(h,w)$ is effectively a constant, except in this design for the gate restriction and the channel connecting the left and right channel. A similar analogy can be found for Kirchoff's current law for fluidic circuits where the sum of flows entering a node is equal to the sum of flow leaving the node (as mass conservation) or:

$$\sum_{n=1}^{N} Q_n = 0 \quad (5.5)$$

Where the n subscript denotes different expected flows at junctions or after resistances. A circuit schematic of the design is displayed in Figure 5.1 below.

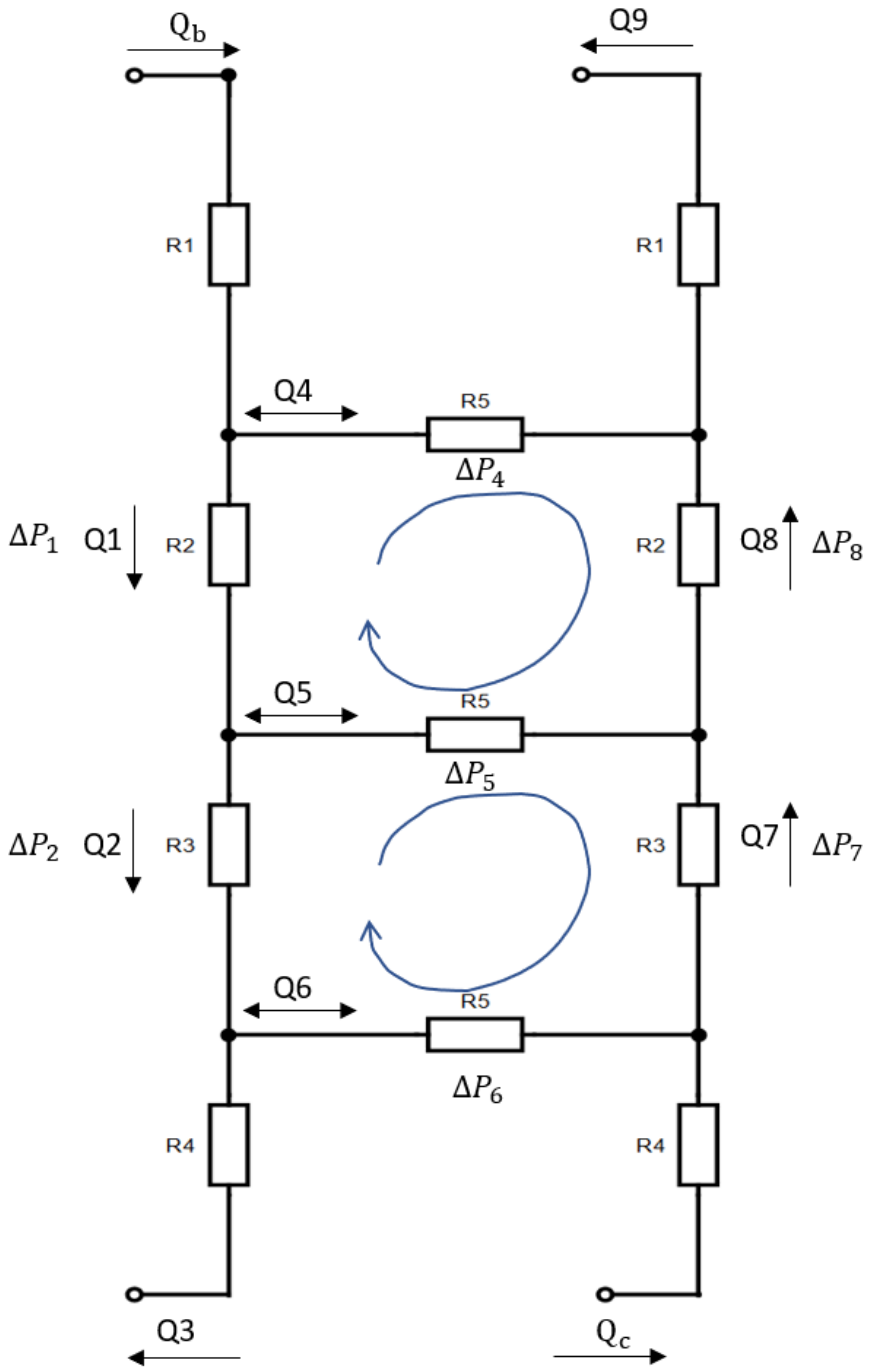

Figure 5.1: An electrical circuit schematic of the microfluidic design. Q_b denotes the inlet bulk flow rate and Q_c denotes the inlet control flow rate. R is the equivalent hydraulic fluid resistance for the channel, ΔP is the pressure drop across the channel and Q_n are the unknown flow rates to be determined.

Due to the symmetry of the design, fluid resistors parallel to each other can be considered to have the same vale; for instance, R_1, left is the same as R_1, right and so on. Utilising equation 5.4, a set of simultaneous equations can be developed to describe the system; however, the initial configuration and the direction of the flow needs to be considered. As such, 4 device states are described: the capture state where $Q_b \gg Q_c$, the third gate

release state where $Q_b > Q_c$ and Q6 is in the direction of the bulk flow channel, the second gate release state where $Q_b < Q_c$ but Q_c is larger and $Q_{5,6}$ are in the direction of the bulk flow channel, and the first gate release state where $Q_b \gg Q_c$ and $Q_{4,5,6}$ are in the direction of the bulk flow channel for which the equations are shown in Table 5.1 below.

Table 5.1: Simultaneous equations for the dependencies of each flow rate based on a Kirchoff's current law analogy for fluids.

Device State 1: Capture ($Q_b \gg Q_c$)	Device State 2: Third Gate Release ($Q_b > Q_c$)	Device State 3: Second Gate Release ($Q_b < Q_c$)	Device State 4: First Gate Release ($Q_b \ll Q_c$)
$Q_1 = Q_b - Q_4$	$Q_1 = Q_b - Q_4$	$Q_1 = Q_b - Q_4$	$Q_1 = Q_b + Q_4$
$Q_2 = Q_1 - Q_5$	$Q_2 = Q_1 - Q_5$	$Q_2 = Q_1 + Q_5$	$Q_2 = Q_1 + Q_5$
$Q_3 = Q_2 - Q_6$	$Q_3 = Q_2 + Q_6$	$Q_3 = Q_2 + Q_6$	$Q_3 = Q_2 + Q_6$
$Q_7 = Q_c + Q_6$	$Q_7 = Q_c - Q_6$	$Q_7 = Q_c - Q_6$	$Q_7 = Q_c - Q_6$
$Q_8 = Q_7 + Q_5$	$Q_8 = Q_7 + Q_5$	$Q_8 = Q_7 - Q_5$	$Q_8 = Q_7 - Q_5$
$Q_9 = Q_8 + Q_4$	$Q_9 = Q_8 + Q_4$	$Q_9 = Q_8 + Q_4$	$Q_9 = Q_8 - Q_4$

From Table 5.1, it can be observed that a general description of the device flow rates could be developed by allowing for each arithmetic symbol to be denoted as '±', where the sign depends on the direction of the fluid flow (and consideration of what is set as positive and negative). As a first assumption, Q_b and Q_c are both known values as inlet conditions for the device.

As a practical consideration, it is useful to determine the specific flow rates at each gate, as functions of Q_b and Q_c, in order to determine theoretical pressure requirements at each fluid inlet for experiments, for which the corresponding flow rates are Q_4 (Gate 1), Q_5 (Gate 2), Q_6 (Gate 3). Rearranging the simultaneous equations for each device in terms of these flow rates gives the following set of equations for the flow rate at each gate for every device state:

$$\left.\begin{array}{c} Q_4 = [Q_b + Q_c] - Q_3 - Q_8 \\ Q_5 = -[Q_b + Q_c] + Q_1 + Q_3 + Q_9 - Q_2 \\ Q_6 = -[Q_b + Q_c] + Q_2 + Q_9 \end{array}\right\} Q_b \gg Q_c \quad (5.6)$$

$$\left.\begin{array}{c} Q_4 = [Q_b + Q_c] - Q_3 - Q_8 \\ Q_5 = -[Q_b + Q_c] + Q_1 + Q_3 + Q_9 - Q_2 \\ Q_6 = [Q_b + Q_c] - Q_2 - Q_9 \end{array}\right\} Q_b > Q_c \quad (5.7)$$

$$\left.\begin{array}{c} Q_4 = [Q_b + Q_c] - Q_3 - Q_8 \\ Q_5 = [Q_b + Q_c] - Q_1 - Q_3 - Q_9 + Q_2 \\ Q_6 = [Q_b + Q_c] - Q_2 - Q_9 \end{array}\right\} Q_b \leq Q_c \quad (5.8)$$

$$\left.\begin{array}{c} Q_4 = -[Q_b + Q_c] + Q_3 + Q_8 \\ Q_5 = [Q_b + Q_c] - Q_1 - Q_3 - Q_9 + Q_2 \\ Q_6 = [Q_b + Q_c] - Q_2 - Q_9 \end{array}\right\} Q_b \ll Q_c \quad (5.9)$$

$$\left.\begin{array}{c} Q_4 = \pm[Q_b + Q_c] \pm Q_3 \pm Q_8 \\ Q_5 = \pm[Q_b + Q_c] \pm Q_1 \pm Q_3 \pm Q_9 \pm Q_2 \\ Q_6 = \pm[Q_b + Q_c] \pm Q_2 \pm Q_9 \end{array}\right\} \quad (5.10)$$

Equations 5.6 through 5.9 describe the flow rate conditions for each of the gates depending on the channel configuration, while equation 5.10 is the general form of the equations for the device description. The summary of each of the gate flow conditions is determined by the gate condition where, when the gate direction is reversed, the associated equation for each gate is multiplied by -1. Interestingly, however, the inlet flow rates only act as a sum for each flow rate (as their sign is always the same), and other flows within the channel determine the direction. For example, for Q_4 to be true in equation 5.5, $Q_b + Q_c > Q_3 + Q_8$, otherwise the flow becomes negative and goes against the initial assumptions for the equation setup (i.e., $Q_1 \neq Q_b - Q_4$) if this were to happen. To evaluate and explain each equation, each system can be rearranged so that the bulk and control channel flow rates are shown together (as denoted by the square brackets) where using the capture state of the device we have:

$$\left.\begin{array}{c} Q_4 = [Q_b - Q_3] + [Q_c - Q_8] \\ Q_5 = [Q_1 + Q_3 - Q_b - Q_2] + [Q_9 - Q_c] \\ Q_6 = [Q_2 - Q_b] + [Q_9 - Q_c] \end{array}\right\} Q_b \gg Q_c \quad (5.11)$$

From this system, it can be established that for each of the flow rates, a set of equalities can be developed to ensure they are positive and moving in the expected directions.

$$\left.\begin{array}{c} Q_b + Q_c > Q_3 + Q_8\} Q_4 > 0 \\ Q_1 + Q_3 + Q_9 > Q_b + Q_c + Q_2\} Q_{\ 5} > 0 \\ Q_2 + Q_9 > Q_b + Q_c\} Q_6 > 0 \end{array}\right\} Q_b \gg Q_c \ (5.12)$$

Then, for any release of particles, the inequalities change direction as the flow rate would be negative compared to the initial setup of the equations. To determine additional relations within these equations for flow rate, a similar analogy to Kirchoff's voltage law can be used, where the sum of pressure drop around a closed path in the circuit is 0:

$$\sum_{n=1}^{N} P_n = 0 \ (5.13)$$

By considering the direction of the flow again for each device state and solving the loops shown in Figure 5.1, we obtain:

$$\left.\begin{array}{l} R_2(Q_1 + Q_8) + R_5(-Q_4 + Q_5) = 0 \\ R_3(Q_2 + Q_7) + R_5(-Q_5 + Q_6) = 0 \end{array}\right\} Q_b \gg Q_c \ (5.14)$$

$$\left.\begin{array}{l} R_2(Q_1 + Q_8) + R_5(-Q_4 + Q_5) = 0 \\ R_3(Q_2 + Q_7) - R_5(Q_5 + Q_6) = 0 \end{array}\right\} Q_b > Q_c \ (5.15)$$

$$\left.\begin{array}{l} R_2(Q_1 + Q_8) - R_5(Q_4 + Q_5) = 0 \\ R_3(Q_2 + Q_7) + R_5(Q_5 - Q_6) = 0 \end{array}\right\} Q_b \leq Q_c \ (5.16)$$

$$\left.\begin{array}{l} R_2(Q_1 + Q_8) + (Q_4 - Q_5) = 0 \\ R_3(Q_2 + Q_7) + (Q_5 - Q_6) = 0 \end{array}\right\} Q_b \ll Q_c \ (5.17)$$

Finally, by considering the two lines from inlets to outlets on the same side, and utilising equation 5.1, a final set of equations can be developed to solve for the flow in the system. To use this, points of the pressures are considered in the system for equivalences, as illustrated in Figure 5.2 below.

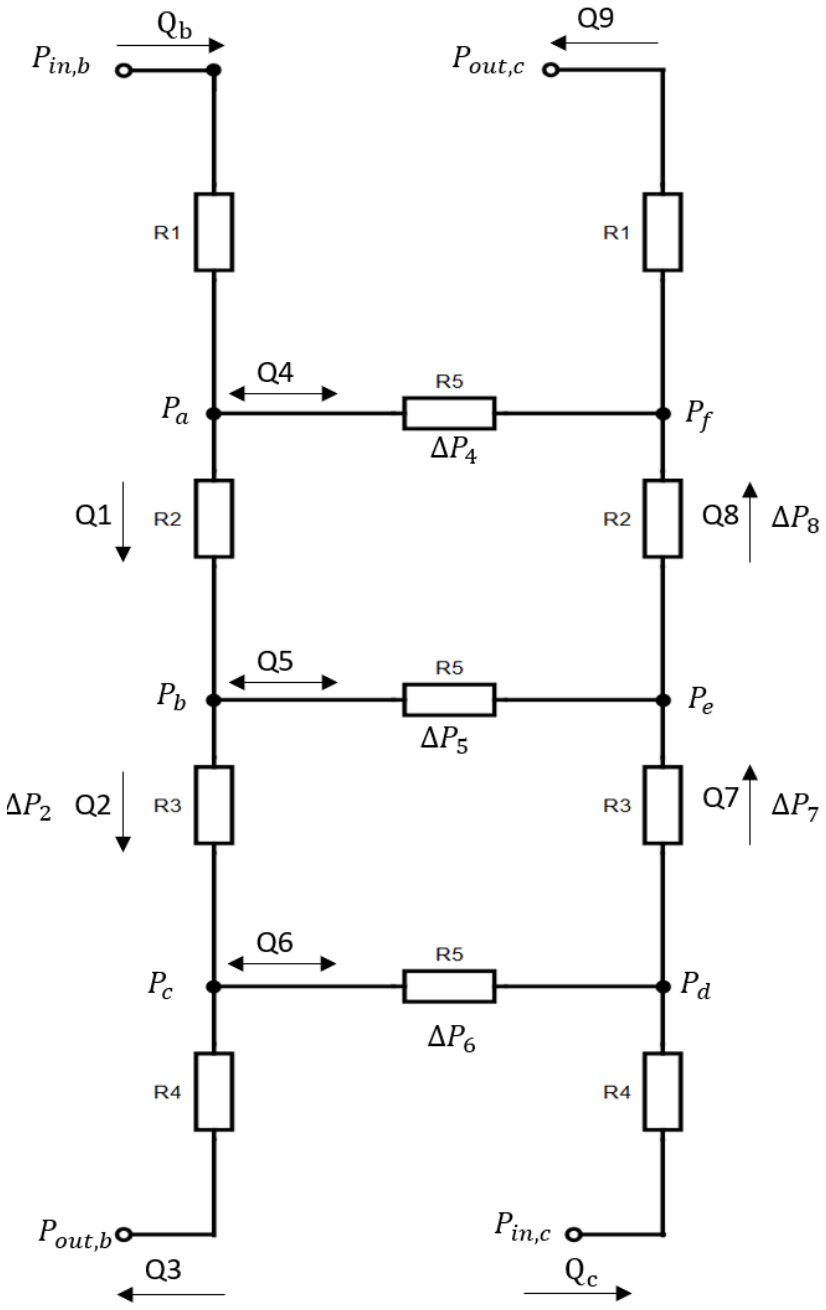

Figure 5.2: An electrical circuit schematic of the microfluidic design. P_n is representative of the pressures at each node.

Based on Figure 5.2, a few assumptions are made where the outlet conditions $P_{out,b/c}$ are considered 0 for this analysis but can also be a known constant for applications. Next, $P_{in,b/c}$ are also known as inlet conditions and have a relationship to $Q_{b/c}$ denoted by equation 5.1. From this, we can obtain the final equations by systematically running along each main channel (e.g. with the control channel, $\Delta P_9 = \Delta P_f - \Delta P_{out,c}$, $\Delta P_8 = \Delta P_e -$

ΔP_f, …, $\Delta P_c = \Delta P_{in,c} - \Delta P_d$) and equating the flow rates between each gate channel: $\Delta P_5 = \Delta P_b$ -ΔP_e From this setup, the following equations are obtained:

$$\left.\begin{aligned} P_{in,b} - R_1 Q_b - P_{in,c} + R_4 Q_c &= R_5 Q_4 - R_3 Q_7 - R_2 Q_8 \\ P_{in,b} - R_1 Q_b - P_{in,c} + R_4 Q_c &= R_2 Q_1 + R_5 Q_5 - R_3 Q_7 \\ P_{in,b} - R_1 Q_b - P_{in,c} + R_4 Q_c &= R_2 Q_1 + R_3 Q_2 + R_5 Q_6 \end{aligned}\right\} Q_b \gg Q_c \quad (5.18)$$

$$\left.\begin{aligned} P_{in,b} - R_1 Q_b - P_{in,c} + R_4 Q_c &= R_5 Q_4 - R_3 Q_7 - R_2 Q_8 \\ P_{in,b} - R_1 Q_b - P_{in,c} + R_4 Q_c &= R_2 Q_1 + R_5 Q_5 - R_3 Q_7 \\ -P_{in,b} + R_1 Q_b + P_{in,c} - R_4 Q_c &= -R_2 Q_1 - R_3 Q_2 + R_5 Q_6 \end{aligned}\right\} Q_b > Q_c \quad (5.19)$$

$$\left.\begin{aligned} P_{in,b} - R_1 Q_b - P_{in,c} + R_4 Q_c &= R_5 Q_4 - R_3 Q_7 - R_2 Q_8 \\ -P_{in,b} + R_1 Q_b + P_{in,c} - R_4 Q_c &= -R_2 Q_1 + R_5 Q_5 + R_3 Q_7 \\ -P_{in,b} + R_1 Q_b + P_{in,c} - R_4 Q_c &= -R_2 Q_1 - R_3 Q_2 + R_5 Q_6 \end{aligned}\right\} Q_b < Q_c \quad (5.20)$$

$$\left.\begin{aligned} -P_{in,b} + R_1 Q_b + P_{in,c} - R_4 Q_c &= R_5 Q_4 + R_3 Q_7 + R_2 Q_8 \\ -P_{in,b} + R_1 Q_b + P_{in,c} - R_4 Q_c &= -R_2 Q_1 + R_5 Q_5 + R_3 Q_7 \\ -P_{in,b} + R_1 Q_b + P_{in,c} - R_4 Q_c &= -R_2 Q_1 - R_3 Q_2 + R_5 Q_6 \end{aligned}\right\} Q_b \ll Q_c \quad (5.21)$$

This set of equations define the direction of the flow rate between each of the channels as they are simply the pressure difference between each side of the channel, with the magnitude of the flow rates determined by the Q_n parameters. A similar sign switch occurs on the switch from each of the device states with all values being multiplied by -1, apart from the flow rates of interest $Q_{4,5,6}$.

Consequently, the system can now be solved for all flow rates with dependency on $P_{in,b/c}$ experimentally by evaluating the fluid velocity at a given pressure in the external piping using 1 dimensional velocimetry techniques and finding $Q_{external}$. Following this, the Reynold's number is firstly to be determined:

$$Re = \frac{\rho u D}{\mu} \quad (5.22)$$

Typically for a 0.794 mm (1/32") internal pipe, the fluid regime can be considered laminar (50 mm/s flow rate corresponds to a Reynold's number of 44.47, well below the transition range of approximately 1800). As a result, equation 5.1 still applies to the external piping, so by determining the relationship between controller pressure and flow rate, the pressure into the microfluidic chip can be determined from:

$$P_{in,c/b} = P_{controller} - Q_{external}R_{external} \ (5.23)$$

Where the external resistance can be derived from equation 5.2 and the flow rates can be determined using conservation of mass assuming the density is constant due to incompressible flow:

$$Q_{external} = Q_{b,c} \ (5.24)$$

The equations can then be solved using Gauss-Jordan elimination by forming an augmented matrix for each of the device states, where each device state can be put into the form:

$$A * x = B \ (5.25)$$

Where A is a coefficient matrix depending on the analysis resulting from equations 4.1, 5.4 and 5.12, x is always a vector containing $Q_{1,2,4,5,6,7,8}$ and B is a vector made up of the input values Q_b, Q_c and $P_{in,c}$. $Q_{3,9}$ can be determined by substituting the values for $Q_{2,4,6,8}$ based on the equations outlined in Table 5.1. An example matrix is given as:

$$\begin{pmatrix} 1 & 0 & \pm 1 & 0 & 0 & 0 & 0 \\ -1 & 1 & 0 & \pm 1 & 0 & 0 & 0 \\ 0 & 0 & 0 & 0 & \pm 1 & 1 & 0 \\ 0 & 0 & 0 & \pm 1 & 0 & 1 & -1 \\ R_2 & 0 & \pm R_5 & \pm R_5 & 0 & 0 & R_2 \\ 0 & R_3 & 0 & \pm R_5 & \pm R_5 & R_3 & 0 \\ 0 & 0 & R_5 & 0 & 0 & \pm R_3 & \pm R_2 \\ \pm R_2 & 0 & 0 & R_5 & 0 & \pm R_3 & 0 \\ \pm R_2 & \pm R_3 & 0 & 0 & R_5 & 0 & 0 \end{pmatrix} \begin{pmatrix} Q_1 \\ Q_2 \\ Q_4 \\ Q_5 \\ Q_6 \\ Q_7 \\ Q_8 \end{pmatrix} = \begin{pmatrix} Q_b \\ 0 \\ Q_c \\ 0 \\ 0 \\ 0 \\ P_{in,c} - Q_C R_4 \\ P_{in,b} - R_1 Q_b - P_{in,c} + R_4 Q_b \\ P_{in,b} - R_1 Q_b - P_{in,c} + R_4 Q_b \\ P_{in,b} - R_1 Q_b - P_{in,c} + R_4 Q_b \end{pmatrix} \ (5.26)$$

With the ± indicating whether a sign change is required depending on the device state. Additionally, two extra rows are included from the pressure analysis to further constrict the results and correctly define the direction of the flow through the gate channels. During the row-reduction, the bottom two rows in the augmented matrix are aimed to become a row of zeroes, while the top 7 rows correspond to the Q_n vector. Due to the nature of the equations, if a negative value is found based on the original setup, this simply means that the flow is moving in the opposite direction than what was originally defined. Moreover, it should be noted that when an object is trapped inside any of the gates, the resistance

becomes infinite, so during the capture mechanism as shown in chapter 4, once an object is held in place, $R_5 = \infty$. This means that flow is effectively eliminated between each side; however, the pressure difference is still at play where if the flow direction switches, the resistance moves back from ∞ to R_5 on object release. This highlights why objects move past the gate restrictions once an object has been trapped in place [126].

5.3 Materials and Methods

To determine the flow rates from equation 5.25, a Matlab (MATLAB 2017b, The MathWorks, Natick, 2017) script was developed to perform the Gaussian-Jordan elimination (further detail in the Appendix).

Subsequently, a device was made through directly micro milling a piece of PMMA as illustrated in Figure 5.3 below.

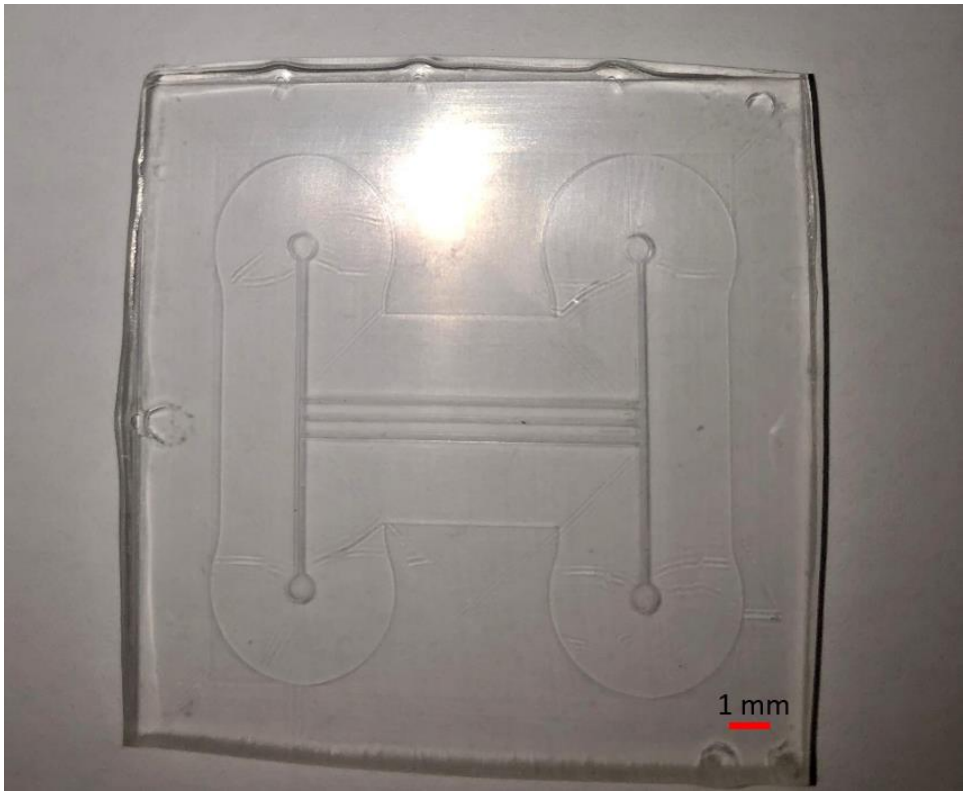

Figure 5.3: Micro milled PMMA microfluidic device. Average channel width and height is 300 µm, gate restriction dimensions are 30 µm x 10 µm.

The device shown in Figure 5.3 was further altered by drilling through each of the inlet holes to create fittings for the external piping. Piping was attached at each inlet and sealed

as a permanent fixture using epoxy resin as well as to hold the piping in place. The open channel side was sealed by using transparent nano adhesive tape (KONAMO). This setup was tested for leakage and no significant leakage was found up to pressures of 700 mbar at each inlet.

The velocimetric used was by timing a dyed fluid moving from the reservoir to a marker on the channel close to the chip. Initially, the external piping and chip were filled with clear water. Once filled, the reservoir for the inlet was changed to contain water mixed with a typical red food colouring (NATCO FOODS LTD.). Once the dye had been identified as leaving the reservoir, the timer started and then stopped when it reached the marker at the inlet of the device.

Two fluid reservoirs were used for testing, and both were filled with de-ionised water. One reservoir had 5 ml of food dye added per 15 ml of water for the velocimetric techniques as well as monitoring the fluid conditions within the device. Fluid was pressure-controlled using an OB1 MK3+ pressure controller (Elveflow) with +/- 1 bar outlets and the pressure set and monitored using the compatible Elveflow Smart Interface software.

The internals of the device were monitored by attaching the other side of the adhesive tape to a petri dish and placed under a BestScope BS-2090 inverted microscope equipped with a 0.45x Basler 106752 camera recording at 200 frames per second. All images were captured using a 4X objective lens, with a 10X internal microscope magnification resulting in an overall image magnification of 40X.

5.4 Results and Discussion

Initially, velocimetry was performed to establish the inlet conditions of the microfluidic device for both inlets, as displayed in Figure 5.4.

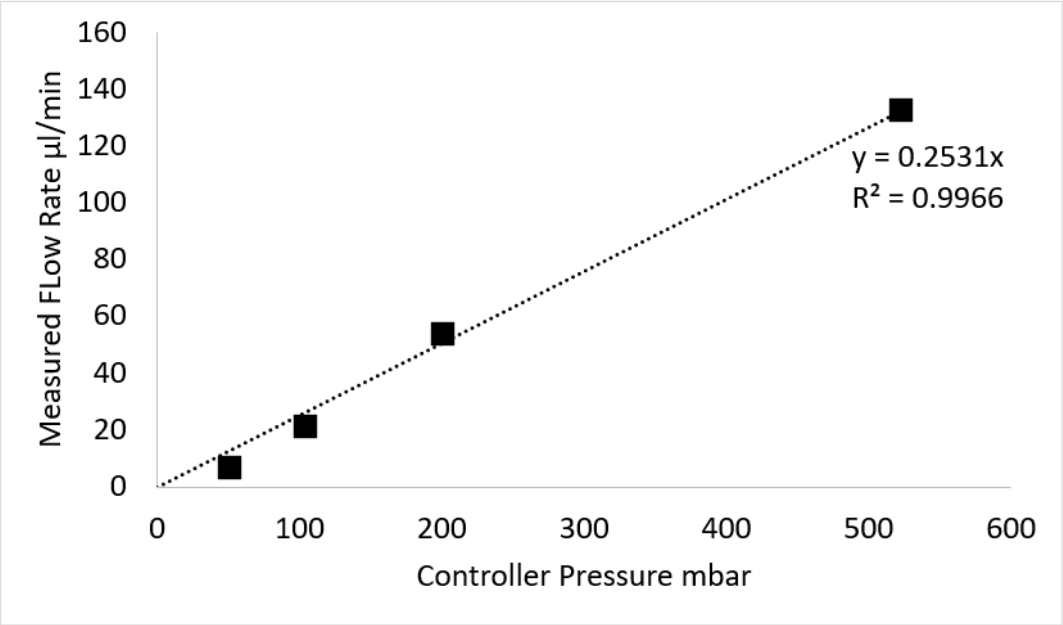

Figure 5.4: Measured velocities versus control pressure applied to the device across a length of 65cm for a pipe with an internal diameter of 0.794 mm, with an additional fluid resistance pipe of 10 cm with 100 µm internal diameter.

Figure 5.4 demonstrates that the relationship between flow rate and controller pressure follows a linear pattern as is expected from the relationship between Q and ΔP. Therefore, using the values from Figure 5.3, the pressure drop across the channels from the controller to each microfluidic inlet can be calculated and utilised to give a reference point for how the system is behaving using equations 5.22 and 5.23. Using the relation between the controller input pressure and the flow rate, the equations are then solved by providing their input values, allowing equation 5.26 to then be solved based on controller pressures. A ratio can then be determined as P_{bcont}/P_{ccont} for each of the controller pressures to find out what the difference between them needs to be in order to alter the flow direction, as shown in Figure 5.5.

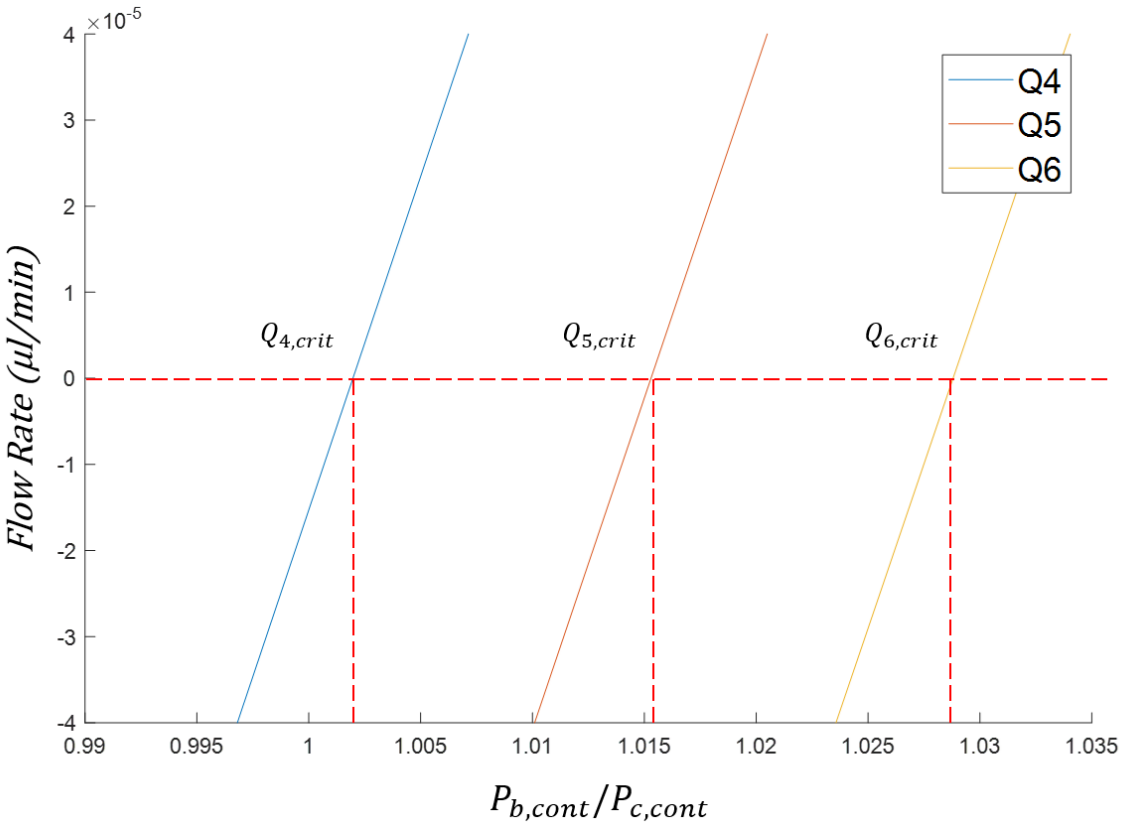

Figure 5.5: Critical points for $Q_{4,5,6}$ where the intersection of the dotted lines indicates where the flow rates are equal to 0 for $P_{c,cont}$ = 100 mbar.

Indeed, Figure 5.5 above provides the analytical solution for what the required pressures are to switch the direction of the flow rates. The order illustrated is as expected, with Q_4 requiring a lower ratio of $P_{b,cont}/P_{c,cont}$ than Q_5, and with Q_5 being lower than Q_6 due to the proximity of the channels to their respective inlets. The proximity of the values to 1 is also what would be expected due to the design being almost symmetric where, for the design analysed, R_2 = R_3 and R_1 is only slightly larger than Q_5 as it is approximately 2 mm longer. The result of this length difference is indicated by the difference in intervals between each of the critical Q values where, if it were symmetric, $Q_{5,crit}$ would be precisely on $P_{b,cont}/P_{c,cont}$ = 0, in this scenario however all of the critical values are shifted to the right somewhat. It is estimated that the only important values for determining the flow rate direction are the ratios between the controller pressure inputs, where the magnitude only determines flow rates through the device.

The magnitude of the interval size depends on the distance between each channel, which was 1 mm for the present setup, thus explaining why the required pressure difference is still relatively small between each critical value despite the addition of a flow restrictor to the inlet flow rate. $Q_{5,crit} - Q_{4,crit}$ from Figure 5.4 is $P_{b,cont}$ = 1.3 mbar and then $Q_{6,crit} - Q_{5,crit}$ is $\Delta P_{b,cont}$ = 1.4 mbar, meaning that fairly precise control of pressure around 0.5 mbar is required to allow for the device to be held in each state. To allow for better control of each gate, the distance between each gate could be increased. This would further allow for a less precise control scheme to still achieve the goal of each flow rate manipulation. An example of this is exhibited in Figure 5.6 below:

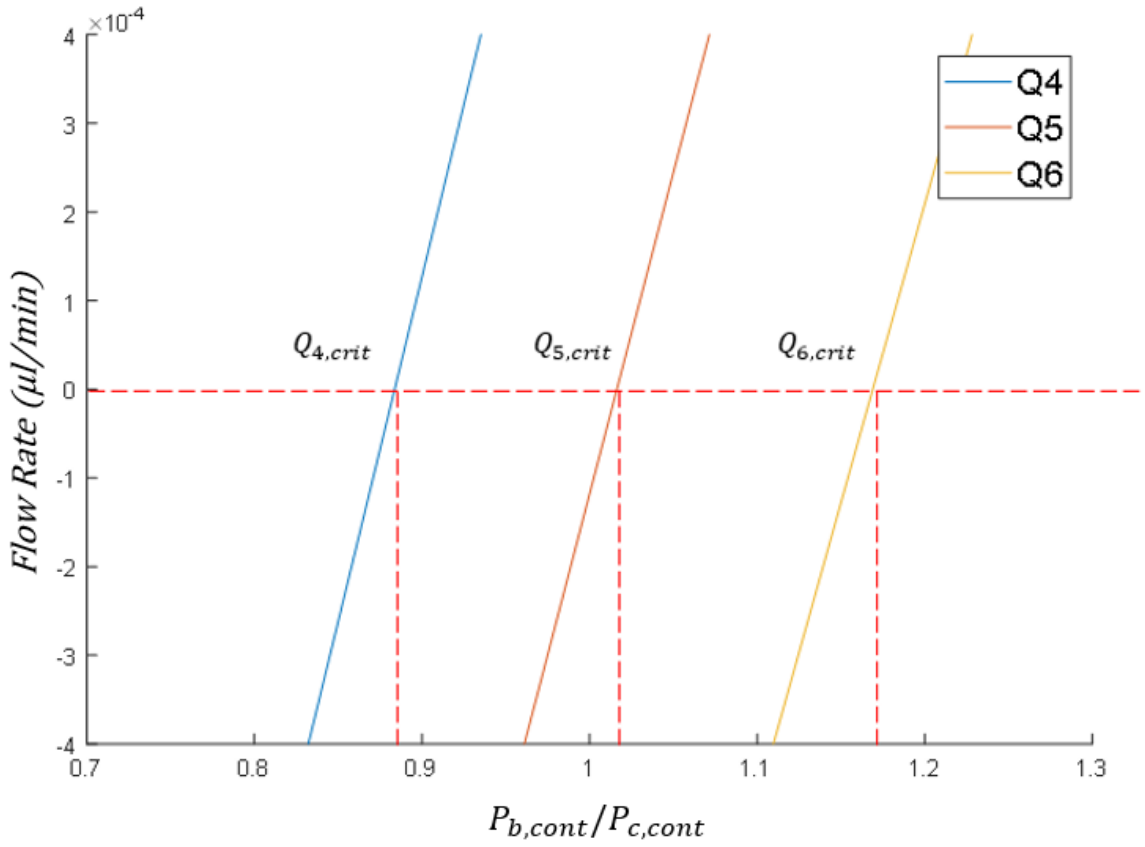

Figure 5.6: The critical points for $Q_{4,5,6}$ for a potential redesign of the tested device with distances between each gate increased to 10 mm. where the intersection of the dotted lines indicates where the flow rates are equal to 0 for $P_{c,cont}$ = 100 mbar.

Figure 5.6 highlights the difference between each critical flow rate, which is much more pronounced as seen by the significant reduction in the rate of change of the flow rates. $Q_{5,crit} - Q_{4,crit}$ is now at $\Delta P_{b,cont}$ = 13 mbar and $Q_{6,crit} - Q_{5,crit}$ becomes $\Delta P_{b,cont}$ = 14 mbar, giving just over 10 times the difference required for the critical flow rates to be reached for the control of the gates leading to less of a need for such precise control over

flow rates. Even though the rate of the flow rates is increasing, each line is diverging faster from one another compared to the 1 mm setup as can be seen with Q_6 now being separated further from the other critical values. However, this information needs to be interpreted alongside the findings of the previous analysis of the simulation setup in outlined throughout Chapter 4. If the gates are too close to their respective inlets, and for example, an object is required to be released from the first gate, the bulk pressure will be too high, and it will be very difficult for the control pressure to reach sufficiently high values to release the object from the gate. This is confirmed by seeing, for example with Q_4, that the critical ratio is now much lower at a ratio of approximately 0.84. If the distance to the bulk flow inlet was reduced as well ($R_1 \rightarrow 0$), then this effect would become much more pronounced, and it would be impossible to switch the flow direction as discussed in chapter 4. Additionally, if spacing is an issue, then the previous setup with 1 mm spaces between each gate is still feasible and allows for additional gates to be fit into the same space, although it requires much more sophisticated control over the system. For instance, with a 1 mm gap, it is possible to fit 23 gates within the same space 3 gates fit with a 10 mm gap. As such, where the goal is the capture of many objects, only the complexity of the control system needs to be adjusted to handle the gates closer together.

Finally, using the 1 mm gap example, the flow rates through the rest of the system can also be shown with this configuration in Figure 5.7:

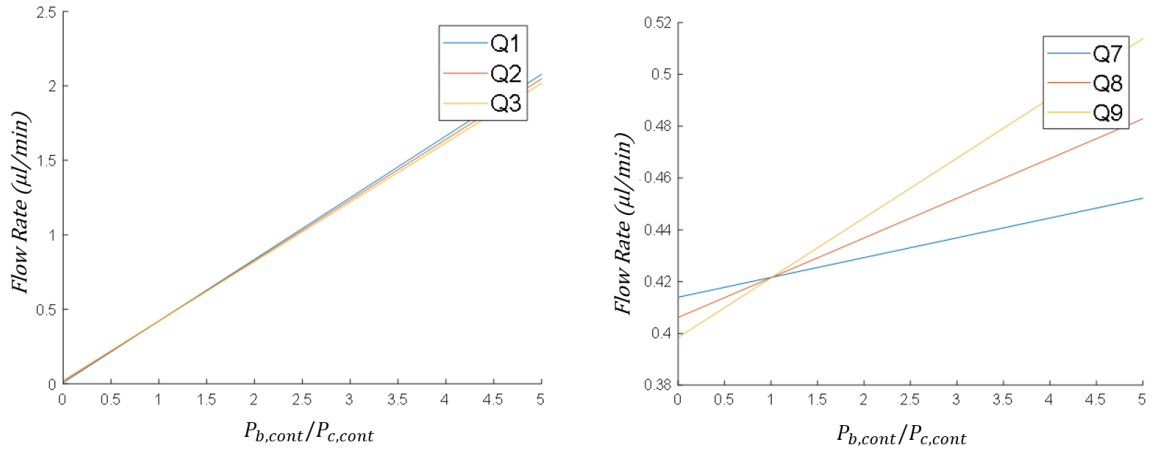

Figure 5.7: Predictions for the flow rates within the entire microfluidic device with 1 mm gaps between each restriction for $P_{c,cont}$ = 100 mbar.

Figure 5.7 highlights the expected trend in the microfluidic device where, as $P_{b,cont}$ increases, $Q_{1,2,3}$ also increase linearly with the flow rates as shown in figure 5.7(a). As expected also, the differences between each of the channels is the amount of flow rate moving through the gate restrictions. For example, when the flow is expected to be reversed with $P_{b,cont} \rightarrow 0$, Q_3 becomes higher than Q_2 due to the addition of flow rate from the third gate. This is reflected in the control channel vales with Q_9 rapidly increasing due to flow influence from all 3channel gates contributing to the flow rate, compared to Q_7 which only increases due to the contribution of flow from the third gate. The reason why $Q_{7,8,9}$ never reach close to 0 is due to $Q_{c,cont}$ being held constant at 100 mbar, if this was reduced then they would also tend towards zero as indicated by the trend in figure 5.7(b).

To demonstrate this, experimental analysis was performed by setting up a microfluidic chip as previously described with the same inlets and outlets and with 1 mm gaps between each gate of which there are 3 in total. Initially, to understand the filling of the device, the control pressure was held constant at 250 mbar, while the bulk pressure was increased linearly from 1 to 500 mbar with a change of 1 mbar every second. The bulk flow was filled with water combined with red dye as indicated by the darker colour in the channel, while the control flow was only water as indicated by the lighter colour in the channel. This is illustrated in Figure 5.8.

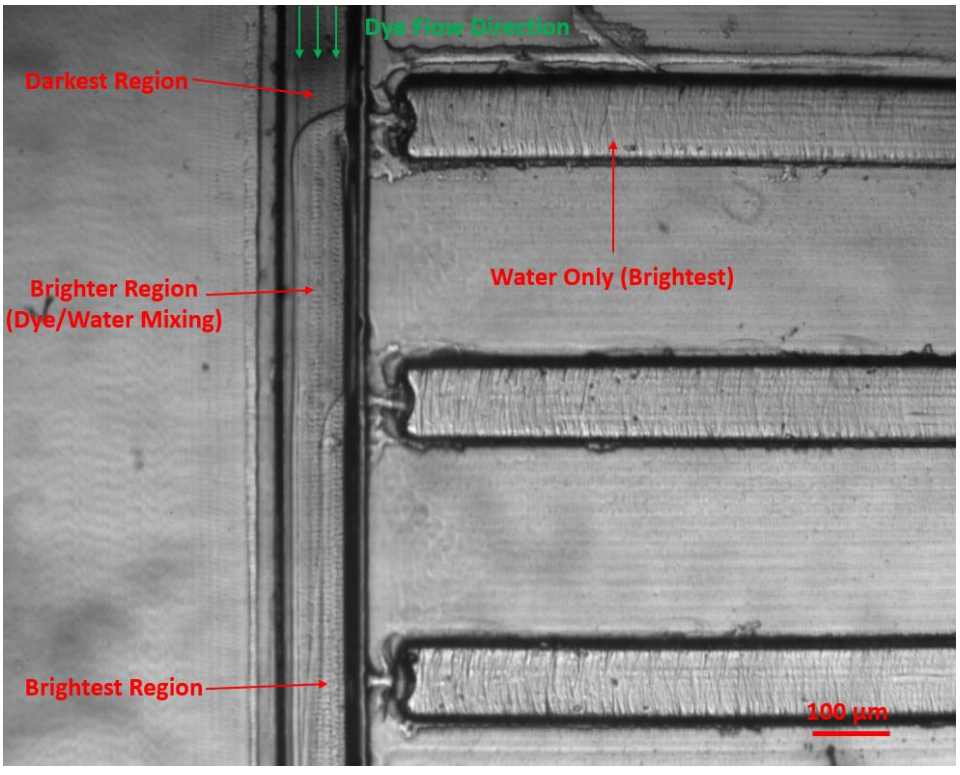

Figure 5.8: General initial state of the device at $P_{b,cont}$ = 240 mbar and $P_{c,cont}$ = 250 mbar. The darker areas indicate fluid from the bulk inlet as water filled with red dye, the brighter areas indicate fluid from the control inlet as water only.

Figure 5.8 above presents an example of how the device performs when $P_{b,cont} << P_{c,cont}$, where three shades of darker areas can be seen. The top channel inlet area at the top left contains the darkest colour and becomes progressively lighter as it passes by each of the gates. This is due to the water from the control channel being pushed through the gate and mixing with the red dye, effectively diluting it as it moves further downstream in the channel. This can be seen progressively occurring in Figure 5.6 where, after each gate, the bulk flow channel colour becomes lighter as more water is mixed. Moreover, after passing the first gate, the bulk flow is pushed far to the left and separate streamlines can be observed between the bulk flow and the now mixed bulk/control flow. This occurs again as the bulk flow passes the second gate where another streamline can be seen to form, and the shade of colour becomes lighter. Finally, at the third gate, the dye is almost completely diluted by the additional water making the streamline less obvious to observe. As the $P_{b,cont}$ pressure increases, the fluid begins to move from the bulk channel into the control channel and the streamlines from the control inlets become condensed and surrounded by the bulk flow, as exhibited by Figure 5.9.

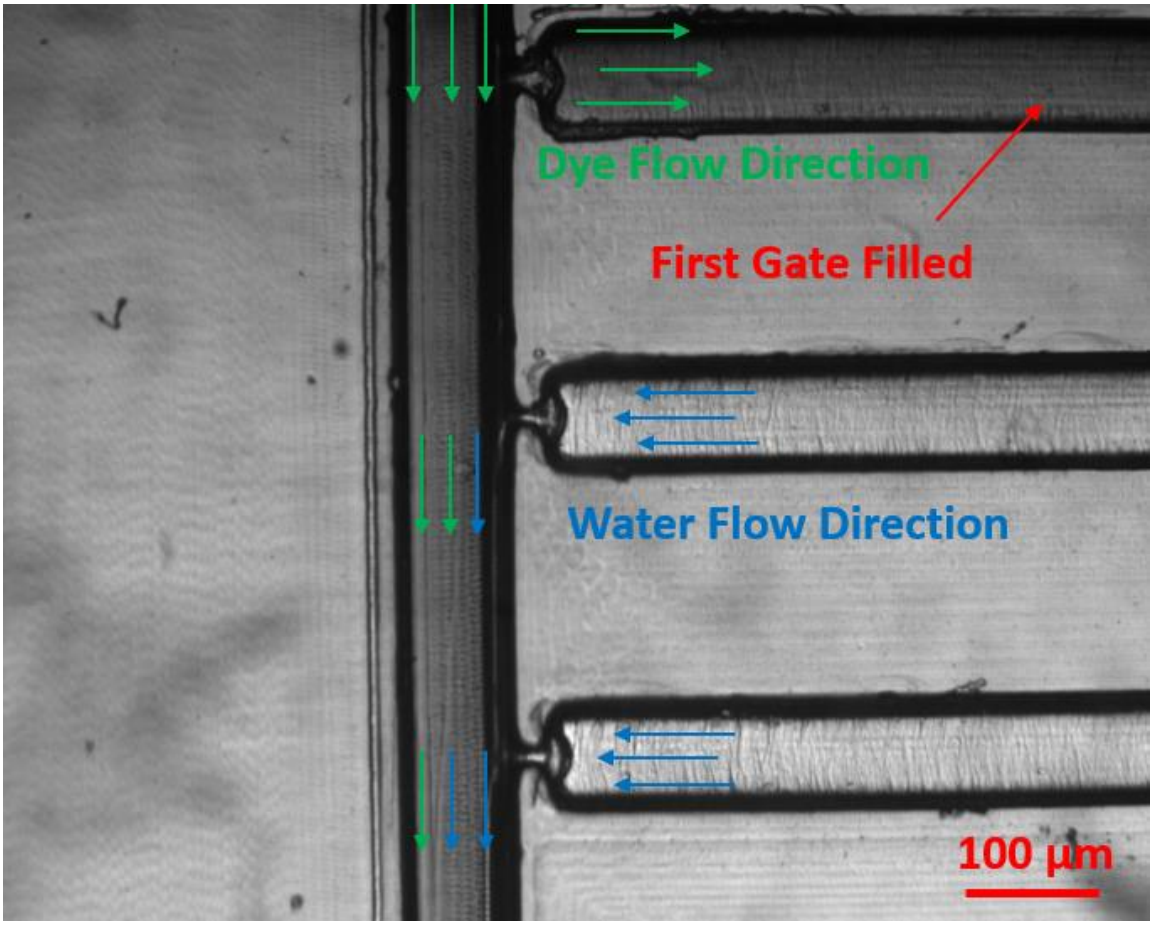

Figure 5.9: First gate being filled in the microfluidic channel at $P_{b,cont}$ = 260 mbar with fluid from the bulk channel moving into the control channel with $P_{c,cont}$ = 250 mbar.

Figure 5.9 then highlights the device state which is much further than the critical point of Q_4, as fully developed flow can be seen within the first gate. Gates 2 and 3 are filled with water and flowing from the control channel into the bulk channel as indicated by a thin stream of lighter fluid moving within the darker fluid originating at the gate restriction and which is water that has not yet mixed with the dye. An interesting phenomenon occurs when reaching Q_{crit} as shown in Figure 5.10:

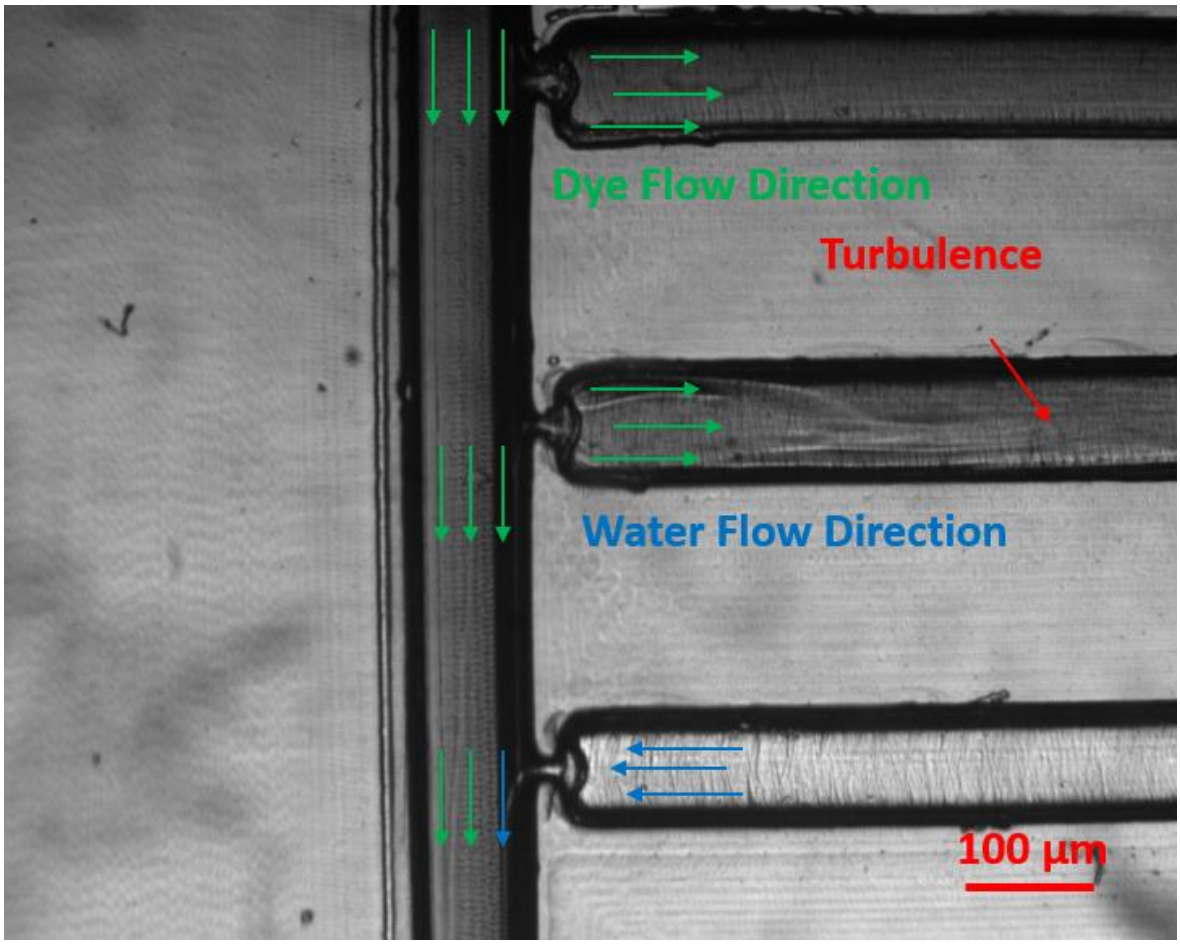

Figure 5.10: Turbulent flow in the second gate as $Q_{5,crit}$ is reached at $P_{b,cont}$ = 262.

As $Q_{5,crit}$ is reached, the gate shortly undergoes a transition period where a turbulent shockwave can be observed as highlighted by the bent streamlines and mixing of the two fluids. Further increasing the pressure then leads to a clear channel again after this turbulence where all the bulk flow is pushed to the top side of the channel. A clear shear is then developed between each fluid as illustrated in Figure 5.10.

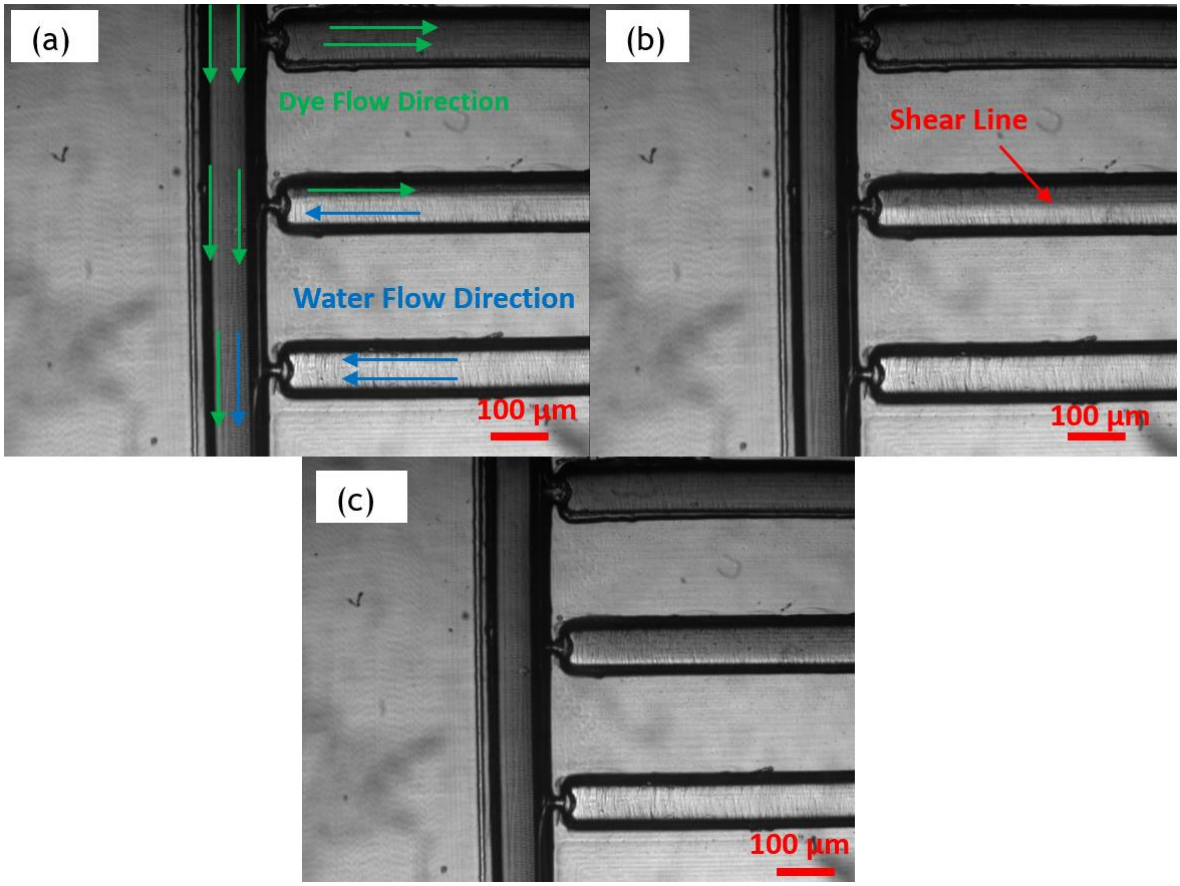

Figure 5.11: (a) Shear flow beginning to be seen in the second gate as $P_{b,cont}$ is increased further at 262.1 mbar. (b) Shear flow of the bulk flow developing further until it is half the channel at $P_{b,cont}$ = 262.3 mbar. (c) Shear flow of the bulk flow almost covering the channel before reaching the next flow transition at $P_{b,cont}$ = 262.5 mbar.

The shear between each of the fluid types is clearly defined in Figure 5.11 as the darker area, indicating more fluid from the bulk channel was entering the gate, increased linearly with finite pressure increases. 0.1 pressure increase increments were required to observe the gradual increase of the gate progressively being filled with the dyed fluid. Figure 5.11(a) demonstrates that the pressure in the bulk channel is slightly lower than the control channel. This highlights the action of each of the pressures influencing each other over the gate, as in Figure 5.11(b) they are shown to effectively be equal, and in Figure 5.11(c) the pressure in bulk channel is shown to be slightly higher than in the control channel.

At $P_{b,cont}$ = 262.6 mbar, the fluid went into the final transition as the water from the control channel was completely eliminated from the gate and the flow was fully reversed, as attested by Figure 5.12 below.

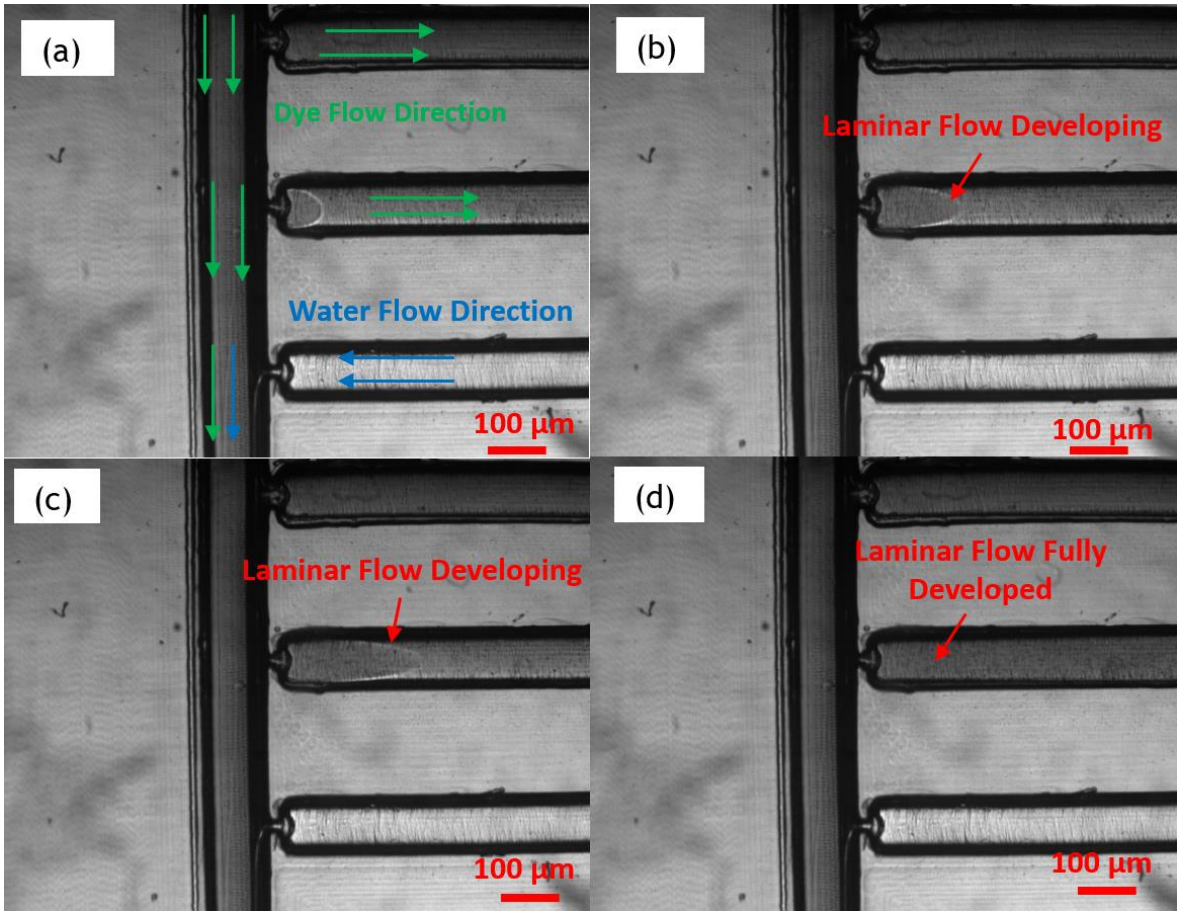

Figure 5.12: Development of a typical laminar flow progression at $P_{b,cont}$ = 262.6 mbar in gate 2. (a) shows the flow beginning to form. (b) shows the flow developing into a typical laminar flow profile. (c) shows the laminar profile extending further from the inlet. (d) shows the laminar flow being completely developed and the streamline being completely invisible.

Figure 5.12 highlights what was found to occur between the point at which the pressures on each side of the gate are approximately equal and the point at which the pressure in the bulk flow exceeds the control flow by a larger margin. A laminar streamline can be seen to form as soon as $P_{b,cont}$ reached 266 mbar in Figure 5.12(a), which can be observed to develop further down the gate channel in Figures 5.12(b) and 5.12(c), until it becomes completely developed in 5.12(d). During this process, the pressure was held constant as it occurred over a period of approximately 0.3 seconds. Therefore, this can be explained as hysteresis of the system as it transitions from its previous state into a new stable state with the flow switching to move from the bulk channel into the control channel.

Finally, in Figure 5.13 below, the filling of the third gate can be observed following a similar process to that of the previous gate.

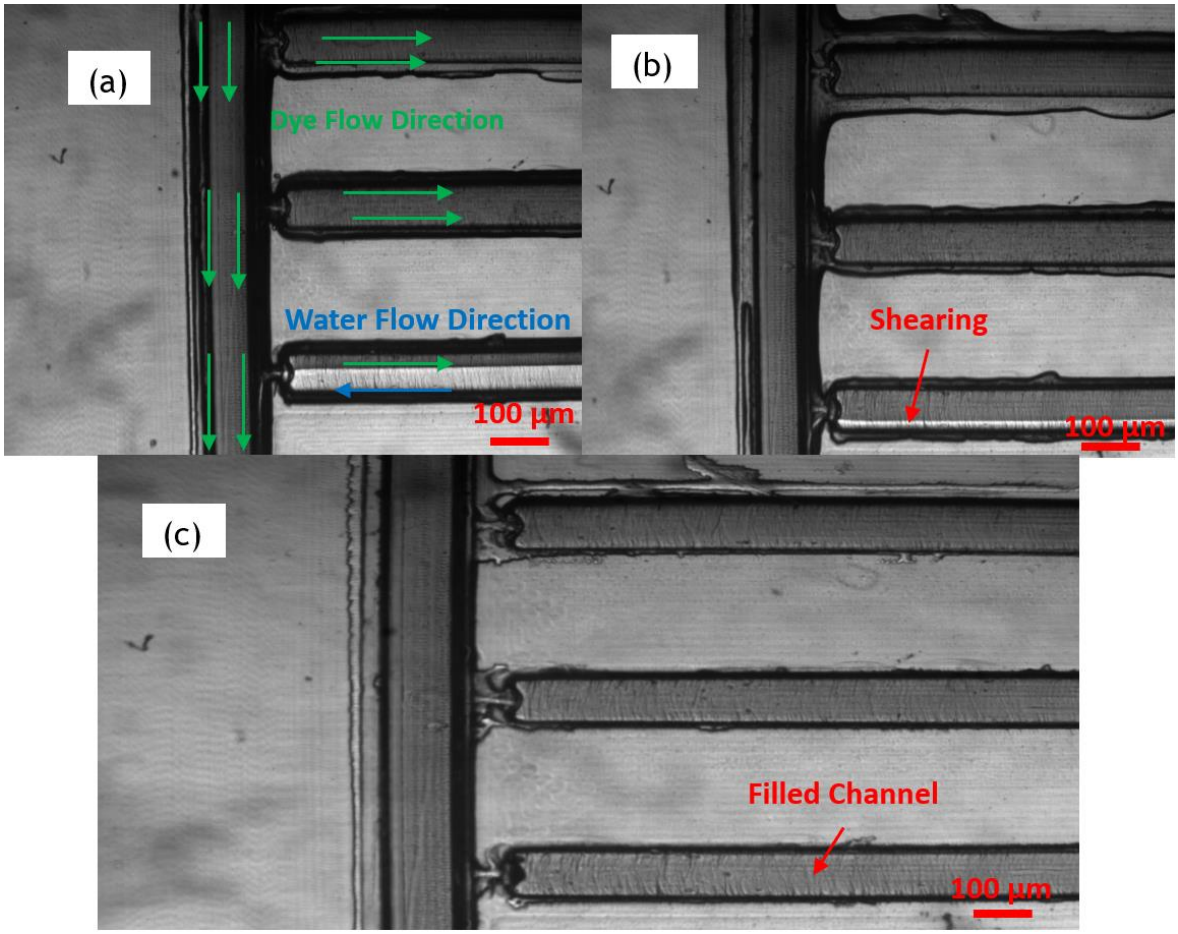

Figure 5.13: Filling of the third gate with the bulk flow moving into the third gate channel (a) Shear flow developing again with the bulk flow at $P_{b,cont}$ = 268 mbar (b) Further development of the shear flow at $P_{b,cont}$ = 268.3 mbar (c) Complete filling of the third channel at $P_{b,cont}$ = 268.4 mbar.

Highlighted within Figure 5.13 is the filling of the channel with the previously seen shear flow. As the bulk flow channel pressure increases, the amount of water in the channel reduces again until the flow direction is switched, as it can be observed by its complete filling with the bulk flow fluid. Therefore, this confirms that all the channels can be filled with the counter current flow setup. Next, to demonstrate the ability of the device to switch the flows back, the same experiment was performed with $P_{b,cont}$ = 270 mbar and held constant as this is the condition for all 3 of the channels to be in the first state as determined experimentally. For this setup, the fluids were switched with the dyed fluid entering the control inlet to better demonstrate the physical effects occurring. The effects of the first channel being filled are illustrated in Figure 5.14.

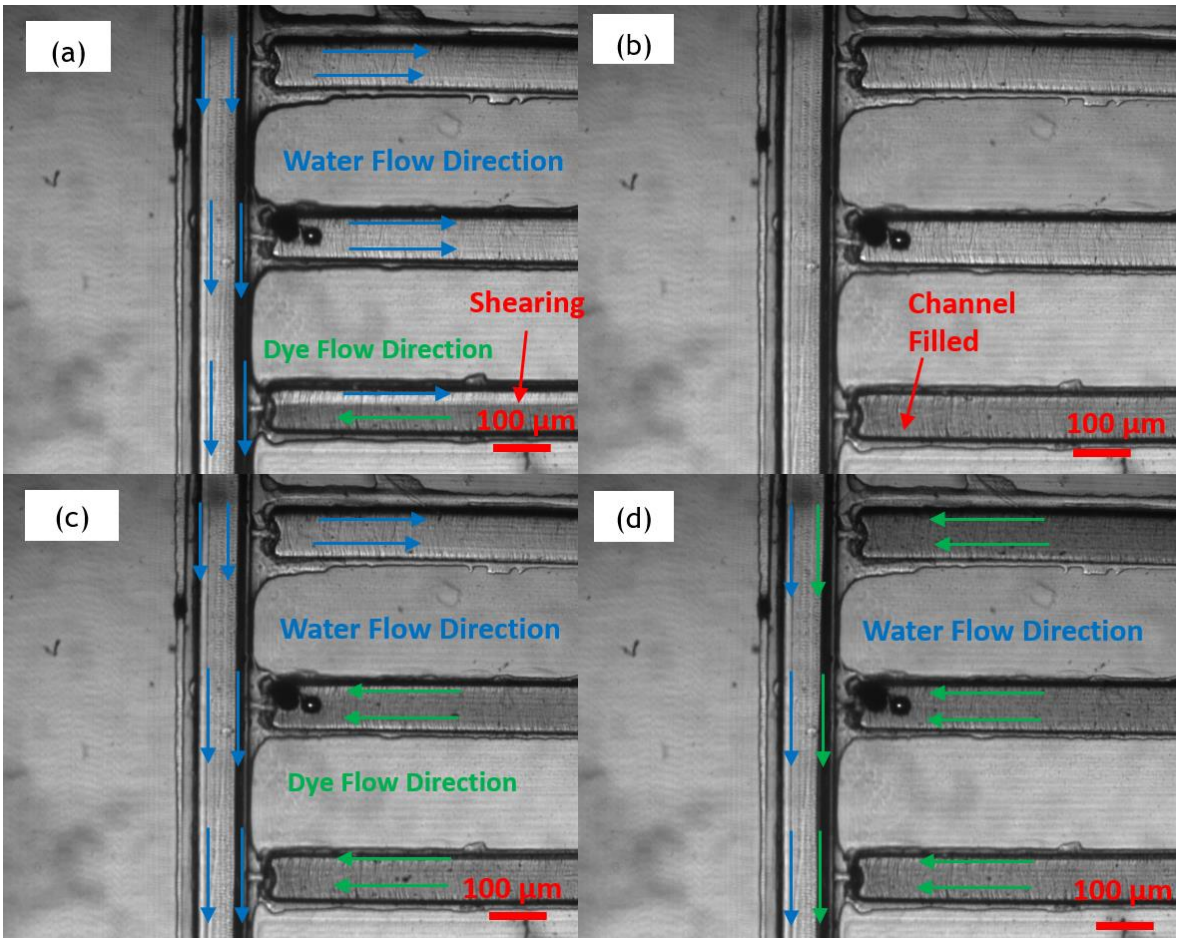

Figure 5.14: Filling of the third gate with the control flow moving into the third gate channel with $P_{b,cont}$ = 270 mbar. (a) Shear flow developing again with the bulk flow at $P_{c,cont}$ = 252 mbar. (b) Complete filling of the third channel with $P_{c,cont}$ = 252.3 mbar. (c) Complete filling of the second channel at $P_{c,cont}$ = 258.4 mbar. (d) Complete filling of the first channel at $P_{c,cont}$ = 261.6 mbar

Figure 5.14 demonstrates the reverse of the flows required to release each object individually. Figure 5.14(a) shows the same shearing effect occurring as seen previously during the filling state of the device, although with the fluids reversed in this instance. Interestingly, it seems that the profile of the shear line is exactly the same as during the filling procedure where it is almost horizontal with a slight increase in the bulk flow fluid closer to the gate restriction. Figure 5.14(b) demonstrates the filling of the third channel where the shear between the two fluids has been eliminated and it is completely filled. Figure 5.14(c) highlights the filling of the third channel, and it can be observed that there is some debris present in the channel which accumulates as particles from the dye. This is

likely due to the restriction blocking large particles from moving through, although in the position where the material has been deposited, fluid can still move around it and enter the bulk flow channel. This was not observed when the dye was in the bulk flow channel as, if a blockage like this formed, it would increase in size until it was dislodged from the gate (rather than being held in position) by collecting other particles, or the dye would safely pass through the restriction into a larger channel where no blockage would occur. Finally, in Figure 5.14(d) the first channel can be seen to be filled with the dyed fluid, indicating that the flow in each of the gate channels has been completely reversed from the initial fluid condition due only to a pressure increase in the control channel. The previous streamlines appear to be hidden in the reversed state because of the streamlines from the gates hugging the right wall where it is obscured visually, and due to the concentration of the particles flowing through the restriction being small, as opposed to the previous scenario where a high concentration of dyed fluid was influenced by a smaller volume of water which is easier to identify visually.

Finally, to evaluate the model developed, the critical values for Q were evaluated based on the pressures for when each channel flow rate was switched (in both directions). The points chosen from the experimental analysis were when the channel was completely filled with red dye in each device state, as this would be a requirement for any objects to be captured or released, as Figure 5.15 below evaluates:

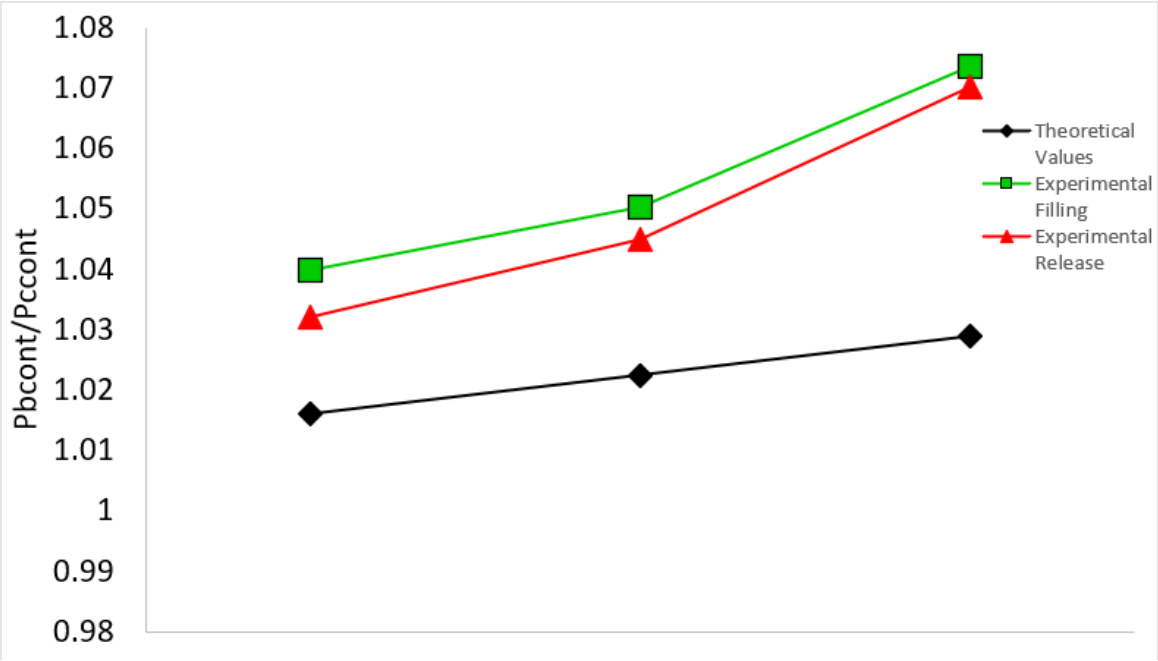

Figure 5.15: Comparison of the theoretically calculated $P_{b,cont}/P_{c,cont}$ for the critical flow rates to the determined experimental values for the flow rate at each gate.

Figure 5.15 then displays the differences between the calculated values of $P_{b,cont}/P_{c,cont}$ for each of the channels where Q_n = 0. The general trend for the theoretical values is observed to be linear, whereas there is a close match $\Delta P_{b,cont}/P_{c,cont}$ between Q_4 and Q_5 but there is a larger jump in the required $\Delta P_{b,cont}/P_{c,cont}$ value between Q_5 and Q_6 based on the experimental results to achieve the critical flow rate. This may be due to unexpected defects within the third gate restriction, which means that a slightly higher bulk pressure is required to allow the fluids on each side to reach an equal pressure. In general, the experimental values are relatively higher than the theoretical ones, which is likely a consequence of not taking the 3D aspects of the design within the theoretical analysis into consideration. This includes pressure losses such as at the device inlets and outlets where the flow is required to turn 90 degrees that was not included in the analysis, as well as discounting any exit effects. The outlet pressure loss should be relatively small compared to the rest of the device (approximately 7 Pa across the length of tubing to waste reservoir), but due to the sensitivity of the pressure requirements, may cause the differences from the theoretical model. The experimental filling and release values are relatively similar; however, the small increase in the filling procedure may be a result of the initial resistance of the flow entering the control channel due to the restriction. The resistance through this channel, although it has a small length, is a factor of 100 higher than that in other channels because of the relatively small dimensions, whereas during release for the fluid to enter from the control channel, it is flowing through the larger 300 µm channel first before reaching the restriction.

The errors of the theoretical model values were 2.3% and 1.56% for $Q_{4,crit}$ for experimental filling and experimental release respectively, 2.65% and 2.14% for $Q_{5,crit}$ and 4.1% and 3.84% for $Q_{6,crit}$. This indicates that the theoretical model is a good predictor for giving target values for the system to begin controlling the pressure at. This means that, for any redesigns of the device, only the external flow rate and resistance are necessary for calculation and inputting these values into the theoretical model will give a reasonable target range to find when the flows will switch. This also means that when adding in further gates, the theoretical calculations will still give $P_{b,cont}/P_{c,cont}$ values below a 5% error rate. As such, for redesigns, it is not necessary to run through the searching procedure of

experimentally testing 1 mbar to 500 mbar, as the model can determine the appropriate range for a given $P_{c,cont}$ to find the critical flow rate values.

5.5 Conclusion

A theoretical model has been developed throughout this chapter to demonstrate the fluid control requirements of any device with the same inlet conditions. The parameters of the theoretical device can be easily manipulated to match any design changes and provides a method of computationally testing devices prior to manufacturing them. This includes determining the approximate control schemes for different numbers of gates, or the distance between each gate and whether the required precision of the control system is acceptable for each design. The model was validated experimentally and demonstrates that the theoretical model follows experimental results with less than 5% error. Several phenomena were also observed during the flow switching procedure including an initial turbulent shockwave to the system upon changing directions, a shearing effect between each fluid while the pressure is increased, and finally laminar flow development with a typical semi-circular streamline profile seen as expected in square microchannels. There is a potential for the model to become more sophisticated by including various effects that were ignored such as inlet conditions, fluids moving around bends/angles, as well as other 3D effects on the fluid flow.

6. Conclusion

6.1 Introduction

This thesis proposes a novel microfluidic technique for the capture, isolation and retrieval of objects or cells using active flow control. The proposed device is a unique method exploiting counter-current flows for capture and release of individual objects through precise pressure control on a microfluidic platform. The main operational steps are individual capture into all present gates in the system, and subsequent individual release from each gate for isolation of the objects from a larger population.

In the following sections, the developed methodology, the main results, and the demonstration of the relation between the main chapters, contribution of this thesis and future directions of this study are outlined.

6.2 Summary of the Thesis

The main development throughout this thesis is towards the manufacture and understanding of the novel counter-current flow technique.

Initially, a rapid prototyping method capable of manufacturing dimensions of about 100 µm was developed in Chapter 3. This served the purpose of further developing rapid prototypes of the design for initial proof-of-concept testing due to it being an unexplored technique, for which several design iterations may be required. A novel red femtosecond laser manufacturing of steel moulds was developed for replica moulding of microfluidic devices to produce channels of 300 µm height and width, and gates with target restrictions of 100 µm. The manufacturing method was evaluated by measuring the surface co-ordinates of the steel mould and resulting PDMS replica and comparing them to the original CAD model design. Because of the nature of the laser ablation process, high errors were recorded around channel walls, as well as sharp geometries leading to overshoots in these areas. The errors in the main channels were deemed acceptable due to their lack of impact on the device function. A more significant overshoot of 50 µm was noted around the gate geometry, likely due to the original geometry tapering to a single point, with a sharp wall on the other side. As a result, target objects/cells would have to be re-evaluated after manufacturing with this technique. Low force stereolithography was also examined in the

context of the present design. The curing process was the most significant factor in enabling successful peeling of the device with a low temperature, longer cure yielding more successful results.

A CFD simulation was developed to further understand the device, the key parameters during its operation by introducing particles into the flow, and their interaction with the fluid environment. The model highlights the importance of precise pressure control within the bulk and control channels as this determines the direction of the flow rate for object capture/release. The simulation setup was applied to alternative designs, and it was found that proximity to the inlet conditions led to the device being unable to control the gates due to the opposing channels failing to overcome the pressure supplied by the other for flow direction reversal. A theoretical model was then developed from the simulation to offer a solution to a 9-gate design as during ICSI, it is preferred for many eggs to be collected. As such the technique should be able to manage as many objects. The simulation was then experimentally validated by demonstrating capture, isolation and retrieval of 150 µm diameter microbeads.

Finally, a theoretical analysis was carried out for the fluid control in the device using electronic circuit analogies. A Matlab 2017b script was developed to solve the simultaneous equations formed using Gaussian-Jordan elimination and the critical flow rates of 0 µl/min were determined theoretically. The theoretical model was then validated experimentally using PMMA microfluidic structure and good agreement was established between the results and the model, although the model predicted lower pressure requirements, likely due to not accounting for certain losses through the system, such as the flow moving through bends and junctions. However, the method was again demonstrated through only fluid control and specific phenomena were noted during device function such as turbulent shockwaves during flow direction switching, and laminar shearing when the bulk and control pressures were approximately equal.

6.3 Contribution of Thesis

This thesis focused on the development of a microfluidic technique for individual capture/isolation of cells/objects with further application to ICSI methods. The research contributions of this research project are as follows:

- A novel microfluidic manufacturing technique using red femtosecond lasers for the ablation of steel moulds for rapid prototyping of microfluidic devices. Manufacturing considerations of replication processes due to the nested inner structure of the gates within the design have also been highlighted.

- A full CFD simulation model with particle tracking has been developed and experimentally validated to assess the ability of the technique to influence cells within the device. The simulation can also be used to allow for rapid redesign testing and for determining co-ordinate positions of the gates.

- A theoretical analysis of the device founded on electrical circuit analogies for determining precise pressure requirements based on controller inputs for fluid direction and magnitude control within the device.

6.4 Future Directions

In this thesis, the main object that has been manipulated by the device is microbeads or smaller dye particles. To further evaluate the impact of the device structure on cells, cells should be placed into the device with the dimensions that have already been determined in this thesis. This will allow for the understanding of the force experienced by the cells and determine whether any cell damage will occur. The theory for this evaluation has already been developed and is shown in Figure 6.1 below:

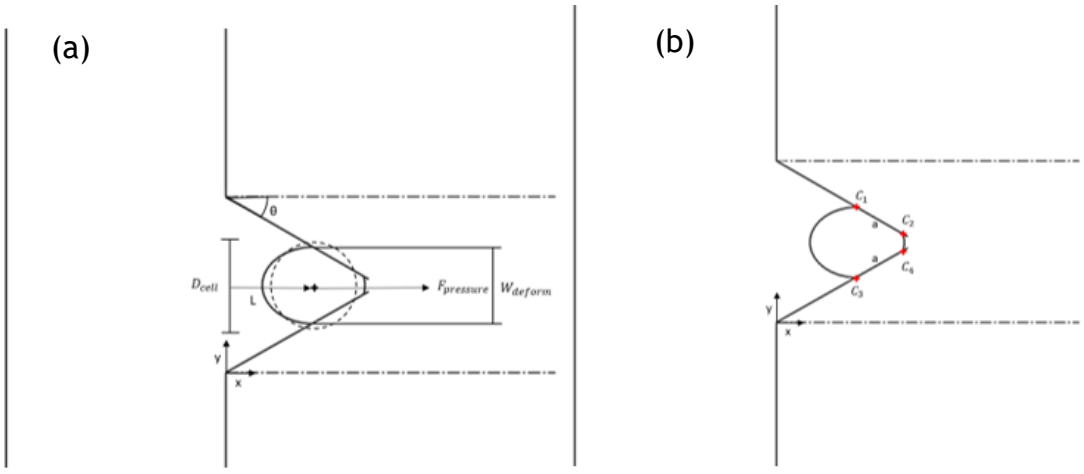

Figure 6.1: Schematic setup for the evaluation of cell deformation and damage within the gates of the microfluidic device. 6.1(a) shows the general geometric considerations required to evaluate the cell damage. 6.1(b) shows positions of the edge contact points of the cell.

Using Figure 6.1(a) as reference, the Tatara model for large deformations of objects could be utilised to determine the cell modulus, and the mechanical properties of the cell [127].

$$E = \frac{3(1-\nu^2)F_{compress}}{2(D_{cell}-W_{deform})a} - \frac{2F_{compress}}{\pi\left(D_{cell}-W_{deform}\right)f(a)} \quad (6.1)$$

Where ν is the poisson ratio, $F_{compress}$ is the compression force applied to the cell from the restriction due to the pressure on the particle, D_{cell} is the cell diameter, W_{deform} is the deformed width of the cell at its centre, a is the contact radius and f(a) is the characteristic length of the non-spherical geometry. Equation 6.1 then offers a method of determining the modulus of the cell and can be combined with determination of cell death through experimental analysis within the device. As precise pressure control and flow rate have now been demonstrated, the forces acting on the cell would be easily determined. The parameter a can be determined through visual measurement by determining the co-ordinates of the contact points C_{1-4} and inputted into equation 6.2:

$$a = \sqrt{(C_{1,y}-C_{2,y})^2 + (C_{2,x}-C_{1,y})^2} \quad (6.2)$$

With this, the forces, modulus and damage to cells could be evaluated as a result of capture within the device.

Another manufacturing technique should additionally be determined for the replication of 3D gate structures of 2 µm. This is to allow the design to be assessed with sperm cells, which has been a challenge to accomplish so far. Two photon polymerisation 3D printing techniques are also a good candidate for initial testing of the device as they have the required feature resolution as well as capability of developing 3D geometry. With this, the technique can be evaluated using an active cell and adjusted in order to manage cells flowing within the system using animal models such as bull sperm as it matches closely the motility patterns of human sperm.

Finally, the device would then have to be integrated to a wider structure and clinically evaluated. This would include inlets for sperm, medium inlets, valves, and visual sensing to operate the device. This would then ensure reliability of the device in a clinical setting and allow it to be employed by embryologists.

Appendix – Code used to solve equation 5.25

```
     clear all
clc
clf
close all

format shortEng
%List constants for channel
R1 = 5.14E+10;
R2 = 3.57E+9;
R3 = 3.57E+9;
R4 = 4.32E+10;
R5 = 2.94E+13;
Rx = R1+R2;
Ry = R3+R4;
Rexternal = 2.34E+12;
%Pb pressure initialisation
Pbcont = 1;
%Pc controller constant value
Pccont = 100;

for i=1:1:500
    %Q in m/s unit conversion
Qb = Pbcont*0.2531*1E-09*0.0166667;
Qc = Pccont*0.2531*1E-09*0.0166667;

%Velocity calculation
Area = pi*((3.95E-4)^2);
vb = (Pbcont*0.0852)/1000;
vc = (Pccont*0.0852)/1000;


%External flow rate in m/s
Qbex = Area*vb;
Qcex = Area*vc;

%Convert P into pascals
Ppasb = Pbcont*100;
Ppasc = Pccont*100;

%Determine Pin
Pinb = Ppasb - (Qbex*Rexternal);
Pinc = Ppasc - (Qcex*Rexternal);

%Evalute Matrix Value
Pcconst = Pinc - ((Qc)*R4);
Pbconst = Pinb - ((Qb)*R1);

%Pressure-based constants
Px = Pinb-((Qc)*R1)-Pinc +((Qc)*R4);


%For Qb>>Qc
%Equation Matrix
A = [1 0 1 0 0 0 0 Qb;
     -1 1 0 1 0 0 0 0;
```

```
     0 0 0 0 -1 1 0 Qc;
     0 0 0 1 0 1 -1 0;
     R2 0 -R5 R5 0 0 R2 0;
     0 R3 0 -R5 R5 R3 0 0;
     0 0 R5 0 0 -R3 -R2 Px;
     R2 0 0 R5 0 -R3 0 Px;
     R2 R3 0 0 R5 0 0 Px;
    ];

%Gaussian-Jordan Elimination
R = rref(A);

R;

%Store flow rates for each pressure value based on relevant matrix
element
%Conversion back into ul/s
Q1(i) = (R(1,8))*1E09;
Q2(i) = (R(2,8))*1E09;
Q3(i) = ((R(2,8))-(R(5,8)))*1E09;
Q4(i) = (R(3,8)*1E09);
Q5(i) = (R(4,8))*1E09;
Q6(i) = ((R(5,8))*1E09);
Q7(i) = (R(6,8))*1E09;
Q8(i) = (R(7,8))*1E09;
Q9(i) = ((R(7,8))+(R(3,8)))*1E09;
Pfrac(i) = Pbcont/Pccont;

%Increment Pbcont
Pbcont = Pbcont + 1;
end

%Plot each flow rates into separate figures
figure
hold on
plot(Pfrac,Q4,'DisplayName','Q4')
plot(Pfrac,Q5,'DisplayName','Q5')
plot(Pfrac,Q6,'DisplayName','Q6')
xlabel('Pbcont/Pccont','fontsize',16)
ylabel('Flow Rate ({\mu}l/min)','fontsize',16)
hold off
lgd=legend('Q4','Q5','Q6')
lgd.FontSize=16;

figure
hold on
plot(Pfrac,Q1,'DisplayName','Q1')
plot(Pfrac,Q2,'DisplayName','Q2')
plot(Pfrac,Q3,'DisplayName','Q3')
xlabel('Pbcont/Pccont','fontsize',16)
ylabel('Flow Rate ({\mu}l/min)','fontsize',16)
hold off
lgd=legend('Q1','Q2','Q3')
lgd.FontSize=16;

figure
hold on
plot(Pfrac,Q7,'DisplayName','Q7')
plot(Pfrac,Q8,'DisplayName','Q8')
```

```
plot(Pfrac,Q9,'DisplayName','Q9')
xlabel('Pbcont/Pccont','fontsize',16)
ylabel('Flow Rate ({\mu}l/min)','fontsize',16)
hold off
lgd=legend('Q7','Q8','Q9')
lgd.FontSize=16;
```

List of References

[1] Definitions of infertility and recurrent pregnancy loss. *2008 Compend Pract Comm Rep* 2008; 90: S60.

[2] Hull MG, Glazener CM, Kelly NJ, et al. Population study of causes, treatment, and outcome of infertility. *Br Med J Clin Res Ed* 1985; 291: 1693.

[3] Agarwal A, Mulgund A, Hamada A, et al. A unique view on male infertility around the globe. *Reprod Biol Endocrinol* 2015; 13: 37.

[4] Barak S, Baker H. *Clinical Management of Male Infertility*. MDText.com, Inc., South Dartmouth (MA), http://europepmc.org/abstract/MED/25905383 (2000).

[5] Hamada A, Esteves SC, Nizza M, et al. Unexplained Male infertility: diagnosis and Management. *Int Braz J Urol* 2012; 38: 576–594.

[6] Palermo G, Joris H, Devroey P, et al. Pregnancies after intracytoplasmic injection of single spermatozoon into an oocyte. *Orig Publ Vol 2 Issue 8810* 1992; 340: 17–18.

[7] Vizag IVF Centre. Intra Cytoplasmic Sperm Injection - ICSI. *Vizag IVF Centre*, https://www.vizagivfcentre.com/icsi (2022).

[8] Organization WH. *WHO laboratory manual for the examination and processing of human semen*. World Health Organization, 2021.

[9] Björndahl L. The usefulness and significance of assessing rapidly progressive spermatozoa. *Asian J Androl* 2010; 12: 33–5.

[10] Lindholmer CH. The Importance of Seminal Plasma for Human Sperm Motility. *Biol Reprod* 1974; 10: 533–542.

[11] Human Fertilisation, Embryology Authority (HFEA). Anonymised register data for 2017-2018. *HFEA: UK fertility regulator*, http://hfea.gov.uk/about-us/our-data/#ar (2020, accessed 20 February 2023).

[12] The Fertility & Gynaecology Academy. Success Rates. *Fertility Clinic in london for IVF - The Fertility Academy*, https://www.fertility-academy.co.uk/about-us/success-rates/ (2023, accessed 25 March 2022).

[13] King's Fertility Limited. Our success rates. *Leading IVF & Fertility Treatment Clinic in London, UK - King's Fertility*, https://www.kingsfertility.co.uk/our-success/ (2022, accessed 30 November 2022).

[14] Manchester University NHS Foundation Trust. Clinical Pregnancy Success Rates. *Saint Mary's Hospital*, https://mft.nhs.uk/saint-marys/services/gynaecology/reproductive-medicine/clinical-pregnancy-success-rates/ (2023, accessed 5 June 2022).

[15] Hull & East Riding Fertility. IVF & ICSI -A Closer Look. *Fertility Clinic in Yorkshire - Hull & East Riding Fertility*, https://www.hulleastridingfertility.co.uk/success-rates/ivf-a-closer-look/ (2022, accessed 25 April 2023).

[16] Manchester Fertility. IVF & ICSI Success Rates. *UK leading specialists in IVF treatment | Manchester Fertility*, https://www.manchesterfertility.com/about/success-rates/# (2023, accessed 25 April 2023).

[17] Friedler S, Raziel A, Strassburger D, et al. Factors influencing the outcome of ICSI in patients with obstructive and non-obstructive azoospermia: a comparative study. *Hum Reprod* 2002; 17: 3114–3121.

[18] Shen S, Khabani A, Klein N, et al. Statistical analysis of factors affecting fertilization rates and clinical outcome associated with intracytoplasmic sperm injection. *Fertil Steril* 2003; 79: 355–360.

[19] Quinn MM, Jalalian L, Ribeiro S, et al. Microfluidic sorting selects sperm for clinical use with reduced DNA damage compared to density gradient centrifugation with swim-up in split semen samples. *Hum Reprod* 2018; 33: 1388–1393.

[20] Preetam S, Nahak BK, Patra S, et al. Emergence of microfluidics for next generation biomedical devices. *Biosens Bioelectron X* 2022; 10: 100106.

[21] GENNET. Microfluidic Sperm Sorting. *GENNET*, https://www.gennet.cz/en/microfluidic-sperm-sorting (2023, accessed 25 April 2023).

[22] Europe IVF. Microfluidic sperm sorting chips. *Top IVF clinic in Prague, Czech Republic | Europe IVF*, https://europeivf.com/en/method/microfluidic-sperm-sorting-chips/ (2023, accessed 25 April 2023).

[23] Baldini D, Ferri D, Baldini GM, et al. Sperm Selection for ICSI: Do We Have a Winner? *Cells* 2021; 10: 3566.

[24] Care Fertility. ZyMot sperm selection for ICSI. *IVF & Fertility Clinics UK | Care Fertility*, https://www.carefertility.com/treatments-services/male-fertility-health/zymot (2022, accessed 25 April 2023).

[25] Saadat M, Taylor M, Hughes A, et al. Rapid prototyping method for 3D PDMS microfluidic devices using a red femtosecond laser. *Adv Mech Eng* 2020; 12: 1687814020982713.

[26] Xia Y, Whitesides GM. Soft Lithography. *Angew Chem Int Ed* 1998; 37: 550–575.

[27] Zhou J, Ellis AV, Voelcker NH. Recent developments in PDMS surface modification for microfluidic devices. *ELECTROPHORESIS* 2010; 31: 2–16.

[28] Mata A, Fleischman AJ, Roy S. Characterization of Polydimethylsiloxane (PDMS) Properties for Biomedical Micro/Nanosystems. *Biomed Microdevices* 2005; 7: 281–293.

[29] Berthier E, Young EWK, Beebe D. Engineers are from PDMS-land, Biologists are from Polystyrenia. *Lab Chip* 2012; 12: 1224–1237.

[30] Xia Y, McClelland JJ, Gupta R, et al. Replica molding using polymeric materials: A practical step toward nanomanufacturing. *Adv Mater* 1997; 9: 147–149.

[31] Shih T-K, Chen C-F, Ho J-R, et al. Fabrication of PDMS (polydimethylsiloxane) microlens and diffuser using replica molding. *Mater Adv Met MAM 2006* 2006; 83: 2499–2503.

[32] Madsen MH, Feidenhans'l NA, Hansen P-E, et al. Accounting for PDMS shrinkage when replicating structures. *J Micromechanics Microengineering* 2014; 24: 127002.

[33] Hupert ML, Guy WJ, Llopis SD, et al. Evaluation of micromilled metal mold masters for the replication of microchip electrophoresis devices. *Microfluid Nanofluidics* 2007; 3: 1–11.

[34] Chen PC, Wang ZP. A Rapid and Low Cost Manufacturing for Polymeric Microfluidic Devices. *Adv Mater Res* 2012; 579: 348–356.

[35] P. P. Shiu, G. K. Knopf, M. Ostojic, et al. Rapid Fabrication of Micromolds for Polymeric Microfluidic Devices. In: *2007 Canadian Conference on Electrical and Computer Engineering*. 2007, pp. 8–11.

[36] Wu C-H, Chen C-W, Kuo L-S, et al. A Novel Approach to Measure the Hydraulic Capacitance of a Microfluidic Membrane Pump. *Adv Mater Sci Eng* 2014; 2014: 1–8.

[37] Chichkov BN, Momma C, Nolte S, et al. Femtosecond, picosecond and nanosecond laser ablation of solids. *Appl Phys A* 1996; 63: 109–115.

[38] Lauer B, Jäggi B, Neuenschwander B. Influence of the Pulse Duration onto the Material Removal Rate and Machining Quality for Different Types of Steel. *8th Int Conf Laser Assist Net Shape Eng LANE 2014* 2014; 56: 963–972.

[39] Rousseau A, Laur V, Députier S, et al. Influence of substrate on the pulsed laser deposition growth and microwave behaviour of KTa0.6Nb0.4O3 potassium tantalate niobate ferroelectric thin films. *Thin Solid Films* 2008; 516: 4882–4888.

[40] Kumar Dubey A, Yadava V. Multi-objective optimisation of laser beam cutting process. *Opt Laser Technol* 2008; 40: 562–570.

[41] Petkov PV, Dimov SS, Minev RM, et al. Laser milling: Pulse duration effects on surface integrity. *Proc Inst Mech Eng Part B J Eng Manuf* 2008; 222: 35–45.

[42] Mata A, Fleischman AJ, Roy S. Fabrication of multi-layer SU-8 microstructures. *J Micromechanics Microengineering* 2006; 16: 276.

[43] Xu J, Locascio L, Gaitan M, et al. Room-Temperature Imprinting Method for Plastic Microchannel Fabrication. *Anal Chem* 2000; 72: 1930–1933.

[44] Fiorini GS, Chiu DT. Disposable microfluidic devices: fabrication, function, and application. *BioTechniques* 2005; 38: 429–446.

[45] Li Y, Zhang H, Yang R, et al. In-plane silicon microneedles with open capillary microfluidic networks by deep reactive ion etching and sacrificial layer based sharpening. *Sens Actuators Phys* 2019; 292: 149–157.

[46] K. R. Williams, K. Gupta, M. Wasilik. Etch rates for micromachining processing-Part II. *J Microelectromechanical Syst* 2003; 12: 761–778.

[47] H. Wensink, J. W. Berenschot, H. V. Jansen, et al. High resolution powder blast micromachining. In: *Proceedings IEEE Thirteenth Annual International Conference on Micro Electro Mechanical Systems (Cat. No.00CH36308)*. 2000, pp. 769–774.

[48] Nguyen N-T. Chapter 4 - Fabrication technologies. In: Nguyen N-T (ed) *Micromixers (Second Edition)*. Oxford: William Andrew Publishing, pp. 113–161.

[49] Laermer F, Franssila S, Sainiemi L, et al. Chapter 21 - Deep Reactive Ion Etching. In: Tilli M, Motooka T, Airaksinen V-M, et al. (eds) *Handbook of Silicon Based MEMS Materials and Technologies (Second Edition)*. Boston: William Andrew Publishing, pp. 444–469.

[50] Muñoz P, Yong YS, Dijkstra M, et al. Double metal layer lift-off process for the robust fabrication of plasmonic nano-antenna arrays on dielectric substrates using e-beam lithography. *Opt Mater Express* 2019; 9: 2046–2056.

[51] Xue B, Geng Y, Yan Y, et al. Rapid prototyping of microfluidic chip with burr-free PMMA microchannel fabricated by revolving tip-based micro-cutting. *J Mater Process Technol* 2020; 277: 116468.

[52] Chen X, Zhang L. Review in manufacturing methods of nanochannels of bio-nanofluidic chips. *Sens Actuators B Chem* 2018; 254: 648–659.

[53] Raoufi MA, Razavi Bazaz S, Niazmand H, et al. Fabrication of unconventional inertial microfluidic channels using wax 3D printing. *Soft Matter* 2020; 16: 2448–2459.

[54] Carnero B, Bao-Varela C, Gómez-Varela AI, et al. Microfluidic devices manufacturing with a stereolithographic printer for biological applications. *Mater Sci Eng C* 2021; 129: 112388.

[55] Liu X, Dong Z, Zhao Q, et al. Optimization of micromilled channels for microfluidic applications using gas-blowing-assisted PDMS coating. *Microfluid Nanofluidics* 2020; 24: 11.

[56] Liao Y, Song J, Li E, et al. Rapid prototyping of three-dimensional microfluidic mixers in glass by femtosecond laser direct writing. *Lab Chip* 2012; 12: 746–749.

[57] Kotz F, Risch P, Arnold K, et al. Fabrication of arbitrary three-dimensional suspended hollow microstructures in transparent fused silica glass. *Nat Commun* 2019; 10: 1439.

[58] He S, Chen F, Liu K, et al. Fabrication of three-dimensional helical microchannels with arbitrary length and uniform diameter inside fused silica. *Opt Lett* 2012; 37: 3825–3827.

[59] LoTurco S, Osellame R, Ramponi R, et al. Hybrid chemical etching of femtosecond laser irradiated structures for engineered microfluidic devices. *J Micromechanics Microengineering* 2013; 23: 085002.

[60] Isiksacan Z, Guler MT, Aydogdu B, et al. Rapid fabrication of microfluidic PDMS devices from reusable PDMS molds using laser ablation. *J Micromechanics Microengineering* 2016; 26: 035008.

[61] Cho BS, Schuster TG, Zhu X, et al. Passively Driven Integrated Microfluidic System for Separation of Motile Sperm. *Anal Chem* 2003; 75: 1671–1675.

[62] Schuster TG, Cho B, Keller LM, et al. Isolation of motile spermatozoa from semen samples using microfluidics. *Reprod Biomed Online* 2003; 7: 75–81.

[63] Hwang, B., Lee, D., Hwang, SJ. et al. Rheotaxis Based High-Throughput Motile Sperm Sorting Device. Int. J. Precis. Eng. Manuf. 20, 1037–1045 (2019).

[64] Bukatin A, Kukhtevich I, Stoop N, et al. Bimodal rheotactic behavior reflects flagellar beat asymmetry in human sperm cells. *Proc Natl Acad Sci* 2015; 112: 15904–15909.

[65] Nosrati R, Vollmer M, Eamer L, et al. Rapid selection of sperm with high DNA integrity. *Lab Chip* 2014; 14: 1142–1150.

[66] Unger MA, Chou H-P, Thorsen T, et al. Monolithic Microfabricated Valves and Pumps by Multilayer Soft Lithography. *Science* 2000; 288: 113–116.

[67] Elizabeth Hulme S, Shevkoplyas SS, Whitesides GM. Incorporation of prefabricated screw, pneumatic, and solenoid valves into microfluidic devices. *Lab Chip* 2009; 9: 79–86.

[68] Gallagher MT, Smith DJ, Kirkman-Brown JC. CASA: tracking the past and plotting the future. *Reprod Fertil Dev* 2018; 30: 867–874.

[69] Bonner WA, Hulett HR, Sweet RG, et al. Fluorescence Activated Cell Sorting. *Rev Sci Instrum* 2003; 43: 404–409.

[70] Wang Y, Wang X, Pan T, et al. Label-free single-cell isolation enabled by microfluidic impact printing and real-time cellular recognition. *Lab Chip* 2021; 21: 3695–3706.

[71] Lamanna J, Scott EY, Edwards HS, et al. Digital microfluidic isolation of single cells for -Omics. *Nat Commun* 2020; 11: 5632.

[72] Carlo DD, Wu LY, Lee LP. Dynamic single cell culture array. *Lab Chip* 2006; 6: 1445–1449.

[73] Arakawa T, Noguchi M, Sumitomo K, et al. High-throughput single-cell manipulation system for a large number of target cells. *Biomicrofluidics* 2011; 5: 014114.

[74] Chen Y, Wu T-H, Kung Y-C, et al. 3D pulsed laser-triggered high-speed microfluidic fluorescence-activated cell sorter. *Analyst* 2013; 138: 7308–7315.

[75] Nawaz AA, Chen Y, Nama N, et al. Acoustofluidic Fluorescence Activated Cell Sorter. *Anal Chem* 2015; 87: 12051–12058.

[76] Hejazian M, Li W, Nguyen N-T. Lab on a chip for continuous-flow magnetic cell separation. *Lab Chip* 2015; 15: 959–970.

[77] J. Kim, H. -H. Lee, U. Steinfeld, et al. Fast Capturing on Micromagnetic Cell Sorter. *IEEE Sens J* 2009; 9: 908–913.

[78] Lee J-J, Jeong KJ, Hashimoto M, et al. Synthetic Ligand-Coated Magnetic Nanoparticles for Microfluidic Bacterial Separation from Blood. *Nano Lett* 2014; 14: 1–5.

[79] Jan Krüger, Kirat Singh, Alan O'Neill, et al. Development of a microfluidic device for fluorescence activated cell sorting. *J Micromechanics Microengineering* 2002; 12: 486.

[80] A. Romani, N. Manaresi, L. Marzocchi, et al. Capacitive sensor array for localization of bioparticles in CMOS lab-on-a-chip. In: *2004 IEEE International Solid-State Circuits Conference (IEEE Cat. No.04CH37519)*. 2004, pp. 224-225 Vol.1.

[81] Zhang X, Khimji I, Gurkan UA, et al. Lensless imaging for simultaneous microfluidic sperm monitoring and sorting. *Lab Chip* 2011; 11: 2535–2540.

[82] Barnea I, Karako L, Mirsky SK, et al. Stain-free interferometric phase microscopy correlation with DNA fragmentation stain in human spermatozoa. *J Biophotonics* 2018; 11: e201800137.

[83] Eravuchira PJ, Mirsky SK, Barnea I, et al. Individual sperm selection by microfluidics integrated with interferometric phase microscopy. *Methods Quant Phase Imaging Life Sci* 2018; 136: 152–159.

[84] Daloglu MU, Ozcan A. Computational imaging of sperm locomotion. *Biol Reprod* 2017; 97: 182–188.

[85] Su T-W, Xue L, Ozcan A. High-throughput lensfree 3D tracking of human sperms reveals rare statistics of helical trajectories. *Proc Natl Acad Sci* 2012; 109: 16018–16022.

[86] Heng X, Erickson D, Baugh LR, et al. Optofluidic microscopy—a method for implementing a high resolution optical microscope on a chip. *Lab Chip* 2006; 6: 1274–1276.

[87] Sun T, Morgan H. Single-cell microfluidic impedance cytometry: a review. *Microfluid Nanofluidics* 2010; 8: 423–443.

[88] De Angelis A, Ferrara MA, Coppola G, et al. Combined Raman and polarization sensitive holographic imaging for a multimodal label-free assessment of human sperm function. *Sci Rep* 2019; 9: 4823.

[89] Xie C, Li Y. Confocal micro-Raman spectroscopy of single biological cells using optical trapping and shifted excitation difference techniques. *J Appl Phys* 2003; 93: 2982–2986.

[90] PIMENTEL JA, CARNEIRO J, DARSZON A, et al. A segmentation algorithm for automated tracking of fast swimming unlabelled cells in three dimensions. *J Microsc* 2012; 245: 72–81.

[91] Inaba K, Shiba K. Microscopic analysis of sperm movement: links to mechanisms and protein components. *Microscopy* 2018; 67: 144–155.

[92] Tasoglu S, Safaee H, Zhang X, et al. Exhaustion of Racing Sperm in Nature-Mimicking Microfluidic Channels During Sorting. *Small* 2013; 9: 3374–3384.

[93] Asghar W, Velasco V, Kingsley JL, et al. Selection of Functional Human Sperm with Higher DNA Integrity and Fewer Reactive Oxygen Species. *Adv Healthc Mater* 2014; 3: 1671–1679.

[94] Kirkman-Brown JC, Smith DJ. Sperm motility: is viscosity fundamental to progress? *Mol Hum Reprod* 2011; 17: 539–544.

[95] De Wagenaar B, Berendsen JTW, Bomer JG, et al. Microfluidic single sperm entrapment and analysis. *Lab Chip* 2015; 15: 1294–1301.

[96] Chai H, Feng Y, Liang F, et al. A microfluidic device enabling deterministic single cell trapping and release. *Lab Chip* 2021; 21: 2486–2494.

[97] Seemann R, Brinkmann M, Pfohl T, et al. Droplet based microfluidics. *Rep Prog Phys* 2011; 75: 016601.

[98] Wu H, Chen X, Gao X, et al. High-Throughput Generation of Durable Droplet Arrays for Single-Cell Encapsulation, Culture, and Monitoring. *Anal Chem* 2018; 90: 4303–4309.

[99] Collins DJ, Neild A, deMello A, et al. The Poisson distribution and beyond: methods for microfluidic droplet production and single cell encapsulation. *Lab Chip* 2015; 15: 3439–3459.

[100] Sinha N, Yang H, Janse D, et al. Microfluidic chip for precise trapping of single cells and temporal analysis of signaling dynamics. *Commun Eng* 2022; 1: 18.

[101] Kobel S, Valero A, Latt J, et al. Optimization of microfluidic single cell trapping for long-term on-chip culture. *Lab Chip* 2010; 10: 857–863.

[102] Faley SL, Copland M, Wlodkowic D, et al. Microfluidic single cell arrays to interrogate signalling dynamics of individual, patient-derived hematopoietic stem cells. *Lab Chip* 2009; 9: 2659–2664.

[103] Frimat J-P, Becker M, Chiang Y-Y, et al. A microfluidic array with cellular valving for single cell co-culture. *Lab Chip* 2011; 11: 231–237.

[104] Montenegro-Johnson T, Loghin D, Smith D. *Rheological and boundary effects on microswimmers*. 2013.

[105] Ishimoto K, Gadêlha H, Gaffney EA, et al. Human sperm swimming in a high viscosity mucus analogue. *J Theor Biol* 2018; 446: 1–10.

[106] Johnson, D., Loghin, D., Blake, R. and Smith, D. Fluid-Structure Interaction of Micro-Swimmers. In: *EUROMECH Colloquium 521*. 2011, pp. 43–44.

[107] Smith, D., Gaffney, A., Gadêlha H. and Kirkman-Brown, J. Bending Moment Efficiency of Sperm Motility. In: *EUROMECH Colloquium 521*. 2011, pp. 45–46.

[108] SMITH DJ, GAFFNEY EA, BLAKE JR, et al. Human sperm accumulation near surfaces: a simulation study. *J Fluid Mech* 2009; 621: 289–320.

[109] Gallagher MT, Smith DJ. Meshfree and efficient modeling of swimming cells. *Phys Rev Fluids* 2018; 3: 053101.

[110] Ishimoto K, Gadêlha H, Gaffney EA, et al. Coarse-Graining the Fluid Flow around a Human Sperm. *Phys Rev Lett* 2017; 118: 124501.

[111] Denissenko P, Kantsler V, Smith D, et al. Human sperm cells swimming in micro-channels.

[112] Iida T, Iwata Y, Mohri T, et al. A coordinated sequence of distinct flagellar waveforms enables a sharp flagellar turn mediated by squid sperm pH-taxis. *Sci Rep* 2017; 7: 12938.

[113] Gonzalez-Castro RA, Carnevale EM. Use of microfluidics to sort stallion sperm for intracytoplasmic sperm injection. *Anim Reprod Sci* 2019; 202: 1–9.

[114] Matsuura K, Uozumi T, Furuichi T, et al. A microfluidic device to reduce treatment time of intracytoplasmic sperm injection. *Fertil Steril* 2013; 99: 400–407.

[115] Zhang Y, Xiao R-R, Yin T, et al. Generation of Gradients on a Microfluidic Device: Toward a High-Throughput Investigation of Spermatozoa Chemotaxis. *PLOS ONE* 2015; 10: e0142555.

[116] Bahat A, Eisenbach M. Sperm thermotaxis. *Mol Cell Endocrinol* 2006; 252: 115–9.

[117] Li Z, Liu W, Qiu T, et al. The construction of an interfacial valve-based microfluidic chip for thermotaxis evaluation of human sperm. *Biomicrofluidics* 2014; 8 2: 024102.

[118] Penchev P, Dimov S, Bhaduri D, et al. Generic software tool for counteracting the dynamics effects of optical beam delivery systems. *Proc Inst Mech Eng Part B J Eng Manuf* 2017; 231: 48–64.

[119] Buls S, Craeghs T, Clijsters S, et al. The Influence of a Dynamically Optimized Galvano Based Laser Scanner on the Total Scan Time of SLM Parts. Epub ahead of print 16 August 2013. DOI: 10.26153/TSW/15430.

[120] Venzac B, Deng S, Mahmoud Z, et al. PDMS Curing Inhibition on 3D-Printed Molds: Why? Also, How to Avoid It? *Anal Chem* 2021; 93: 7180–7187.

[121] Johnston ID, McCluskey DK, Tan CKL, et al. Mechanical characterization of bulk Sylgard 184 for microfluidics and microengineering. *J Micromechanics Microengineering* 2014; 24: 035017.

[122] Newcastle Hospitals NHS Foundation Trust. What happens during IVF, https://www.newcastle-hospitals.nhs.uk/services/fertility-treatment/ivf-and-icsi-information-for-patients-having-treatment/what-happens-during-ivf/ (2023, accessed 25 April 2023).

[123] Beauchamp PJ, Galle PC, Blasco L. Human sperm velocity and postinsemination cervical mucus test in the evaluation of the infertile couple. Arch Androl. 1984;13(2- 3):107-12.

[124] Heydari, A., Zabetian Targhi, M., Halvaei, I. et al. A novel microfluidic device with parallel channels for sperm separation using spermatozoa intrinsic behaviors. Sci Rep 13, 1185 (2023).

[125] Vinny R. Sastri, Chapter 4 - Material Requirements for Plastics used in Medical Devices, Editor(s): Vinny R. Sastri, In Plastics Design Library, Plastics in Medical Devices, William Andrew Publishing, 2010, Pages 33-54, ISBN 9780815520276,

[126] Oh KW, Lee K, Ahn B, et al. Design of pressure-driven microfluidic networks using electric circuit analogy. *Lab Chip* 2012; 12: 515–545.

[127] Hu S, Wang R, Tsang CM, et al. Revealing elasticity of largely deformed cells flowing along confining microchannels. *RSC Adv* 2018; 8: 1030–1038.